

Complex Liquid Crystal Phases in Cylindrical Confinement



Ruibin Zhang

Supervised by Prof. Goran Ungar

Dr. Xiangbing Zeng

A thesis submitted for the degree of Doctor of Philosophy
in the Department of Material Science and Engineering

The University of Sheffield

September 2012

Acknowledgements

It would not have been possible to finish my PhD study and write this thesis without the help and support of the kind people, to only some of whom it is possible to give particular mention here.

Above all I would like to thank my principle supervisor, Prof. Goran Ungar for giving me this opportunity to do this challenging research work with financial support from his research group, and for his most valuable guidance, advice and encouragement in all stages of my PhD study. I'm very grateful to Dr. Xiangbing Zeng, my second supervisor, for his constant support and enlightening advice throughout my study. I also thank my colleague Dr Feng Liu for all the helpful discussion and suggestion.

The samples used in this study cost lots of effort of other people. I would therefore like to thank Prof. Carsten Tschierske and members of his group, of Martin-Luther-University for the synthesis of T-shaped molecules; Prof. Richard Bushby from the University of Leeds and Prof. Andrew Cammidge from the University of East Anglia for providing the discotic liquid crystals; Prof. Martin Steinhart from the University of Osnabrück, Prof. Kyusoon Shin and Mr. Bong Seock Kim from Seoul National University for providing the anodic aluminium oxide templates; Prof. Jang and Dr. Sa Hoon Min from Seoul National University for fabricating the mesoporous silica nanofibers.

I'm also grateful to the help and support here around the University of Sheffield. My special thanks go to Dr. Jamie Hobbs and Dr. Christa Weber from the Physics and Astronomy department for offering me the training and access to AFM, without which some problems in this study can never be solved. Many thanks go to Dr Patrick Baker from the department of Molecular Biology for giving me the access to the X-ray facility. I'm also very thankful to Dr. Wei Guan in our department for his help on TEM observation.

Finally I would like to express my love and gratitude to my family. I'd particularly like to thank my parents for their support, understanding, and encouragement in every possible way. I'm especially grateful to my aunt Mrs Henxiu Ma, who kindly supported my living expenses here, without which my PhD study in the UK would never be possible.

Abstract

Confined liquid crystals (LCs) have attracted much interest because their richness in physical phenomena and potential applications. In this thesis the configuration of novel liquid crystal phases confined in cylindrical cavities from tens of nanometres to hundred of microns primarily were investigated by means of small angle X-ray scattering (SAXS), grazing incident X-ray scattering (GSAXS) and atomic force microscopy (AFM).

The arrangement of honeycomb phases and 3-d channeled-layer phases (ChL) formed by polyphilic side-branched compounds in nanoporous anodic aluminium oxide (AAO) templates as well as in glass capillaries with micrometer diameters were investigated. 3-d diffraction patterns were reconstructed from the SAXS data. A fracture method associated with AFM observation was performed on the AAO samples to complement the X-ray study. Details of assembly of individual columns inside the nanochannel were directly observed by AFM for the first time. Surprisingly, even the planar-anchored columns were found reluctant to orient axially (parallel to the 1-d channel), which was explained by the strong deformation energy of the 2-d lattice. Besides, the in-plane orientation of the 2-d lattice was observed in both planar and homeotropic anchoring conditions and different mechanisms were proposed. For the ChL phase, axial orientation was observed due to the high rigidity of the columns. The 3-d layered structure could be suppressed by the nanopores and an induced smectic structure was observed.

Configuration of several discotic columnar LCs in cylindrical confinement was studied. The investigation of pure triphenylene derivatives in nanopores refutes the only detailed experimental work on discotics published as far. Again the discotic columns are mainly perpendicular to the channel axis, even with planar anchoring condition, to avoid the distortion of the 2-d lattice. The axial configuration was observed only when the rigidity of the columns was increased by dopant.

The structure of LC-directed mesoporous silica nanofibers fabricated via dual structure-directing agents in 200 nm AAO membranes was characterized by SAXS and TEM. Different mesoporous structures were observed when changing the alkyl chain length of the cationic surfactant.

Contents

CHAPTER 1 Introduction	1
1.1 The liquid crystalline state.....	2
1.2 Liquid crystal mesogens and their mesophases	3
1.2.1 Calamitics	3
1.2.2 Discotics.....	4
1.2.3 T-shaped liquid crystals	7
1.3 Defects in columnar liquid crystals	9
1.3.1 Dislocations.....	9
1.3.2 Disclinations.....	10
1.3.3 Developable domains.....	12
1.4 Liquid crystals confined in cylindrical geometry	13
1.4.1 Nematics and Smectics	13
1.4.2 Discotics.....	16
1.5 Alumina nano-template.....	19
1.6 Mesostructured silica nanofibers	20
CHAPTER 2 Experimental Methods	22
2.1 Preparation methods	22
2.1.1 AAO template samples preparation.....	22
2.1.2 Surface modification.....	24
2.2 X-ray diffraction	24
2.2.1 Synchrotron radiation	25
2.2.2 Small angle X-ray scattering.....	26
2.2.3 Grazing Incidence Small angle X-ray scattering	28
2.2.4 Reciprocal Spacing Reconstruction.....	29
2.3 Microscopy.....	30
2.3.1 Optical microscopy.....	30
2.3.2 Scanning electron microscopy.....	31
2.3.3 Transmission electron microscopy	31

2.3.4 Atomic Force Microscopy	31
CHAPTER 3 Planar-anchored Honeycomb Phases in Cylindrical Cavities	35
3.1 Introduction	35
3.2 Porous anodic alumina templates	36
3.2.1 Square honeycomb phases	36
3.2.2 Hexagonal honeycomb phases	54
3.3 Glass capillaries.....	57
3.3.1 Round capillaries	58
3.3.2 Square capillaries.....	63
3.4 Conclusions	65
CHAPTER 4 Homeotropic-anchored Honeycomb Phase in Cylindrical Confinement	67
4.1 Introduction	67
4.2 The compound	68
4.3 AAO templates	69
4.3.1 B1 in 400 nm AAO template.....	69
4.3.2 B1 in 60 and 20 nm AAO template	76
4.4 Glass capillaries.....	77
4.4.1 Round capillaries	78
4.4.2 Rectangular capillary	85
4.5 Conclusions	87
CHAPTER 5 3d Phases in Cylindrical Confinement	89
5.1 Introduction	89
5.2 Compounds.....	90
5.3 Results and discussions	91
5.3.1 C1	91
5.3.2 C2	96
5.4 Conclusion.....	102
CHAPTER 6 Columnar Discotic Liquid Crystals in Cylindrical Confinement.....	103
6.1 Introduction	103
6.2 Compounds.....	104
6.3 Triphenylene-based mesogens	104

6.3.1 Homeotropically anchored columns	105
6.3.2 Planar-anchored columns	116
6.3.3 Influence of the dopant	123
6.4 Helicene	129
6.5 Conclusions	132
CHAPTER 7 Mesoporous Nanofibers from Dual Structure-Directing Agents in AAO Template	134
7.1 Introduction	134
7.2 MSNF samples	135
7.3 Results and discussions	136
7.4 Conclusion	143
Summary	144
Future work	147
References	149
Appendix	154
A.1 Construction of the 3-d diffraction pattern	154
A.2 Calculation of the correlation length	155
A.2.1 Determination of direct beam width	155
A.2.2 Determination of intrinsic line widths and coherence length	156

CHAPTER 1 Introduction

Liquid crystals (LCs) combine both order and mobility on a molecular and supramolecular level: they are anisotropic in some of their properties while showing a certain degree of fluidity, which in some cases may be comparable to that of liquids. Due to this dual nature they are easily affected by external fields such as applied electric, magnetic fields and the substrate surface. Alignment of bulk LC mesophases by surface anchoring is a key technique used in the construction of LC devices. Later the surface anchoring was extended to three-dimensions by confining them to curved geometries such as spheres and cylinders. Confined LCs have attracted much interest because of their richness in physical phenomena and potential applications^[1]. Compared to the bulk, they experience strong non-planar restrictions and interfacial interactions imposed by the surrounding matrix due to the large surface to volume ratio, which can profoundly affect their ordering and orientations. The study of the nematics in spherical confinement finally lead to the discovery of polymer dispersed liquid crystal (PDLC)^[2] materials for electro-optic devices. In addition, cylindrical porous membranes with uniform and controllable pore diameters further facilitated the study of the confinement effect on the LCs. They provided cylindrical cavities with a large range of diameters in which the configuration of the LCs could be examined. Also the inner walls are accessible to chemical treatment for control of molecular anchoring.

In this work the configuration of novel columnar and some 3-d liquid crystal phases confined in cylindrical cavities is studied. The emphasis is on the effect of curvature, surface anchoring manner and the LC phase geometry on the orientation of the LC phases inside the cavity.

1.1 The liquid crystalline state

LCs are an intermediate phase of matter in addition to the solid and liquid phases. In a crystalline solid, there is both positional and orientational long-range order, i.e., the constituent elements (i.e. atoms, molecules) are fixed on a 3-d periodic lattice and do not possess mobility within the crystal although they can vibrate around their lattice points due to thermal energy. Contrary to it, both types of order are absent in isotropic liquids. In liquid crystal, the positional order is either fully or partially lost while there is some degree of orientational order^[3]. As a result, the liquid crystalline phase possesses some of the characteristics of the order, evidenced by X-ray diffraction, and some of the disorder, evidenced by the ease of flow. Compared to the crystal, the orientational order parameter $\langle(3\cos^2\phi-1)/2\rangle$ in a liquid crystal is significantly smaller than 1 and is highly dependent on temperature (here ϕ is the angle between the molecular axis and the director). This combination of order and mobility on a molecular or supramolecular level makes liquid crystals unique materials: they respond to external (electric, magnetic, chemical or mechanical) stimuli by rapidly adopting configurations of minimum free energy.

There are different ways to classify LCs^[3]. They can be divided into thermotropic and lyotropic. In thermotropic LCs, the self-organization occurs on heating of the pure compounds, and the shape of the molecules dictates the orientational order and the thermal motion gives the mobility. While in lyotropic LCs the mobility is provided by the addition of solvents, and their order is governed by the relative concentration of the solute. Considering the geometrical structure of the mesogenic molecules, they can be grouped into two main types: the "calamities" formed from the rod-shaped molecules and the "discotics" formed from disc-like molecules. The liquid crystalline phases are further categorized into nematic, smectic and columnar phases by their symmetry in terms of the orientational and translational degrees of freedom.

1.2 Liquid crystal mesogens and their mesophases

An essential requirement for thermotropic LC state to occur is that the molecule must be highly geometrically anisotropic in shape, like a rod or a disc. Considering the geometrical structure of the mesogenic molecules, LCs could be generally divided into calamitics and discotics depending on whether their mesophases are formed by rod-like or disc-like molecules.

1.2.1 Calamitics

Rod-like molecules possess a large extend of anisotropy, and they form the vast majority of thermotropic liquid crystals. Following the terminology introduced by Friedel^[4], they are classified broadly into three types: nematic, cholesteric and smectic.

The nematic phase of calamitics is the simplest liquid crystal phase. It differs from the isotropic liquid in that the molecules have some long-rang orientational order: they have a degree of preference to pointing along an averaged direction, which is defined as the director and denoted by the vector \mathbf{n} (Fig.1.1a). The cholesteric mesophase is also known as chiral nematic, in which the director rotates about an axis perpendicular to the long axes of the molecules to form a helical structure.

At certain conditions when the liquid crystal material gains an amount of positional order, it forms smectic phase where the molecules prefer to lie in layers, while within each layers it is still essentially a two-dimensional nematic liquid crystal. There are a number of types of smectic phases. When the director is perpendicular to the layer, the mesophase is called smectic A (SmA) (Fig.1.1b). If the director tilts away from the layer normal, it is called smectic C (SmC) (Fig.1.1c). There are also smectics which form layers with positional order within each layer. For example, in smectic B phase, the molecules in each layer are parallel to the layer normal, and they have the so-called hexatic ordering.

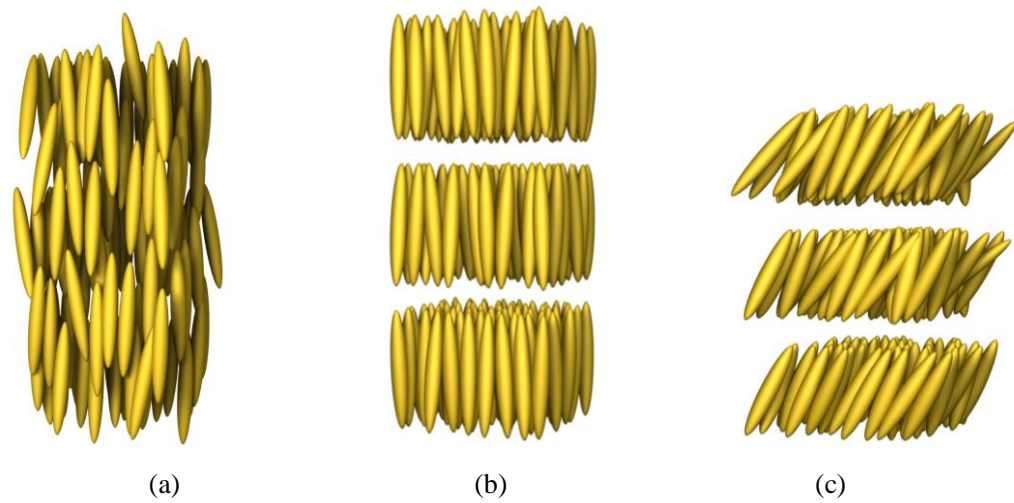


Figure 1.1 LC phases of calamitics: a). nematic phase, b) smectic A phase, c) smectic C phase.

1.2.2 Discotics

The first discotic liquid crystal molecule was a benzene ring as the core surrounded by six acyloxy chains^[5]. Since then a large number of discotic molecules has been synthesized^[6]. Generally speaking, discotics have flat and stiff aromatic cores with six or eight aliphatic long chain substituents connected to them by different linkages such as ether, ester, benzoate, alkyne, etc. The aromatic core unit is usually benzene or polyaromatic such as triphenylene^[7], perylene bisimide^[8], phthalocyanine^[9], and hexabenzocoroene^[10] (Fig.1.2); the substituents are flexible chains and can diminish the melting temperature of the LC phase. The self-assembly of DLCs is affected by the nature of the discoid core and the periphery flexible chains.

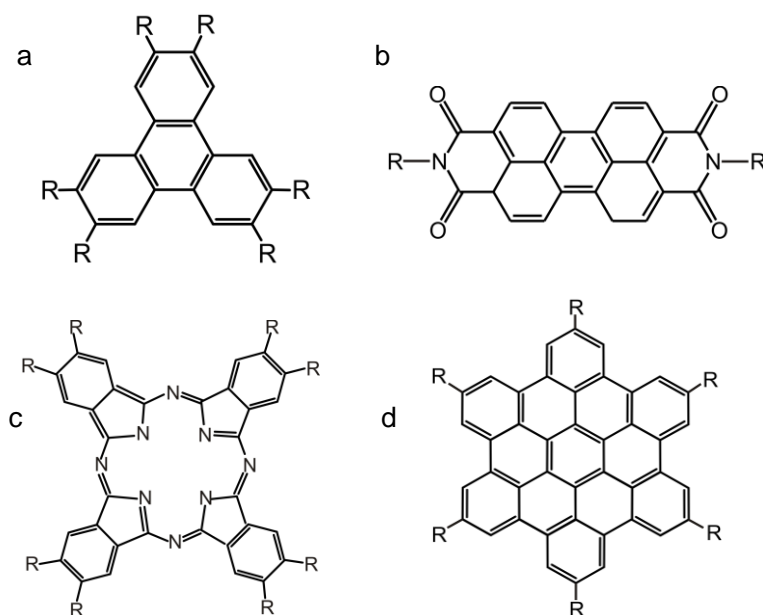


Figure 1.2 Mesogens of typical discotic molecules: a) triphenylenes; b) perylene bisimide; c) phthalocyanine; d) hexabenzocorone.

Disc-shaped molecules can form nematic phases by orienting the molecules more or less parallel (Fig.1.3a). However, unlike the usual rod-shaped nematic, discotic nematic phase is optically negative, with the director being the preferred axis of the orientation of the disc normals. In addition to the nematic phase, a majority of disc-shaped molecules form columnar phases by stacking one on top of the other. The driving force for formation of columnar mesophases has been postulated to be shape anisotropy^[11-13], microsegregation between flexible chains and rigid core^[14], and core-core van der Waals attractions^[15]. In discotic columnar phases, the flat molecular cores form an oriented, one-dimensional liquid i.e. they are orientationally ordered but translationally disordered. Although there is no positional order along the columns due to thermal fluctuations, the columns can pack parallel on a 2-d lattice. For instance, hexagonal columnar phase (Fig.1.3b) is characterized by a hexagonal packing of the molecular columns. The flexible hydrocarbon chains are highly disordered and form an amorphous shell surrounding the column of the core. The core-core distance inside a column is usually of the order of 3.5Å, and the intercolumnar distance is usually 20-40Å, depending on the length of the peripheral chains^[16].

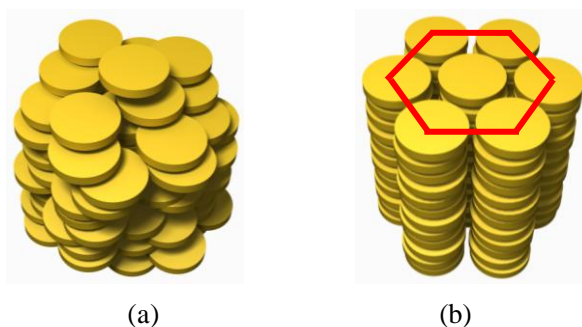


Figure 1.3 Schematic representations of LC phases of discotic molecules: a) nematics phase; b) hexagonal columnar phase.

The partial orbital overlap of neighboring aromatic cores leads to the formation of charge carrier pathways, while the flexible alkyl chains around the cores substantially insulate the column from the neighboring column. Thus the discotic columns behave nearly as one-dimensional conductors and may be described as “molecular wires”^[17]. Indeed, high charge carrier mobilities have been determined for many discotics^[18]. The columnar phase of hexa-peri-hexabenzocoronene (HBC) possesses the highest intrinsic charge-carrier mobility for this kind of material as reported so far^[19]. For small cores like triphenylene, the charge carrier mobility can be improved by introduction of electron acceptors^[20,21]. This property has attractive applications in electronic devices such as light-emitting diodes^[22], field-effect transistors^[23] and solar cells^[24, 25]. To realize these applications, the orientation of the columns must be well controlled in order to ensure the undisturbed migration of charges along the desired direction. For example, the main charge transport in field-effect transistors takes place parallel to the insulating substrate and therefore requires planar alignment of the discotic molecules with uniaxial columnar orientation in the charge-transport direction. In contrast, homeotropic alignment is required in light-emitting diodes and photovoltaic devices since the migration of charges is perpendicular to the substrate.

1.2.3 T-shaped liquid crystals

Thermotropic liquid crystalline phases are usually formed by either molecules with an anisometric shape or by amphiphilic molecules. In the case of anisometric molecules, the mesophases formed strongly depend on the molecular shape: calamitic or discotic molecules are arranged with their long axes parallel to each other to give thermotropic smectic or columnar liquid-crystalline phases. On the other hand, the self organization of amphiphilic molecules is mainly driven by the tendency to segregate incompatible (hydrophilic and hydrophobic) parts of the individual molecules, which gives rise to large aggregates of lamellar, columnar, or cubic thermotropic and lyotropic mesophases^[26]. By combining these two structural principles, that is, adding both alky chains and hydrophilic groups to the rigid aromatic core, novel T-shape amphiphiles have been synthesized^[27], as shown in Fig.1.4.

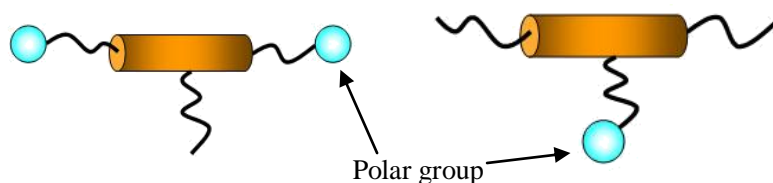


Figure 1.4 Schematic molecular structure of two ternary block molecules: (a) bolaamphiphiles with terminal polar groups; (b) facial amphiphiles with lateral polar groups.

T-shaped molecules can be generally divided into two classes: bolaamphiphiles and facialamphiphiles. Both compounds represent ternary amphiphiles with a T-like shape in which a rigid core of defined length is combined with two terminal chains and one lateral chain, incompatible with each other. In bolaamphiphiles, hydrophilic substituents are grafted to the terminal ends of rod-like mesogenic molecules^[27] and provide attractive forces (H-bonding) to stabilize the competition between the parallel alignment of the rodlike biphenyl units and the steric interaction. Different types of lamellar structures are formed when the length of the lateral chains is either very short or very long. While between these two extremes, a series of more complex and interesting phases, the

columnar phases are formed^[28], as shown in Fig.1.5. For the columnar mesophases, the rigid-rod segments tend to restrict the side length of the polygons within relatively narrow limits, giving rise to columns with a well-defined polygonal shape. The lateral chains fill the interior of the polygons; the terminal chains form the corners of these polygons and connect the rigid rods. Thus, the number of sides of the polygons critically depends on the volume of the lateral chain and the length of the molecule. The polygon that provides the exact volume required by the lateral chains is selected.

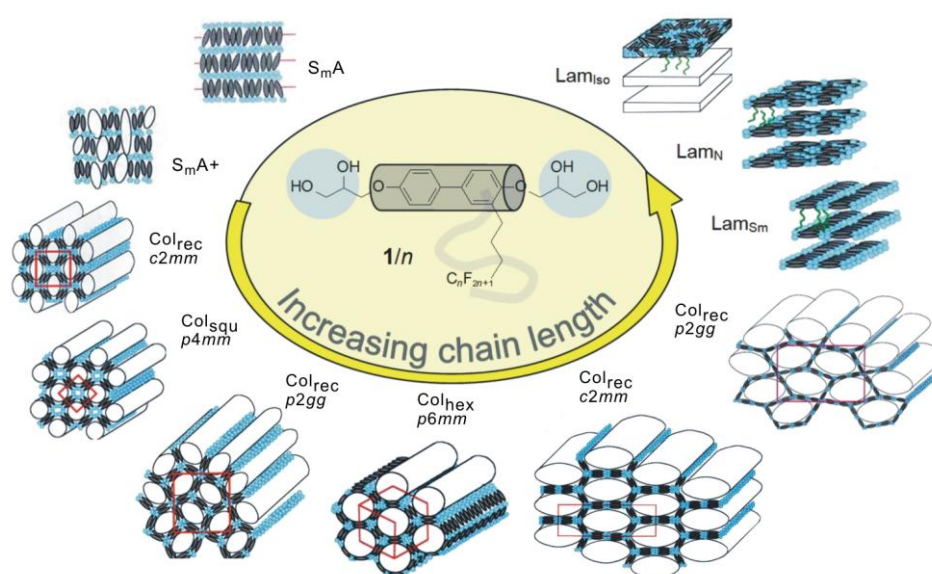


Figure 1.5 Schematic drawing of the phase sequence of bolaamphiphiles with the increasing of the length of the lateral chain. Reproduced from ref [28].

On the other hand, in faciamphiphiles the non-polar and polar chains are reversed, i.e., functional groups such as oligoethyleneoxide, carbohydrate units, or carboxylic acid groups are laterally attached to the rigid rod, while two non-polar chains are attached in the terminal positions^[29,30]. The sequence of mesophases starts with a conventional SmA phase (Fig.1.6). When increasing the volume fraction of the lateral chain cylinder structures are formed at first, which then change into new lamellar phases. It bears a relation to that found for the bolaamphiphiles as shown in Fig.1.5, which indicates the generality of the self-organization principles involved.

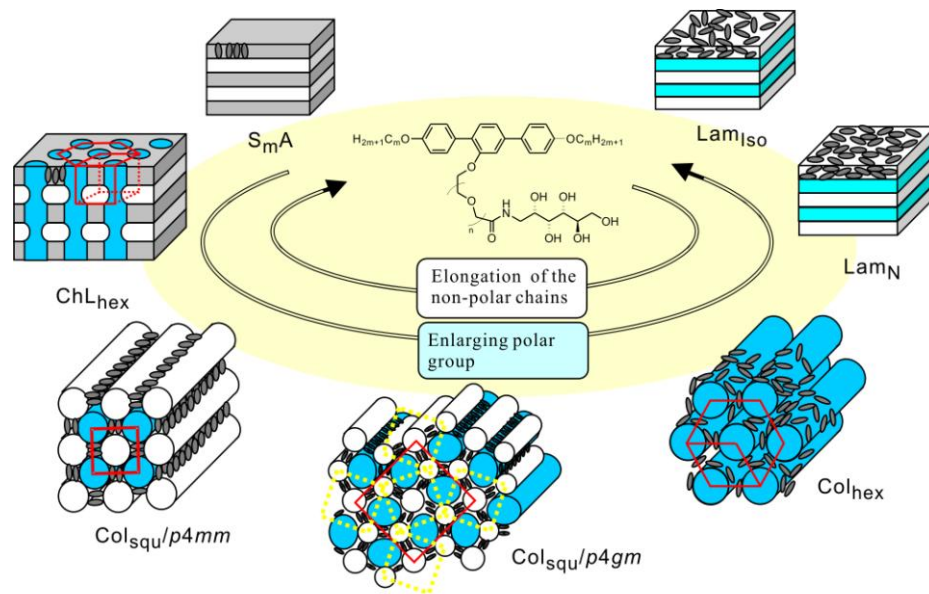


Figure 1.6 Schematic drawing of the phase sequence of facial amphiphiles. Reproduced from ref [30]

1.3 Defects in columnar liquid crystals

An understanding of the defects is vital in that it provides insight into the mesophase structure. In many cases the defects can stabilize the unusual mesophase structures, for example, the formation of blue phases and Twist Grain Boundary phases^[31]. Defects in the columnar phase have been investigated in detail by Bouligand^[32] and by Kleman and Oswald^[33]. Generally, they can be classified into three groups^[31]: dislocation, disclination, and developable domains.

1.3.1 Dislocations

By definition, these defects break the translational symmetry of the 2-d lattice of the columnar phases. There are two kinds of dislocations: edge dislocation and screw dislocation. The edge dislocation is a defect where an extra half-plane of lattice is introduced mid way through the crystal, distorting nearby planes of lattices. For edge dislocations, $\mathbf{b} \perp \mathbf{L}$, where \mathbf{b} is the Burgers vector and \mathbf{L} is the dislocation line. Edge

dislocations are further divided into longitudinal edge dislocations (\mathbf{L} parallel to the column axis \mathbf{n} , Fig.1.7a and b) and transverse edge dislocations (\mathbf{L} perpendicular to \mathbf{n} , Fig.1.7c and d). For screw dislocations the defect line movement is perpendicular to direction of the stress and the lattice displacement, rather than parallel, and \mathbf{b} is parallel to \mathbf{L} (Fig.1.7 e and f). A hybrid composed of screw and edge dislocations is shown in Fig.1.7g.

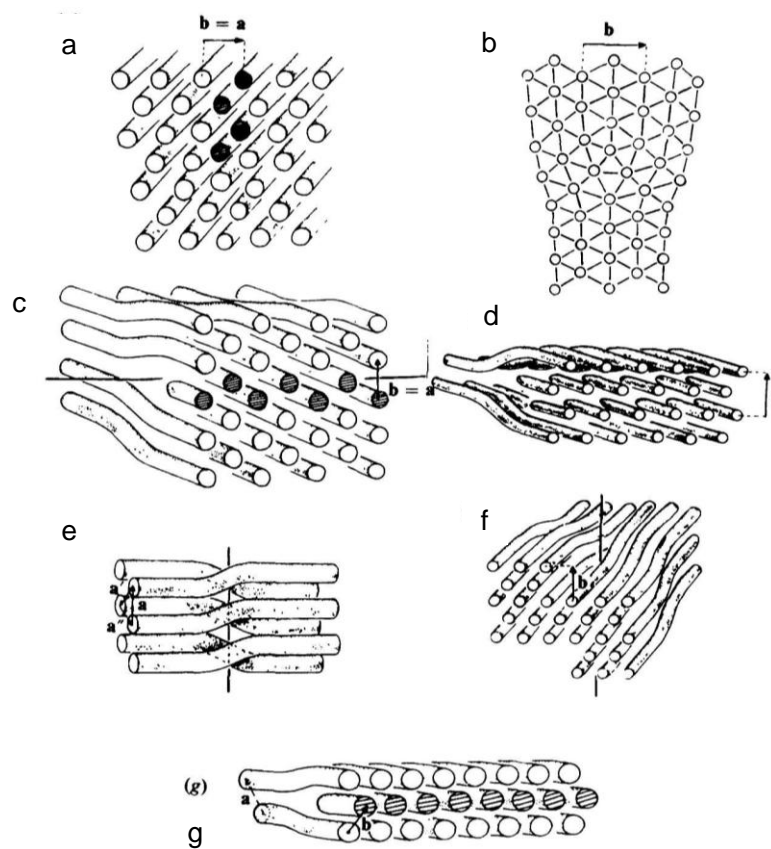


Figure 1.7 Dislocations in the columnar phase: a) and b) longitudinal edge dislocations; c) and d) transverse edge dislocations; e) and f) screw dislocations; g) a hybrid of screw and edge dislocations. (from ref [32]).

1.3.2 Disclinations

The term disclination is modified from ‘disinclination’, which was originally proposed by Frank^[34] to describe the points observed in the schlieren texture of nematics when they

were observed between crossed polarizers. Disclinations break the symmetry of rotations. In the hexagonal lattice, longitudinal wedge disclinations are the standard crystal disclinations, in which the rotation vector is the sixfold axis L_6 , or threefold axis L_3 , or twofold axis L_2 , parallel to the columns. The lattice gets stretched near a negative disclination (Fig.1.8a) and compressed near a positive one (Fig.1.8b). In transverse wedge disclinations the rotation vector is normal to \mathbf{n} . Examples of $\pm\pi$ disclinations are shown in Fig.1.8(c-e). Two transverse wedge disclinations can occur in association as shown in Fig.1.8 (f).

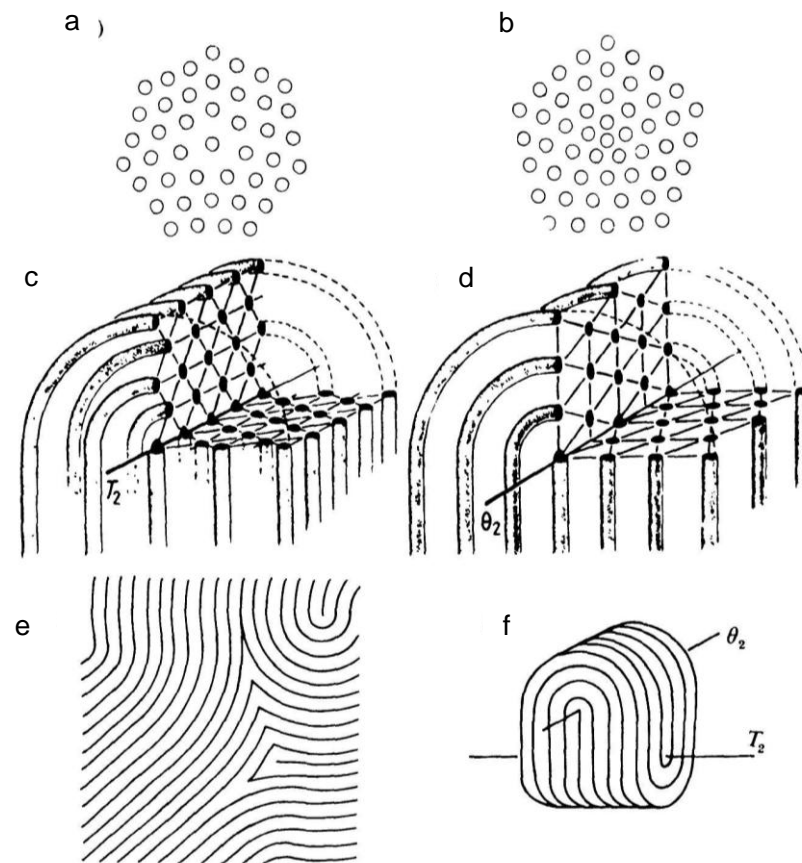


Figure 1.8 Disclinations in the columnar phase: a) and b) - $\pi / 3$ and $\pi / 3$ longitudinal wedge disclinations about the sixfold axis L_6 ; c) and d) π transverse wedge disclinations about the binary axes T_2 and θ_2 respectively; e) - π transverse wedge disclination leading to the formation of walls; f) two π disclinations at right angles to each other, one about T_2 and the other about θ_2 (from ref[32]).

1.3.3 Developable domains

In developable domains, there exist physical planes P (Fig.1.9a) perpendicular to the columns, and the envelope of these planes defines the developable surface D (Fig.1.9b). Developable domains can occur without distorting the hexagonal lattice and involving only the bending of the columns. There are three specific examples: (a) the developable surface degenerates into a straight line, and the columns form a set of coaxial circles around this line (Fig.1.9a); (b) the developable surface is a cylinder, and the columns are along the involutes of a circle in any plane normal to the axis of the cylinder; (c) the developable surface is generated by half-tangents to a helix, and the columns are normal to the half-tangents and are involutes of the helix (Fig.1.9c).

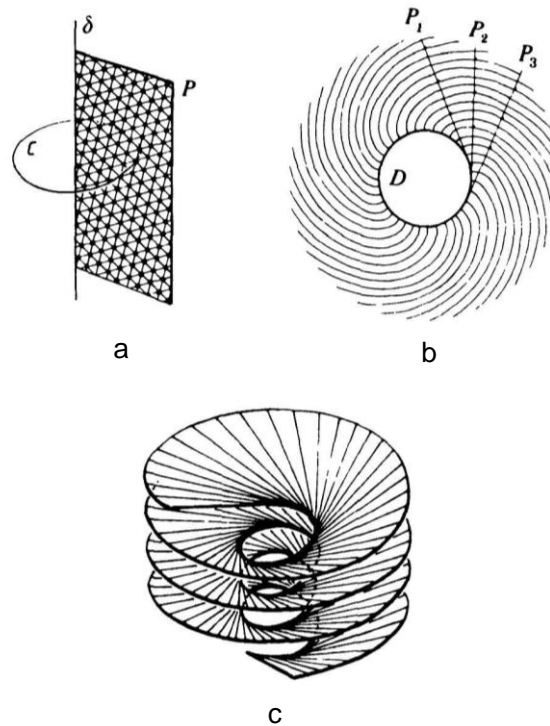


Figure 1.9 Developable domains in the columnar phase. a) the developable surface is degenerated into a straight line δ common to the planes P . The columnar axes form coaxial circles about δ . b) the developable surface D is a cylinder. The columns are a set of parallel and equispaced involutes of a circle. c) a Riemann surface generated by half-tangents to a helix. The columns are normal to the half-tangents (from ref [32]).

1.4 Liquid crystals confined in cylindrical geometry

1.4.1 Nematics and Smectics

The interest in liquid crystals confined to spherical and cylindrical geometries have lasted for more than a century. The initial work began in the early 1900's by Lehmann^[35]. He observed stable nematic director configurations in liquid crystal droplets suspended in an isotropic fluid. By studying the birefringent textures with optical polarizing microscopy he concluded that the specific director configuration within the spherical confining cavity depends on the liquid crystal material and the angle at which the liquid crystal molecules are anchored to the isotropic fluid interface.

It was first thought in the early 1970's that the nematic director field in a cylinder with perpendicular boundary conditions would consist of only a radial component with a line disclination along the cylinder axes where the director field is undefined^[36]. Later Cladis and Kleman^[37] and Meyer^[38] predicted that when nematics confined in cylindrical cavities under strong homeotropic anchoring condition, they would form an escaped-radial (ER) configuration (Fig.1.10) since the high cost of splay deformation energy in the center of the cylinder could be relieved by introducing a finite amount of bend deformation; a configuration transition from escaped radial to planar radial with an isotropic core along the cylinder axis will occur when the diameter becomes smaller than 0.1 μm . However, under strong planar anchoring conditions, an escaped-twisted (ET) structure would be stable. They also calculated the ET structure to transform into a planar-concentric (PC) structure when the elastic free energy becomes favorable^[37]. The ER structure has been optically verified in large capillary tubes of radius 20-200 μm ^[38-40], and it occurs with singular point defects regularly spaced along the cylinder axis (ERPD). The defects result from the fact that two energy-equivalent configurations exist where the direction of bend is changed.

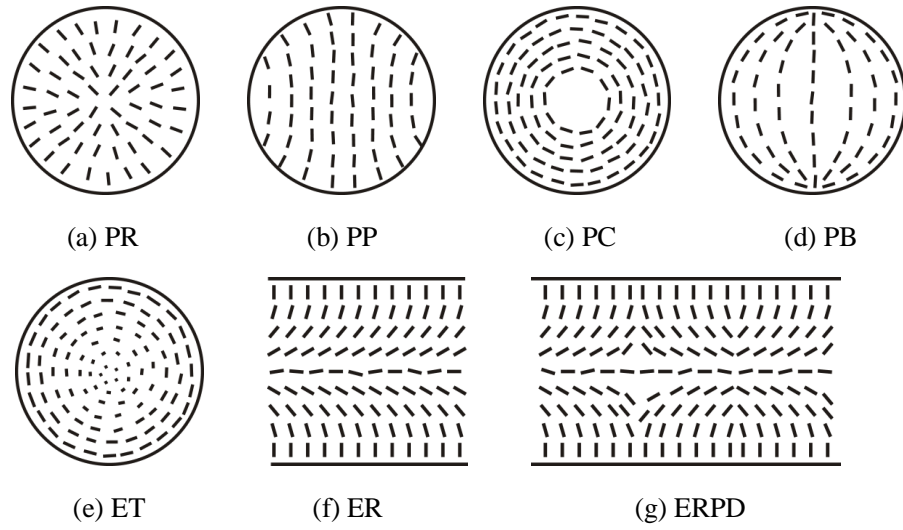


Figure 1.10 Schematic sketch of the a. planar radial (PR), b. planar polar (PP), c. planar-concentric (PC), d. planar bipolar (PB), e. escaped twisted (ET), f. escaped radial (ER), g. escaped radial with point defects (ERPD) nematic structure in the director field representation.

Based on $^2\text{H-NMR}$ study and Frank free energy analysis, Crawford and co-workers performed a series of studies on nematic LCs ($5\text{CB-}\beta d_2$) confined to nuclepore membranes. They measured the surface elastic constant K_{24} and molecular-anchoring strength W_0 ^[41,42], which were not accessible before in the submicrometer cavities. They found that under homeotropic anchoring condition, cylinders with untreated surfaces can provide sufficient anchoring strength to support the ERPD configuration for radius as small as $0.05 \mu\text{m}$, while cylinders with treated lecithin walls provide weakened anchoring strengths and only support this structure in cavities of radius $0.5 \mu\text{m}$ and above, and at $R \leq 0.4 \mu\text{m}$ the planar polar nematic configuration (PP) occurs rather than the PR structure^[42-44]. The total free energy of a confined liquid crystal is expressed as:

$$F = \frac{1}{2} \int_{vol} \{K_{11}(\nabla \cdot \mathbf{n})^2 + K_{22}(\mathbf{n} \cdot \nabla \times \mathbf{n})^2 + K_{33}(\mathbf{n} \cdot \nabla \times \mathbf{n})^2 - K_{24} \cdot (\mathbf{n} \times \nabla \times \mathbf{n} + \mathbf{n} \nabla \cdot \mathbf{n})\} dV + \frac{1}{2} \int_{surf} (W_\phi \sin \Phi' + W_\theta \cos \Phi') \sin^2 \theta' dS \quad (1.1)$$

where \mathbf{n} is the nematic director, the first three terms describe the splay, twist, and bend deformations, respectively, with K_{11} , K_{22} , and K_{33} denoting the appropriate elastic

constants. The fourth term is a surface elastic contribution where K_{24} is the saddle-splay surface elastic constant, a material constant independent of short-range interactions at the surface. The final two terms represent the interfacial free energy, described by the azimuthal W_ϕ and polar W_θ anchoring strengths. The deformation free energy of PR and PP configurations have been discussed^[44]. For PR configuration, n is normal to the surface, the energy per unit length of the cylinder, which is pure splay energy, is given by:

$$F_{PR} = \pi K_{11} \ln(R/\rho) \quad (1.2)$$

where R is the radius of the cylinder and ρ is the radius of the line disclination which is of the order of molecular dimensions, at which elastic theory breaks down. This configuration is independent of anchoring strength. For PP configuration, assuming $K_{11}=K_{22}=K_{33}$, under strong anchoring:

$$F_{PP} = \pi K \ln(R/2\rho) \quad (1.3)$$

By modifying the inner walls of the cylinders with a polyimide treatment, Crawford and co-workers managed to change the homeotropic anchoring condition to planar. They found that for cylinder sizes $R=0.2$ and $0.3 \mu\text{m}$, the nematics adopt the PB configuration, while increasing the pore size from $R=0.3 \mu\text{m}$ to $R=0.5 \mu\text{m}$ the director configuration transforms to the ET structure^[45]. Again, they considered the free energy and concluded that for PC configuration,

$$F_{PC} = \pi K_{33} \ln(R/\rho) \quad (1.4)$$

ρ is the radius of the core of the disclination. For PB configuration, the core was considered as isotropic liquid and the energy was not discussed. In the one-constant approximation ($K_{11}=K_{22}=K_{33}$),

$$F_{PB} = \pi K \ln(R/4\rho) \quad (1.5)$$

Later they studied chiral doped nematic LCs ($5CB-\beta d_2$) in Anopore membranes (alumina) with pores of $0.1 \mu\text{m}$ radius^[46] and found the parallel-axial structure for the pure nematic (Fig.1.11a), the radially twisted structure (Fig.1.11b) for low chirality and the twisted bipolar structure (Fig.1.11c) for higher chirality.

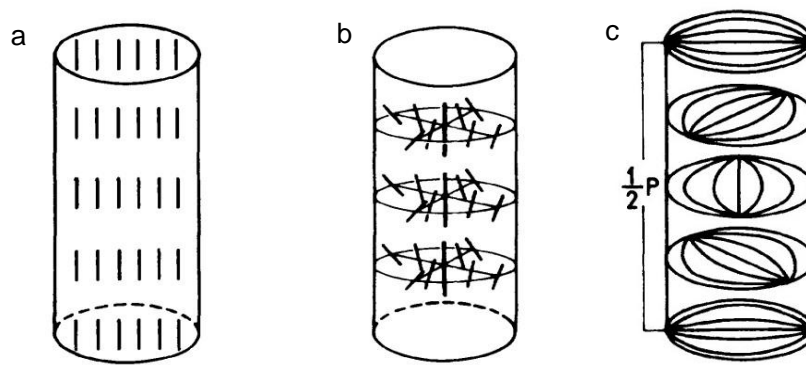


Figure 1.11 Nematic director field of (a) the PA configuration, (b) the RTA configuration, (c) the ATPB configuration. From ref [46].

After nematics, the next simplest LC phase studied in confinement is the smectic-A phase. Kralj and Zumer^[47] have discussed the relative stability of smectic-A structures in cylindrical cavities, and shown that ER configurations could be stabilized in the case of strong homeotropic anchoring. DNMR studies of the orientational order of elongated LC molecules (5CB and 8CB)^[48,49] in Anopore membranes by Crawford and coworkers have significantly contributed to the determination of director fields, surface parameters, and surface wetting phenomena. For both samples, they observed parallel axial configuration in the 200 nm pores of Anopore membranes. Jin^[50] et al. proposed that 10CB and 12CB confined in Anopore could experience different anchoring transitions depending on thermal treatment and atmospheric conditions, which would lead to the transition from parallel axial to planar radial configuration.

1.4.2 Discotics

Compared to the nematic and smectic phases of calamitics, there are few studies concerning the appearance of discotic molecules in cylindrical confinement. K.Q. Jian and G. Crawford firstly applied the previous results on nematics in cylindrical geometries to a disc-like polycyclic aromatic hydrocarbon in its nematics phase^[51]. The large discotic molecule was found to be planar-anchored on the flat alumina surface. They filled the discotics in the AAO template with a diameter of 200 nm, followed by heating and

template removal to produce carbon fibers with graphene layers. Using transmission electron microscopy they observed that the graphene layers lie perpendicular to the fiber axis, which they concluded is the result of static equilibrium in the confined discotic LC precursor: the director of the discotic nematics is parallel to the long-axis of the nanochannel.

M. Steinhart and coworkers^[52] studied the orientation of a triphenylene derivative in 60 and 400 nm AAO templates in which the molecules are homeotropically anchored. They used Theta/2Theta XRD scanning as the experimental method. The setup is schematically shown in Fig.1.12. By comparing the intensity of the reflections corresponding to the column planes and intracolumnar disk-to-disk distance, they concluded that the discotic molecules are highly oriented with their directors along the long axes of the nanopores, while close to the pore wall there's a thin homeotropically oriented layer due to the homeotropic anchoring of the molecules on the wall surface.

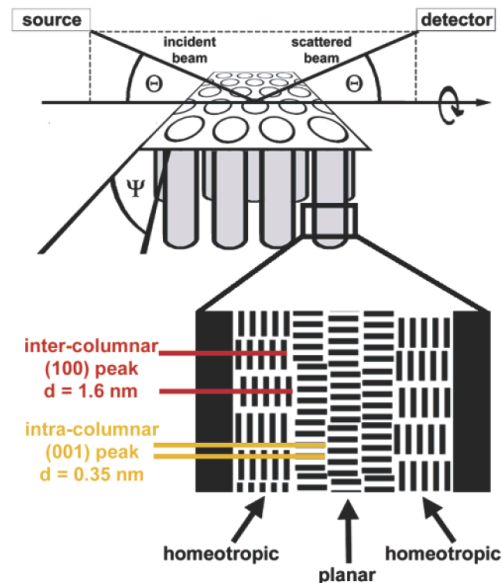


Figure 1.12 Schematic representation of the XRD setup in ref [52]. For the $\theta/2\theta$ scans the samples were placed in the device so that the surface of the template was oriented perpendicularly to the plane of incident and scattered X-ray beams.

Later they reported the influence of the polarity of the pore walls and dopants on the orientation of the discotic columns^[53,54]. In the case of coated nonpolar wall, they observed no apparent orientation of the columns. While proper selection of the dopant allows enhancing the axial orientation of the discotics in sub-50 nm pores. However these samples were all quenched from isotropic temperature and they haven't examined the configuration of the columns close to equilibrium. Furthermore, using the $\theta/2\theta$ scanning gives information on only very small region of reciprocal space, hence the reliability of these XRD results is limited.

D. Caprion reported Monte Carlo simulations of a model discotic molecule embedded in cylindrical pores with planar anchoring condition^[55]. They showed that for a small radius ($R= 5$ discs), the molecules were roughly oriented along the tube axis: the columns were either parallel to the tube axis or meandered around that axis (Fig.1.13a,b). However, in large pores ($R= 10$ discs), the columns can be built along the axis of the cylinder, but the constraint on the column's orientation is weak enough to allow ordering in all directions even perpendicularly to the tube (Fig.1.13c,d).

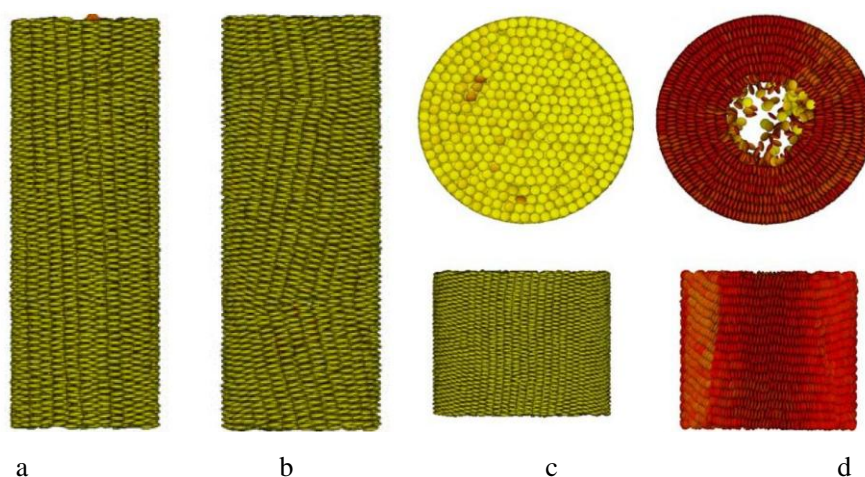


Figure 1.13 a) and b): $R= 5$ disc, with straight a) or zigzag ordering b); c) and d): $R=10$ disc. c) presents columns oriented along the z-axis at all distances from the wall, and d) presents columns wrapped around the tube forming a hole in the middle. From Ref [55].

1.5 Alumina nano-template

Ordered nanochannel array materials have raised considerable interest in recent years due to their utilization as a template for the fabrication of nano-sized fine structures. Anodized aluminum oxide (AAO) template is a popular choice because of its regular hexagonal pore packing, narrow size distributions of pore diameters and uniform pore depths^[56-59]. During anodization, nanopores grow perpendicular to the surface of the membrane with equilibrium of field-enhanced oxide dissolution at the oxide/electrolyte interface^[60,61]. As schematically shown in Fig.1.14, oxygen-containing ions (O^{2-} /OH⁻) migrate from the electrolyte through the oxide layer at the pore bottom to the metal/oxide interface and form oxide. While Al^{3+} ions simultaneously drift through the oxide layer into the solution at the oxide/electrolyte interface^[62]. It was suggested that the repulsive forces between neighboring pores caused by mechanical stress at the metal/oxide interface promote the formation of hexagonally ordered pore arrangements^[63]. The diameter of the pore can be controlled by varying anodization conditions such as applied voltage and utilized electrolytes, and the length of the nanoporous channels can simply be controlled by anodization time. Since its oxide pore walls have high surface energy, liquid soft matter with low surface energy spontaneously infiltrates the nanopores, enabling the creation of 1D nanostructures and advanced membrane configurations, which is of both scientific interest and potential applications.

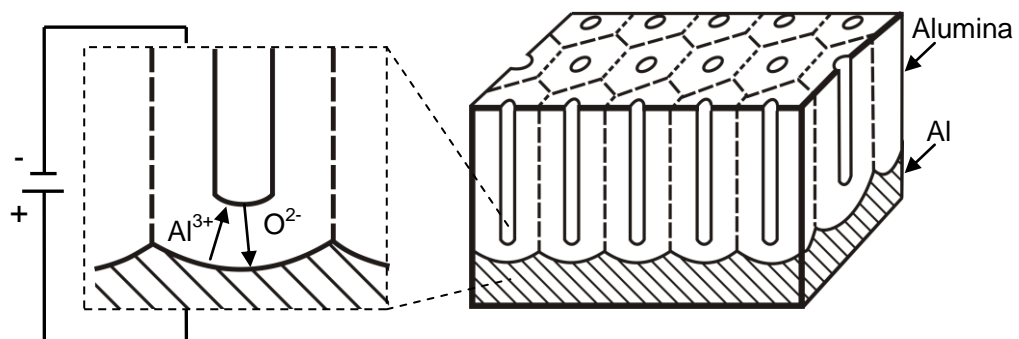


Figure 1.14. Scheme of the anodic oxidation of aluminium.

1.6 Mesostructured silica nanofibers

Porous solids are widely used in many diverse fields of science and engineering as adsorbents, catalysts and catalyst supports owing to their high surface areas. According to the IUPAC^[64] definition porous materials are divided into three classes: microporous (<2nm), mesoporous (2-50nm) and macroporous (>50nm). Well-known members of the microporous class are the zeolites, which provide excellent catalytic properties; larger pores are present in porous glasses and porous gels, known as mesoporous materials.

Kresge et al^[65] discovered that the cooperative self-assembly of surfactants, such as cetyltrimethylammonium bromide (CTAB), in a solution containing network-forming species, such as tetraalkoxysilanes, can be used for templating mesoporous silica structures, and they synthesized the first mesoporous solid (MCM 41) that showed a regularly ordered pore arrangement and a very narrow pore-size distribution. Since then, these materials have attracted considerable interest due to their diverse potential applications^[66]. For many applications it is required to form the mesoporous material as a thin film on a support surface^[67]. However, thin-film formation on solids, such as mica or silicon wafers, revealed that the channels of the formed mesoporous films are predominately aligned parallel to the substrate surface, which is not practicable for applications in specific fields, such as membrane science, because a pore direction perpendicular to the surface is necessary for these devices. Recently, surfactant-anodic aluminum oxide (AAO) dual templates were applied to the synthesis of mesostructured silica nanofibers (MSNF). When the silica–surfactant nanocomposite is grown inside the nanopores, the wall surface is expected to assist the self-organization of the silica–surfactant nanocomposite, and the resulting mesophase might be an assembly of oriented surfactant-templated silica-nanochannels. Several surfactants have been used as structure-directing agents to fabricate MSNFs in the AAO template. Yang and coworkers^[68] first reported the preparation of mesoporous silica fibers with concentric circular orientation inside the channels of AAO template using tetraethoxysilane (TEOS) mixed with a block

copolymer surfactant Pluronic F127 under acidic conditions. Yamaguchi et al.^[69] used hexadecyltrimethyl-ammonium bromide (CTAB) and obtained unidimensional channels of silica parallel to the long-axis of the AAO pores. Mallouk and co-workers^[70] described the formation of SBA-15-like MSNF using Pluronic P123. Maeda and co-workers^[71] reported the preparation of MSU-H mesoporous silica in AAO template. It was also revealed that the architecture/orientation of nanochannels formed within different pore sizes of AAO substrates using P123 was largely varied depending on the channel size of the substrates^[72, 73]. It was also reported that the orientation of the silica nanochannel can be controlled by changing the concentration of surfactants and the humidity in the gas phase during preparation^[74]. Thus, preparation of mesoporous silicas within the confined space of AAO substrates should have large potentials in tailoring mesopore architecture toward new applications.

CHAPTER 2 Experimental Methods

2.1 Preparation methods

2.1.1 AAO template samples preparation

The permeable AAO membranes were kindly provided by the groups of Prof. Martin Steinhart of Max Planck Institute in Halle and Prof. Kyusoon Shin of Seoul National University. These hexagonally packed nanoporous alumina templates were fabricated via a two-step anodization of high-purity aluminium sheets^[75-78]. First aluminum sheets were electropolished in a 4:1 v/v mixture of ethanol and perchloric acid at 4 °C. To obtain templates with pore diameter of 200 and 400 nm, the electropolished sheets were anodized at 190 V in 0.1 M phosphoric acid solution while the temperature was controlled to 0 °C. The first anodized alumina layer was removed by dipping the sheet into chromic acid at 75 °C and aluminum sheet remained after dipping was washed with distilled water and ethanol. The second anodization was carried out under the same conditions as the first anodization. Alumina layer on opposite side and non-oxidized aluminum layer were eliminated using NaOH solution and CuCl₂ solution, respectively. The barrier layer of alumina template was removed by floating the alumina on 0.1 M phosphoric acid solution at 60 °C. Pore diameter was adjusted by dipping the alumina templates into 0.1 M phosphoric acid at 30 °C. They normally contain 100 µm deep pores that grown perpendicular to the membrane. The aluminium substrates, which the AAO layers had initially been attached to, were selectively etched away with a mixture of 1.7 g CuCl₂ · H₂O, 50 mL concentrated HCl and 50 mL deionized water. Thus they became permeable free-standing membranes. Different sizes of the nanopores were obtained by changing the electrolyte, anodization voltage and temperature. For example, to obtain 60 nm membranes, 0.3 M oxalic acid was used as the electrolyte. The voltage and temperature were set at 40 V and 15 °C respectively; to obtain 20 nm membranes, 0.3 M sulfuric acid was used as the

electrolyte. The voltage and temperature were set at 25 V and 40°C respectively. Fig.2.1 shows the SEM images of the top surface of the empty templates of different sizes.

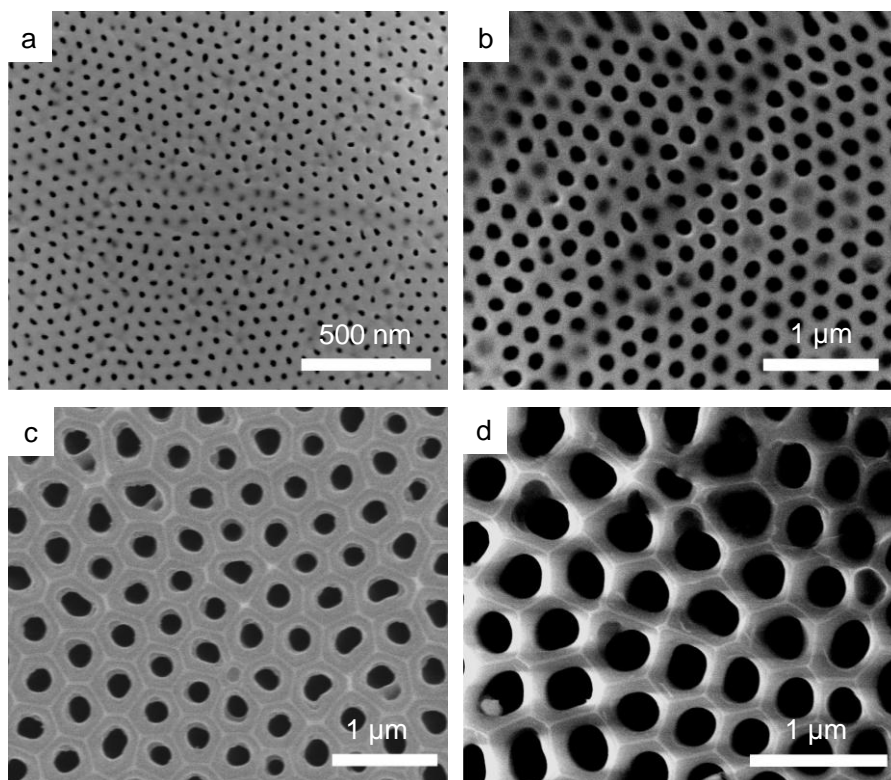


Figure 2.1 SEM images of empty templates with different pore diameters: a) 20 nm; b) 60 nm; c) 200 nm; d) 400 nm.

Filling of the templates with LC was prepared by melting the LCs on the top surface of the AAO membranes above their isotropic temperatures, during which they automatically infiltrated into the nanochannels due to the high surface energy. Materials remaining on the top surface were carefully wiped off with lens tissue while they were still liquid. Prior to any further experiments, the filled templates were heated to above the isotropization temperature of the LC and cooled slowly (0.1 K min^{-1}) in order to erase any flow-induced alignment and establish an equilibrium organization.

2.1.2 Surface modification

In order to study the effect of surface polarity on the orientation of the LC columns, the substrate surface was modified by hexadecyltrichlorosilane (HTS) (Fluorochem). For glass slides and capillaries, they were first cleaned with a 1:3 mixture of H₂O₂ (hydrogen peroxide) (30%) and H₂SO₄ (98%, Sigma-Aldrich) (“piranha” solution) at 70 °C for 15min to achieve a highly hydroxyl terminated silicon surface^[79], after which they were rinsed abundantly with pure deionised water. Then they were dried by hot air blower and dipped into a 1% solution of HTS in hexadecane (99% Sigma-Aldrich) at 80 °C for 2h. After removal from solution they were rinsed in chloroform and allowed to dry. For AAO templates, the inner wall surface was treated by HTS vapor at 90 ° for 3 hours.

2.2 X-ray diffraction

X-ray diffraction is one of the most important methods of studying ordered structures. The scattering of X-rays by a crystal can be considered as reflection by lattice planes of the crystal, which occurs only when the scattered waves satisfy Bragg’s law:

$$n\lambda=2d\sin\theta \quad (2.1)$$

Where λ is the wavelength of the X-ray beam, θ is half of the diffraction angle, d is the inter-planar spacing, and n indicates the order of the diffraction. Bragg’s law may also be expressed in vector notation. Let \mathbf{S} , \mathbf{S}_0 be unit vectors along the directions of the diffracted and incident beams, then the vector $(\mathbf{S} - \mathbf{S}_0)$ is parallel to \mathbf{d}^*_{hkl} , the reciprocal lattice vector of the reflecting planes. The moduli of these vectors are: $|\mathbf{S} - \mathbf{S}_0| = 2 \sin \theta$ and $|\mathbf{d}^*_{hkl}| = 1/d_{hkl}$. Thus Bragg’s law can be expressed as:

$$(\mathbf{S} - \mathbf{S}_0) / \lambda = \mathbf{d}^*_{hkl} \quad (2.2)$$

The geometric interpretation of X-ray diffraction photographs is greatly facilitated by Ewald sphere^[80], which involves the reciprocal lattice and a “sphere of reflection”. It is constructed by being centered on the crystal (A) and drawn with a radius R of the reciprocal of the wavelength of X-ray beam $1/\lambda$ (Fig.2.2). From the triangle AOB, it can be

seen that $|OB|=2R\sin\theta=2(1/\lambda)\sin\theta=|\mathbf{d}^*_{hkl}|$. Hence, if the origin of the reciprocal lattice is shifted from the centre of the sphere (A) to the point where the direct beam exits from the sphere (O), then $OB=\mathbf{d}^*_{hkl}$. Thus the condition that the real space lattices satisfy Bragg condition is that the corresponding reciprocal lattice point intersects the Ewald sphere while the origin of the reciprocal lattice is taken at (O).

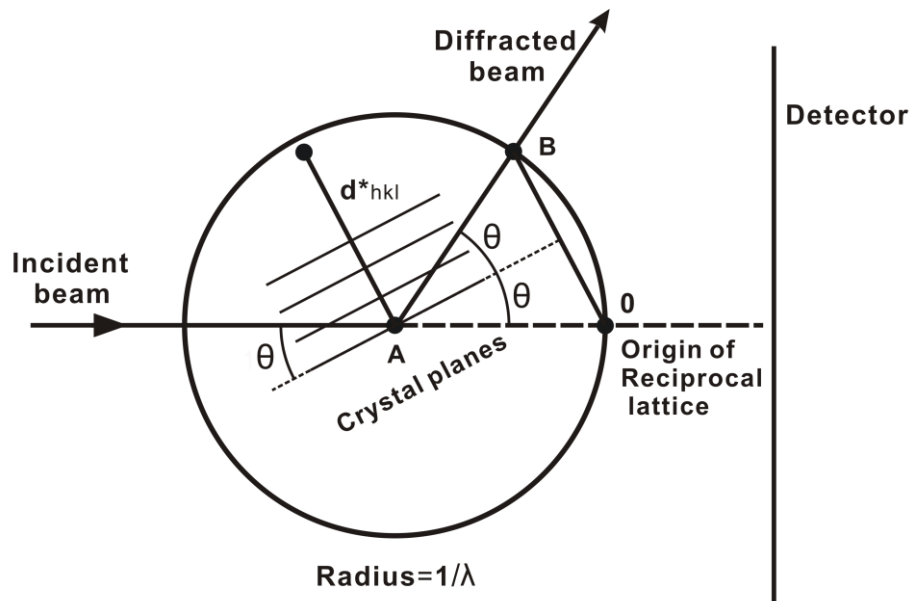


Figure 2.2 The Ewald sphere construction for a set of reflecting planes at the correct Bragg angle.

2.2.1 Synchrotron radiation

The electromagnetic radiation emitted when charged particles are accelerated radially is called synchrotron radiation. It is produced in the injection-accelerating system inside the storage ring, which is like a polygon with the bending magnets at their vertices. Electrons are generated by thermionic emission in the electron gun, and then they pass into the bunching cavity where an alternating electric field causes electrons to bunch together. Next the electrons are injected into the accelerating circle, in which they are accelerated by a varied-frequency electric field to close to the speed of light, and they emit electromagnetic radiation whenever their trajectory is bent by a magnetic field^[81]. The generated synchrotron light finally goes into the beamline where certain wavelengths of the light are selected and focused to perform the X-ray experiment. The radiation emitted by the

orbiting electrons covers an extremely broad range of the electromagnetic spectrum, from the infrared ($\lambda \sim 10^{-2}$ cm) to the hard X-ray ($\lambda \sim 10^{-2}$ nm). The flux of X-rays emitted is many orders of magnitude greater than obtainable with conventional X-ray tubes, making the required time for any single measurement very short and therefore allowing rapid time series measurements with samples undergoing dynamic evolution.

2.2.2 Small angle X-ray scattering

Small angle X-ray scattering (SAXS) is a reliable and economic method for analyzing nanostructured materials. It shares the same physical principle with other X-ray diffraction techniques referred to as wide-angle X-ray scattering (WAXS). The only difference between them is that SAXS has a diffraction 2θ angle range of 0° to roughly 2° or 3° , while WAXS is in the range from 0.5° to 180° ^{d821}. Since the scale of structure and the scattering angle are inversely proportional, SAXS patterns contain structure information on relatively large scales, typically in the size range of 1-100nm. The scattering intensity distribution contains information about particle size, size distribution, particle shapes and orientation, etc.

For the SAXS experiment of AAO template samples, the setup is shown in Fig.2.3. The AAO template samples were mounted on a motorized goniometer in such a way that the long-axis of the nanochannels was set horizontal, and the samples were rotated about the vertical axis in increments of $\Delta\Phi = 1^\circ$ during experiment. The diffraction patterns were recorded from $\Phi = 0^\circ$ (where the channel is parallel to the beam) to close to 90° .

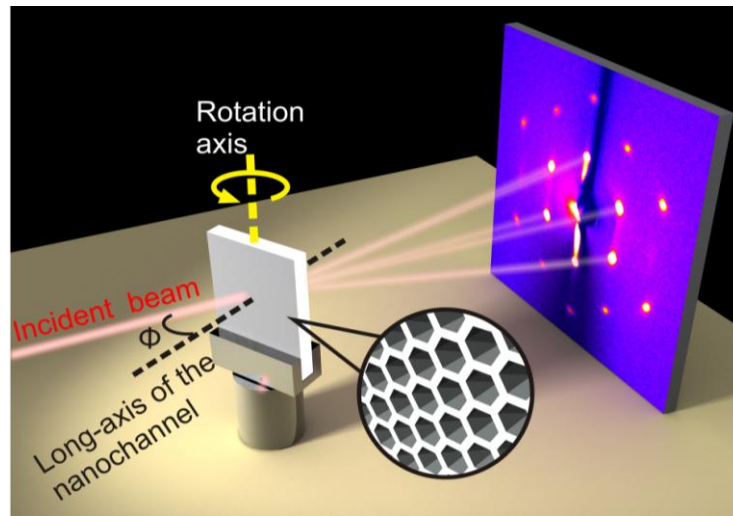


Figure 2.3 Scheme of SAXS experiment set-up for AAO template samples. Φ : the angle between X-ray beam direction and the normal of the template.

The glass capillary samples were studied by an in-house X-ray facility. During the experiment they were mounted on a motorized goniometer in such a way that the long-axis of the tube was set horizontal and perpendicular to the incident X-ray beam (Fig.2.4). During SAXS experiment, the capillary tube was rotated about its long-axis.

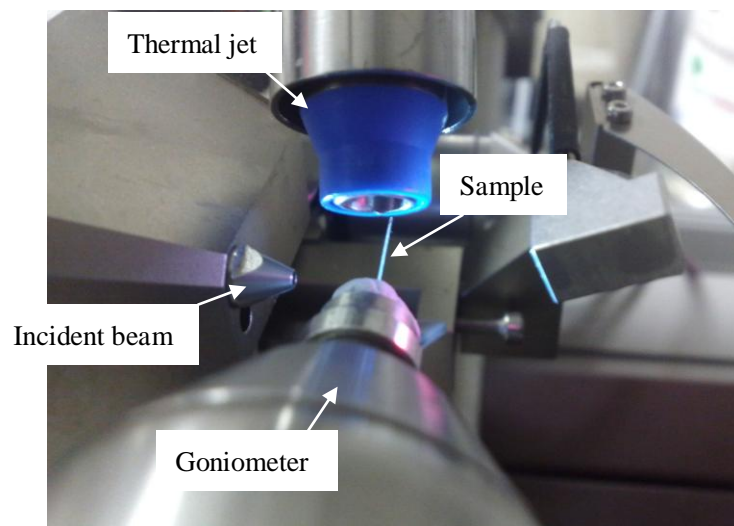


Figure 2.4 X-ray experimental setup for glass capillary samples.

For the in-house X-ray facility, X-rays are produced using a Rigaku MicroMax 007 micro-focus copper rotating anode generator running at 40kV, 20mA; the temperature was controlled by an Oxford Cryosystems Cryostream jet, and data were accumulated using a MarResearch MAR345 image plate detector system.

2.2.3 Grazing Incidence Small angle X-ray scattering

Grazing incidence small-angle X-ray scattering (GISAXS) is a powerful tool to study nanostructured surfaces and thin films. It combines the accessible length scales of small-angle X-ray scattering (SAXS) and the surface sensitivity of grazing incidence diffraction (GID)^[83]. In GISAXS, a grazing incidence angle α is chosen between about half the critical angle α_c of total internal reflection of the film material and several α_c , depending on the depth to be probed. The general setup of GISAXS is relatively quite simple, as schematically drawn in Fig.2.5.

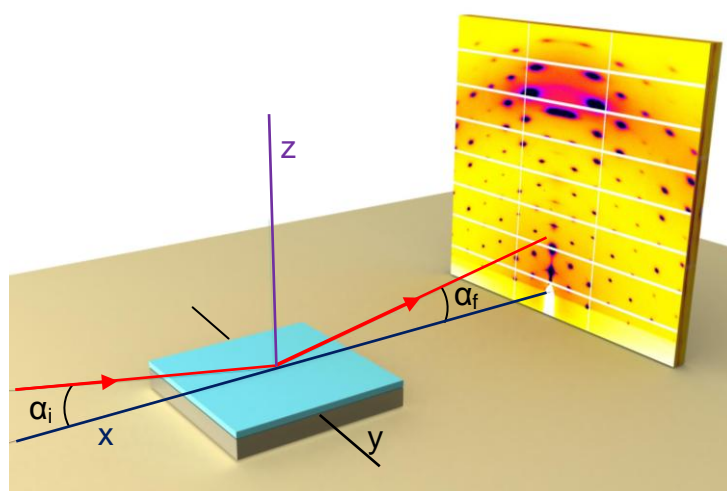


Figure 2.5 Scheme of the GISAX geometry

For thin film samples on substrates, there are two critical angles corresponding to two interfaces: air/sample and sample/substrate interface. If the incident angle used is bigger than both of them, the diffraction pattern comes from the scattering of the primary beam. If the incident angle is lower than the first critical angle, very weak scattering from the evanescent wave, which travels along the surface and penetrates the film only 5-10 nm. If

the incident angle is somewhere in between, the largest scattering cross section is achieved, however, multiple scattering effects have to be taken into account.

GISAXS has several important advantages over transmission X-ray experiment for the investigation of coatings, films and particles on surfaces. First, the x-ray beam path length through the film plane is sufficiently long, thus a highly intense scattering pattern is obtained even for films of nanoscale thickness. Second, the absorption by the substrate is minimized compared to traditional transmission SAXS due to the limited penetration depth of the incoming beam at glancing angles near the critical angle of the substrate on which the film is deposited. Besides, GISAXS is a very useful technique for studying alignment of complex self-assembled LCs on the substrate surface^[84].

In this study, samples for GISAX were prepared by casting thin films on substrate surface via solution. The obtained thin films were heated to isotropic temperature, and then slowly cooled into the liquid crystal phase. GISAXS measurements were carried out at Station I16 at Diamond Light Source (U.K.).

2.2.4 Reciprocal Spacing Reconstruction

In order to facilitate the visualization of diffraction data and determine the geometric relationship between LC columns and nano-cylinders, 3-d diffraction patterns were reconstructed. A C program was written by Dr. X.B. Zeng to collect the data, perform the necessary geometrical corrections and convert the data into a single 3-d array of diffraction intensities in reciprocal coordinates. As the template rotates, the reciprocal lattice points of the LC phase successively cut the Ewald sphere and cause corresponding diffraction peaks on the screen. Each spot (x,z) on the 2-d diffraction image corresponds to a point (q_x, q_y, q_z) in the 3-d reciprocal space. If we assign the x' and z' axes in the q -space to be parallel to the x and z axes of the diffraction image respectively and y' axis as the direction of the incident beam, it can be shown that:

$$\begin{aligned}
q_{x'} &= \frac{2\pi x}{\lambda\sqrt{SD^2 + x^2 + z^2}} \\
q_{y'} &= \frac{2\pi}{\lambda} \left(\frac{SD}{\sqrt{SD^2 + x^2 + z^2}} - 1 \right) \\
q_{z'} &= \frac{2\pi z}{\lambda\sqrt{SD^2 + x^2 + z^2}}
\end{aligned} \tag{2.3}$$

where SD is the sample to detector distance, and λ the X-ray wavelength. As the template is rotated by Φ , the axis of the reciprocal space is rotated by Φ as well. Here the x and z axes are parallel to the template, while the y axis is perpendicular to it, and we have:

$$\begin{aligned}
q_x &= q_{x'}\cos\Phi + q_{y'}\sin\Phi \\
q_y &= q_{y'}\cos\Phi - q_{x'}\sin\Phi \\
q_z &= q_{z'}
\end{aligned} \tag{2.4}$$

From the above equations each spot on the diffraction images can be mapped into the reciprocal space. To construct the 3-d diffraction pattern, a cubic volume in the reciprocal space ($-Q < q_x, q_y, q_z < Q$) is divided into typically 100 x 100 x 100 boxes. For each sample, every intensity point of all diffraction images was mapped to one of these boxes. An averaged intensity value is taken for all the points that fall into each particular box. The 3-d diffraction pattern is then examined in ParaView (Kitware Inc.) using iso-intensity surfaces.

2.3 Microscopy

2.3.1 Optical microscopy

An Olympus BX-50 transmitted-light polarizing microscope with Mettler FP82 hotstage and FP90 control unit was used to observe the texture of the LCs. A Coolsnap-pro digital camera and Image-Pro Plus software were used to capture and process the images. A Nikon Eclipse ME600 microscope in reflection mode was also used in this study. NIS Elements F3.0 software was used to process the obtained images.

2.3.2 Scanning electron microscopy

Scanning electron microscopy (SEM) was used to observe the surface of AAO templates. Samples were coated by carbon film before SEM analysis. The images were acquired using a FEI Sirion Field Emission Gun scanning electron microscope (FEGSEM) with accelerating voltages of 20 kV.

2.3.3 Transmission electron microscopy

Transmission electron microscopy (TEM) was used to characterize the morphology of mesoporous silica nanofibers. TEM experiments were carried out on a Philips EM430 microscope at a voltage of 200 kV.

2.3.4 Atomic Force Microscopy

The atomic force microscope (AFM) is part of a larger family of scanning probe microscopes (SPMs)^[85,86], which also include the scanning tunnelling microscope (STM) and scanning near field optical microscope (SNOM), amongst others. The common feature in all SPM techniques is the use of a very sharp probe to scan across a surface of interest, and record the interactions between the probe and the surface to produce a very high resolution image of the sample, potentially to the subnanometre scale, depending upon the technique and sharpness of the probe tip. In the case of the AFM the probe is a stylus which interacts directly with the surface, probing the repulsive and attractive forces which exist between the probe and the sample surface to produce a high resolution three-dimensional topographic image of the surface. It was created as a solution to the limitations of the STM, which was able to image only conductive samples in vacuum. The AFM has a number of advantages over electron microscope techniques, primarily in being able to take measurements in air or fluid environments rather than in high vacuum. In addition, it is a relatively non-destructive method that allows the imaging of soft matters such as polymers, biological samples and liquid crystals in their native state.

General setup of AFM

A typical atomic force microscope is constructed as shown in Fig.2.6. A sharp tip is located at the end of the cantilever and is used as a probe. A beam of laser is reflected from the back side of the cantilever onto the centre of a position-sensitive photodetector. Any force applied on the tip will cause the cantilever to bend or twist and thus produce a change in the position of the reflected spot on the photodetector, which will be monitored.

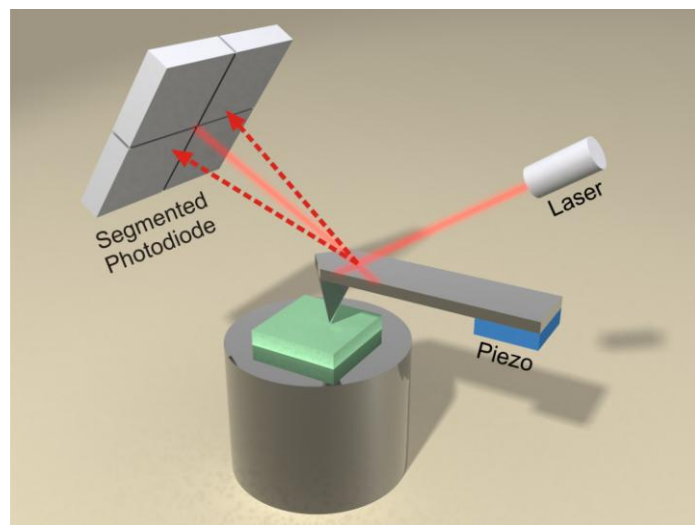


Figure 2.6 Schematic setup of an atomic force microscope. A laser beam is reflected from the back of the cantilever onto a four-segment photodiode. The sample is placed on the top of a piezo tube. In tapping mode, the cantilever is excited by a piezoelectric element to oscillate with a given amplitude A .

The most common configuration for the photodetector is shown on the top left of Fig.2.6 which is of a quadrant photodiode divided into four parts. The difference in the light intensities between the two upper and the two lower segments of the photodiode is measured and converted to a voltage, which is then used as an output signal, describing the deflection of the cantilever to a good approximation, and sent to the computer which controls the piezoelectric scanner. A feedback loop continuously checks the feedback signal, compares it to a user defined setpoint value, and adjusts the tip-sample separation accordingly so that the difference is minimized. Both the sample and the cantilever are mounted on piezoelectric elements, known as the sample scanner or tip scanner,

respectively. While the feedback system is enabled, the scanner moves the tip in x- and y-directions relative to the sample to scan over the surface. The necessary height adjustments of the piezo element (in the z-direction) to keep the feedback value at its setpoint are recorded as a topographical height image of the surface.

Tapping mode AFM

Tapping mode AFM (or “intermittent contact” mode) has been developed as a gentle non-destructive and high spatial resolution mode in order to overcome the limitations of contact mode imaging, in which the probe remains in contact with the sample at all times that it is easy to cause damage to both the probe and the sample. In tapping mode, the cantilever is excited by a piezo element mounted at the base of the cantilever to oscillate at a value close to its resonant frequency. The oscillation is characterized by three parameters, the frequency, the amplitude and the phase lag with respect to the mechanical excitation. The excitation frequency is fixed at the beginning of the experiment, while the other two parameters may be calculated from the photodiode signal and converted to amplitude and phase signals. If the probe is brought down close to the surface, the tip lightly “taps” on the sample surface during scanning, being in physical contact with the sample at the bottom of its swing. The forces acting upon the tip will change the resonant frequency of the tip-sample system. In addition, dissipative interactions cause a damping of the oscillation amplitude from its free value. Thus, as the surface is scanned, the oscillatory amplitude of the cantilever will change as it encounters differing topography. By using a feedback mechanism to alter the z-height of the piezocrystal and maintain a constant amplitude, an image of the surface topography can be obtained.

One of the striking features of tapping mode AFM is the ability to produce simultaneously the topography and the phase images of the specimen’s surface. The phase image is obtained by measuring the shift of the phase signal between the drive frequency and the

frequency with which the cantilever is actually oscillating. With phase imaging it is possible to qualitatively detect the variations in composition, adhesion, friction, and hardness. However, it is difficult to extract quantitative information from them because of their complex combination. Also it should be noted that topography and phase images are closely linked: large changes in material characteristics such as adhesion and stiffness can couple into the topographic image.

In this thesis, tapping mode AFM observations were performed on a Veeco Multimode instrument with Nanoscope IIIa controller. OTESPA probes from Bruker were used.

CHAPTER 3 Planar-anchored Honeycomb Phases in Cylindrical Cavities

3.1 Introduction

Different from conventional columnar phase of discotic LCs where each column is formed by the stacking of individual molecules, the honeycomb phases of T-shaped molecules are much more complex: they are formed by polygonal cylinders in which the rod-like moieties form walls that are interconnected by columns consisting of alkyl or polar groups, and the shape of these polygons can vary from triangles, square to pentagon or to hexagon^[26, 28]. The polygonal cylinders have their preferred ways of coping with the substrate surface since they have anisotropic shapes and different groups at the corner/side of the polygons. When these honeycombs are confined in cylindrical geometries, the physical phenomena must be complex and interesting since there is mismatch between the polygonal network and the curved surface. Besides, the interaction between columns could be expected to be larger than that of nematics or discotics, and the elastic deformation energy of the columns could be high.

It is known that the configuration of LCs in the cylindrical cavity results from the competition between surface anchoring and the elastic energies of the material, and the anchoring condition at the boundary are of particular importance in determining their final orientations^[35,36]. For nematics, it has been observed that their anchoring manner can be preserved in cavities with diameters well below 1 micron^[40-42]. In this chapter, the configurations of several planar-anchored honeycomb phases confined in cylindrical cavities are investigated by means of optical microscopy, x-ray diffraction, and AFM. AAO templates and glass capillaries are used to provide different sizes of cylindrical confinement, varying from a few tens of nanometers to hundreds of microns.

3.2 Porous anodic alumina templates

3.2.1 Square honeycomb phases

The first honeycomb system studied in the AAO template is the square columnar phase (Col_{squ}) formed by facial amphiphiles in which the polar groups are attached to a lateral position on the rigid terphenyl units (Fig.3.1). Two compounds that can form the Col_{squ} phase were examined. Their structures and LC phases are summarized in Table 3.1.

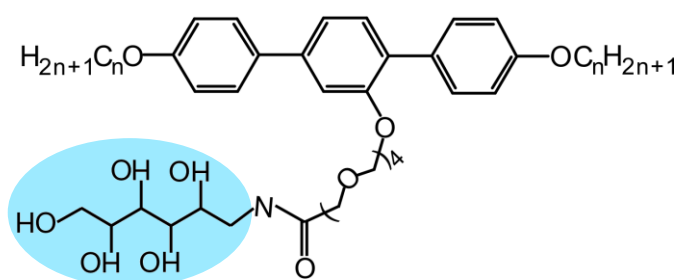


Figure 3. 1 The molecular structure of compound **A₁** and **A₂**. The polar units are covered by the blue shape.

Compound	n	Phase transition (°C)	Lattice parameter/nm
A₁	10	G -8 Col_{squ} /p4mm 94 I	$a_{\text{squ}}=3.9$
A₂	6	Cr 47 Col_{squ} /p4gm 104Colhex 111 I	$a_{\text{squ}}=8$

Table 3.1^[30,87] Molecular chain lengths, LC phase transitions and lattice parameters of compound **A₁** and **A₂**. G=glassy state; I=isotropic liquid; Cr=crystalline phase; Col_{squ} =square columnar phase.

For both compounds, the orientation of their Col_{squ} phase on the flat surface of glass are determined to be planar (the long axis of the columns is parallel to the surface) by polarized optical microscopy (POM). Fig.3.2 shows the birefringence textures of compound **A₁** and **A₂** sandwiched between two glass slides, respectively. The samples were first heated to isotropic liquid, and then cooled to room temperature (R.T) by 0.5 °C/min.

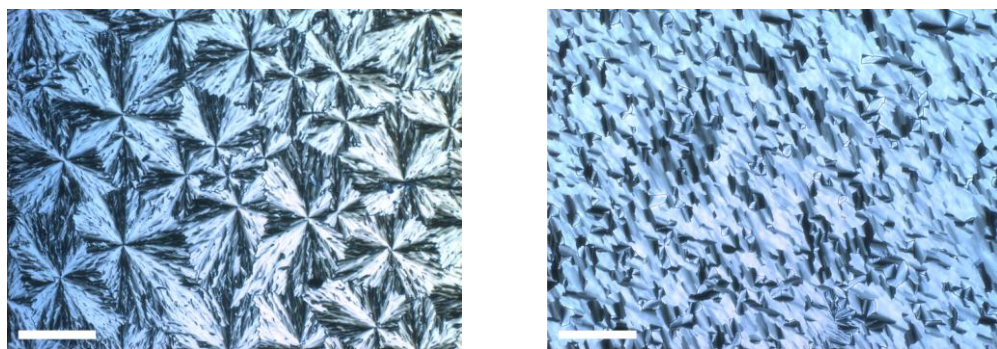


Figure 3.2 Birefringence images of **A1** (left) and **A2** (right) sandwiched between two glass slides, respectively. The bar represents 100 micron.

Compound **A1** can form a $Col_{squ}/p4mm$ phase^[30], the structure of which is schematically drawn in Fig.3.3. The rod-like aromatic cores (grey) form cylinder shells with a square-shaped cross section; the nonpolar alkyl chains form columns (white columns) located at the corners of the squares, which run along the edges of the cylinders and interconnect the cylinder walls; the segregated lateral polar groups fill the inner cell (blue columns). Either inside the white or blue columns, the alkyl chains or polar chains are amorphous. The Col_{hex} phase has only long-range order along the 2-d lattice but is fluid-like along the columns.

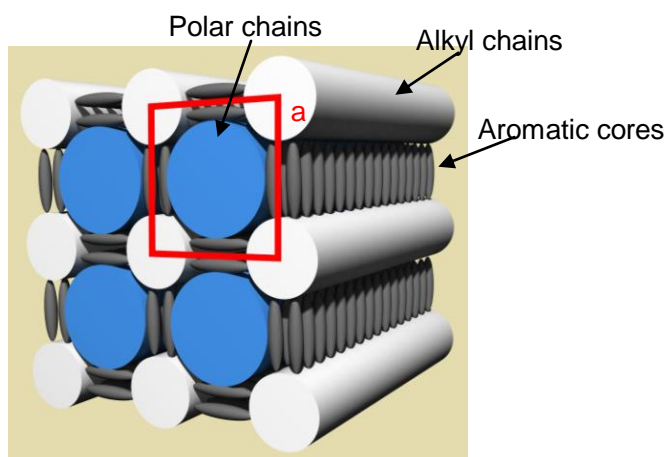


Figure 3.3 Schematic drawing of the Col_{squ} phase of compound **A1**.

The anchoring manner of **A1** on open surface is also planar, as determined by POM. The in-plane orientation of the 2-d lattice on a flat surface was further confirmed by GISAXS experiment. The geometry of GISAXS is described in chapter 2. It can be seen in Fig.3.4 that the (100) plane is parallel to the substrate surface, which means the square cell lies with one side parallel to the LC/solid interface.

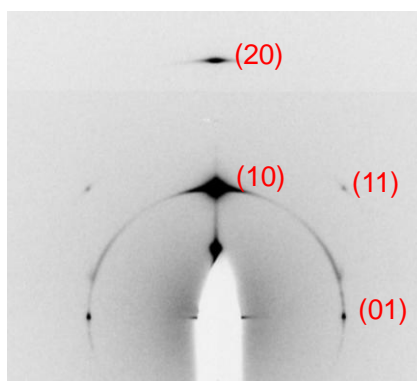


Figure 3.4 GISAXS pattern obtained from the thin film of compound **A1** casted on silicon wafer.

3.2.1.1 **A1**

A1 in 400 nm AAO template

Compound **A1** was first filled in a 400 nm AAO template. Fig.3.5 shows the scanning electron microscopy (SEM) images of the front surface of the AAO template before and after being filled with **A1**. It can be seen that the pores are fully filled while there is no bulk residue on the surface.

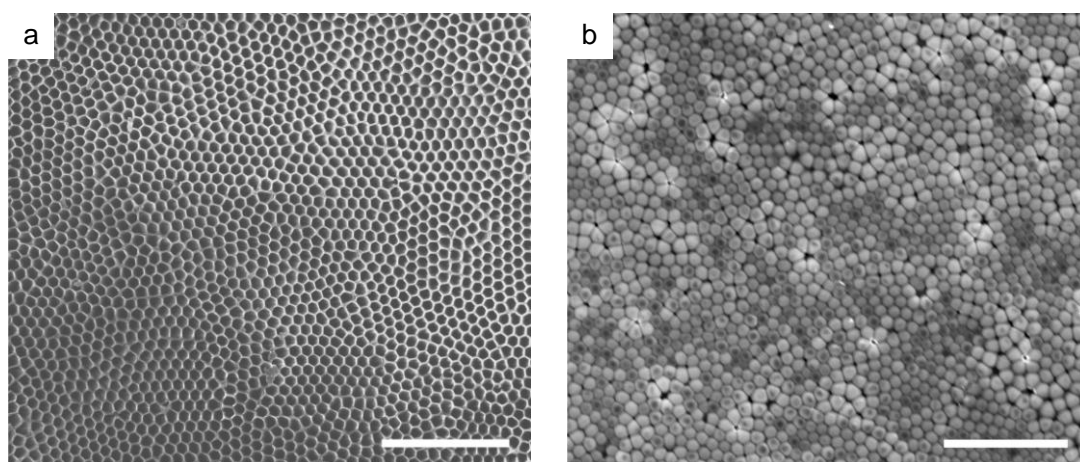


Figure 3.5 SEM images of AAO template with a diameter of 400 nm: a) empty; b) filled with **A1**. The bar=5 μm .

The orientation of **A1** in the template was first studied by SAXS (the setup of the experiment is described in chapter 2). Prior to SAXS experiments, the filled template was heated to 100 $^{\circ}\text{C}$ and cooled slowly (0.1 K min^{-1}) into its LC phase in order to erase any flow-induced alignment and establish an equilibrium organization. For compound **A1**, the strongest reflection is the (10) reflection of the 2-d square lattice. Selected diffraction patterns are shown in Fig.3.6. The Φ -angle between the X-ray beam and the pore axis is indicated below each pattern. A uniform (10) diffraction circle appears at $\Phi = 0^{\circ}$ (incident beam parallel to the channel axis) as shown in Fig.3.6a. As Φ increases, the intensity condenses on the equator (equator and meridian are defined here as perpendicular and parallel to the long-axis of the nanochannel; thus here equator is vertical). However, as Φ reaches 50° (Fig.3.6c), a new set of (11) intensity maxima appears near the meridian and, with Φ increasing further, these split and move rapidly away from the meridian. At the largest accessible Φ angle of about 75° , another set of (10) spots show up on the meridian and the positions of the four intensity maxima on the (10) ring describe close to a regular square.

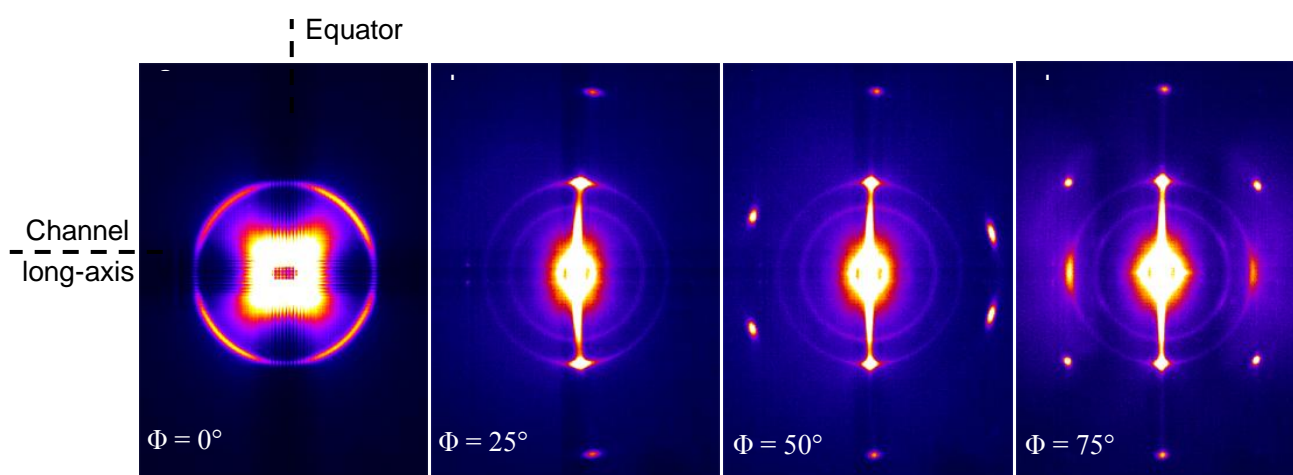


Figure 3.6 X-ray diffraction patterns of 400 nm AAO membranes filled with **A1** recorded at a series of rotation angles Φ indicated in each image. The rotation axis is vertical, the pore axis is in the horizontal plane. Note that the four-quadrant sectorization in the $\Phi=0^{\circ}$ patterns is an artefact due to the saturation of the detector with the intense central scatter originating from the AAO nanopores.

In order to facilitate the understanding of this change of the diffraction pattern with Φ angle, 3-d diffraction pattern was built combining all those recorded images. The result of the complete reciprocal space mapping of the three strongest small-angle reflection groups $\{10\}$, $\{11\}$ and $\{20\}$ for **A1** confined in the AAO template, are shown in Fig.3.7. The contour map shows a single-level isointensity surface chosen so as to capture the essence of the 3-d intensity distribution in reciprocal space coordinates. It can be seen that the map is consistent with the square 2-d reciprocal net being rotationally averaged around a $[10]$ axis, i.e. an axis in the net plane rather than perpendicular to it. According to the geometric relationship between the template and the incident x-ray beam, this $[10]$ axis can be determined to be parallel to the long-axes of the nanochannel, as indicated by the black dashed line in Fig.3.7.

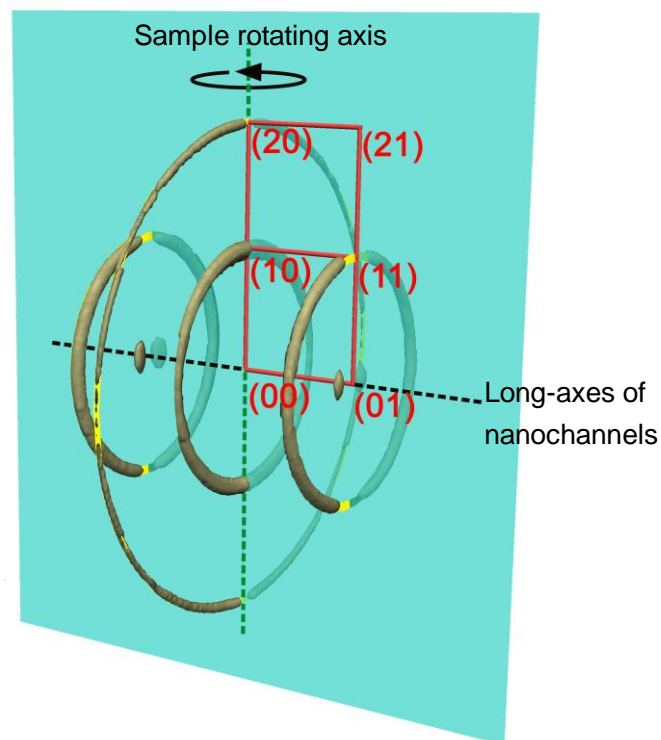


Figure 3.7 3-d diffraction patterns of **A1** confined to 400 nm AAO in reciprocal space coordinates. The isosurface is set to an intensity level such that the reciprocal space distribution of all three strongest reflection groups, i.e. $\{10\}$, $\{11\}$ and $\{20\}$, could be shown simultaneously. The dashed black line indicates the orientation of the nanopores in the AAO. The continuous background scatter predominantly originating from AAO was subtracted by means of a custom-written 3-d fitting algorithm. The breaks in the rings are mainly due to absorption of X-rays by the AAO. They are most prominent in

the plane containing the nanopore axis and the axis of rotation (the blue semitransparent plane), as diffraction for $\Phi = 90^\circ$ is not accessible. The yellow lines are guides to the eyes.

Fig.3.8 illustrates schematically the expected distributions of reciprocal $\{10\}$ points of a square columnar phase for the three hypothetical possible configurations of columns within cylinders, i.e. axial (a), radial (d) and circular-concentric (e).

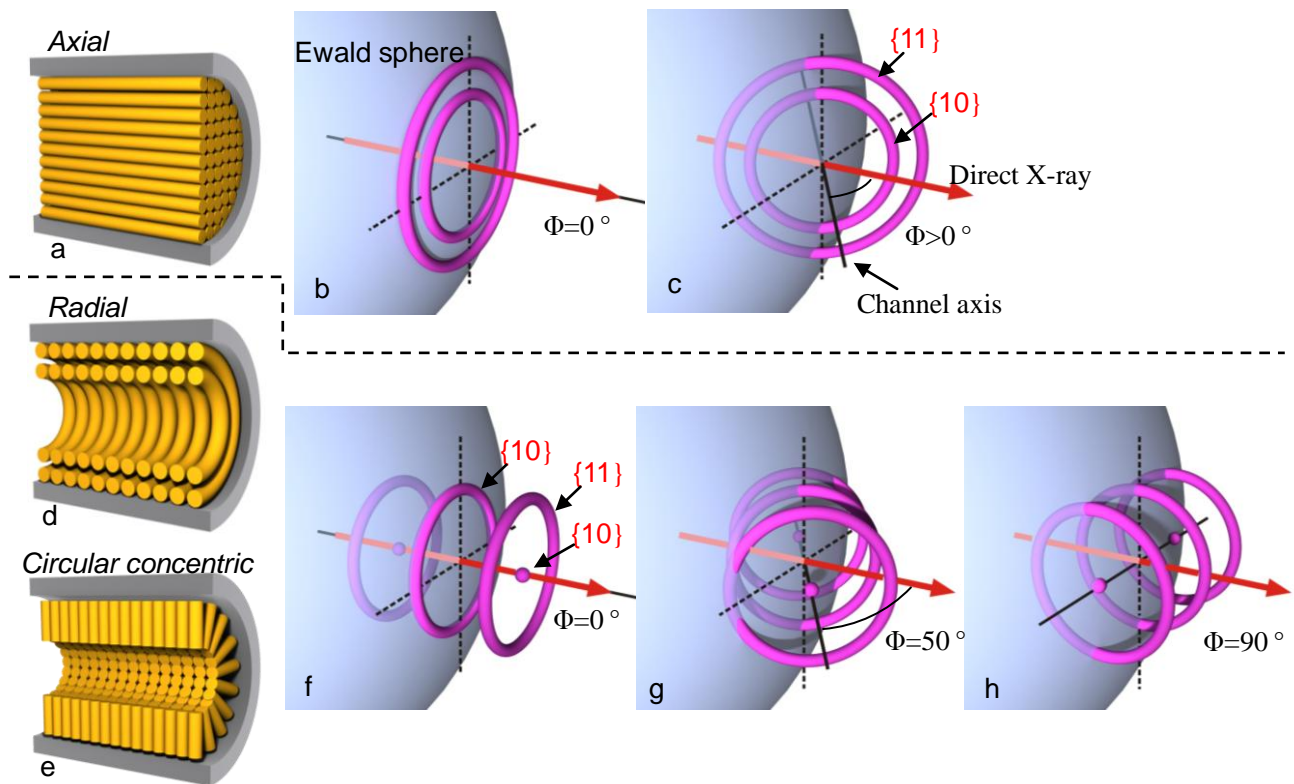


Figure 3.8 a,d,e) Three possible special configurations of columns of the Col_{squ} phase (yellow) in a cylindrical nanochannel: a) axial, b) radial and c) circular concentric; (b,c,f,g,h) schematic of the reciprocal space (rings) and the Ewald sphere of diffraction for the corresponding orientations of the columns. The $\{10\}$ and $\{11\}$ reciprocal points are distributed differently in (b,c) and (f,g,h).

If the orientation of the columns was axial (a), i.e. if the columns were parallel to the nanochannel axis and the 2-d lattice was perpendicular to the channel axis, the situation depicted in the top row of Fig.3.8 would have applied. All reciprocal points would have been in the equatorial plane and the rotational averaging about the pore axis would have created a series of co-planar concentric rings (Fig.3.8b). Thus for any $\Phi > 0$ we would have observed diffraction spots on a vertical line or close to it, i.e. where the

rings cut through the Ewald sphere. However, as seen in Fig.3.6, at $\Phi > 45^\circ$ nonequatorial $\{11\}$ reflections appear. In the radial (b) and circular-concentric (e) situations, the columns are perpendicular to the long-axes of the channels and the 2-d lattice is always on planes that are parallel to and rotating around the channel axis. Since the $[10]$ direction is perpendicular to the channel axis, the reciprocal space lattice points rotate about a $[01]$ direction and form rings arranged exactly as shown in Fig.3.7.

It can be clearer when we rotate the reciprocal space of these possible configurations, respectively. The middle and the right columns of Fig.3.8 show the reciprocal space when, respectively, $\Phi = 0$ and $\Phi > 45^\circ$. In Fig.3.8 (b,c) all reciprocal $\{10\}$ points are condensed in one ring. For $\Phi = 0$ the ring is sufficiently close to the Ewald sphere to give a uniform circle in the diffraction pattern, the same as in Fig.3.6a. As the $\{10\}$ reciprocal ring rotates with increasing Φ the Ewald sphere intersects it only in two points near the equator, as indeed observed (e.g. Fig.3.6b, $\Phi=30^\circ$). However, the experimental observed appearance of meridional diffraction arcs and their subsequent splitting into four spots is inconsistent with situation in Fig.3.8(a-c). Hence, the axial alignment of the columns could be ruled out.

For radial and tangential configurations, on the other hand, the $\{10\}$ and $\{11\}$ reflection groups are separated in three rings. Fig.3.8 shows how the three rings are generated by the rotation of the 2-d reciprocal plane about a $[10]$ direction. According to Fig.3.8 (f,g), at $\Phi = 0$ again a uniform $\{10\}$ diffraction circle is observed, which also condenses at the equator for $\Phi > 0$. In this case for Φ around 45° four additional arcs appear as the other two rings of the $\{11\}$ group intersect the Ewald sphere. The left-right asymmetry observed in Fig.3.6c for $\Phi = 50^\circ$ is due to the curvature of the Ewald sphere – see Fig.3.8g. Thus, the observed changes in the diffraction pattern in the entire range of Φ angles (Fig.3.6) and the reconstructed reciprocal space map (Fig.3.7) are consistent with scenarios involving either radial or tangential orientations of the columns displayed in the bottom half of Fig.3.8.

Since the columns are planar-anchored on the flat surface of glass which has similar polarity as that of alumina, inside the nanochannels of AAO the columns should be planar-anchored on the wall surface as well. Under this anchoring condition, the radial configuration could be ruled out. However, it remains unclear what happens close to the symmetry axis of the nanochannel since the concentric ring arrangement can not extend to the center of the cylinder due to the increasing curvature. The core can either be filled with isotropic liquid, or by hexagonal mesophase with defects. However, SAXS experiment can only give the averaged information over the entire irradiated volume which covers many nanopores and is insufficient to solve this problem. Thus atomic force microscopy (AFM) is employed to further explore the orientation of columns inside individual nanochannel. The AFM measurements were performed using a Nanoscope IIIa Multimode SPM in tapping mode. Aluminium-coated silicon cantilever with a tip radius of 7-10nm was used. First the AAO template (diameter of 400 nm) filled with **A1** was heated to 100 °C and cooled to R.T. at 0.1 °C/min. AFM observation was first performed on the top surface where the nanopores end. It was hoped that the orientation of the LC columns inside the nanopore could be preserved to the very opening where the LC/air interface is involved, and also the top surface could be smooth enough for the tapping mode scanning. The obtained phase images are shown in Fig.3.9. It can be seen in Fig.3.9a that one pore at the lower left corner is overfilled with the material, while the other three at the upper right are well filled and flat at the center. Further zoom in scanning was performed on the central region of these well filled pores. In the higher resolution image (Fig.3.9b) individual columns that form concentric rings can be seen clearly.

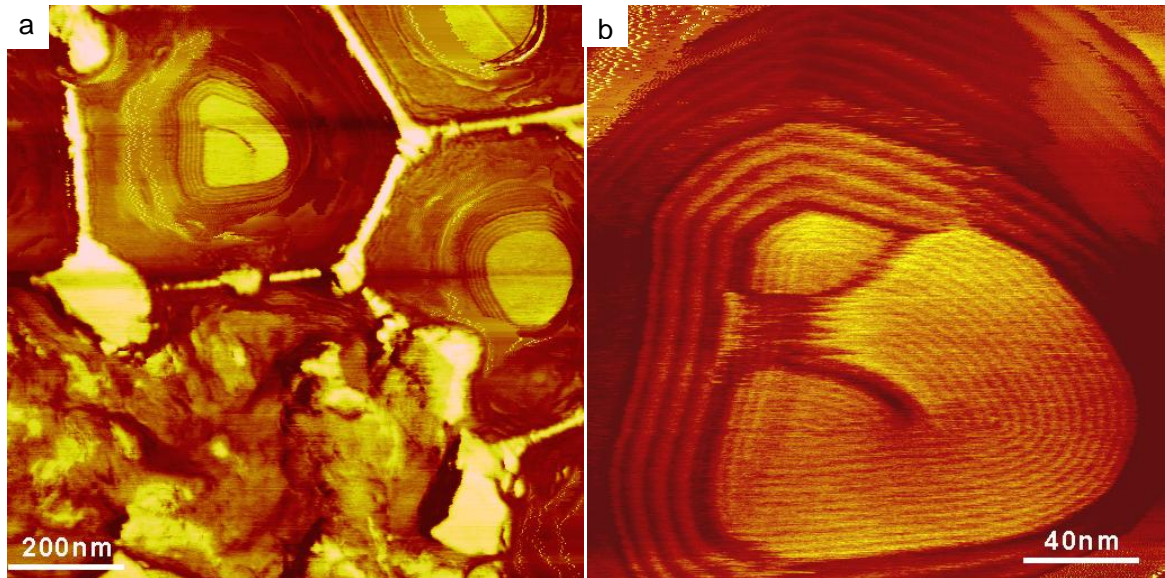


Figure 3.9 AFM phase images obtained from the top surface of 400 nm AAO template filled with **A1**. b) is higher resolution image from a).

The width of the narrow cylinders packed at the centre is about 3.9nm, which is consistent with the square lattice parameter calculated from the SAXS data. A screw dislocation can be seen at the center of the pore, which released the bend deformation. The outer wide bundles could be artifact due to the stiff edge at the end of the nanopore where the probe couldn't reach the sample properly and was "scanned" by the edge instead.

This result indicates that the columns are concentric circular close to the wall of the nanochannel, while traversing straight through at the centre with defects. However, the orientation of LC columns at the opening of the nanopores could be different from that inside channels, and the inner part of the template needs to be further explored. In order to see directly the orientation of LC columns inside the nanochannels, the AAO template filled with **A1** was cracked along its channel axes. We first tried to crack an empty 400 nm template by applying a pressure on the top surface. The fracture surface was examined by SEM as shown in Fig.3.10.

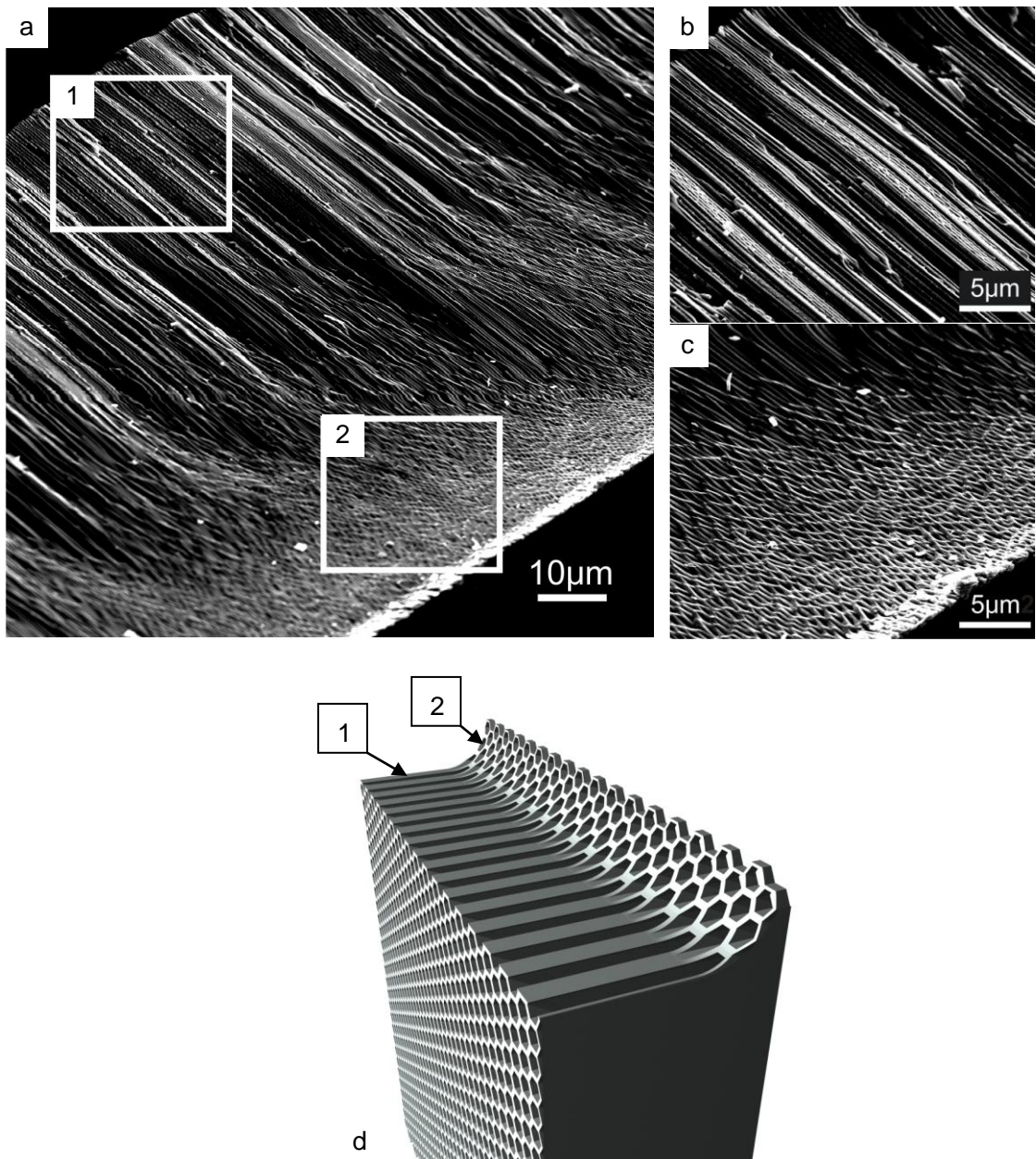


Figure 3.10 a-c) SEM images of the fracture surface of empty AAO template with a diameter of 400 nm. b) and c) are zoom-in images from the frame 1 and 2 in a), respectively. d) Schematic drawing of the cracked AAO template. The markers indicate area 1 and 2 in a), respectively.

In Fig.3.10a, groves and holes can be seen, as indicated in area **1** and **2**. Fig.3.10b and c are the higher resolution images of area **1** and **2**, respectively. It is clear that these terrains are formed when the fracture surface cuts the template either parallel or at an angle to the nanochannels. Fig.3.10d is a schematic drawing of the cracked AAO template. This kind of

crack turns out to benefit the AFM observation later since it exposes different surfaces of the confined LC phase. Tapping mode AFM experiment was then carried out on the fracture surface of the 400 nm AAO template filled with **A1**. The sample was observed at R.T. immediately after being snapped in order to avoid any reorientation of the LC columns.

The tilted-cut area (area **2** in Fig.3.10a) was first examined and the results are shown in Fig.3.11. It can be seen that the fracture surface is relatively smooth and clean. In this area the nanopores were cut into ellipses (Fig.3.11a). Fig.3.11b is a zoom-in image from Fig.3.11a which shows only one pore. It appears that the LC columns form circular concentric bundles and two strength $S=1/2$ disclinations at the centre. In Fig.3.11c, curved steps on the background of the tilted square lattice are clearly observed. This morphology is formed when the fracture surface cuts the square array at an angle; in those areas the fracture surface appears to be close to the (210) crystallographic plane. Fig.3.11d shows the zoom-in image of the center of Fig.3.11a. It can be seen that columns go straight through the pore center, connecting the two disclinations.

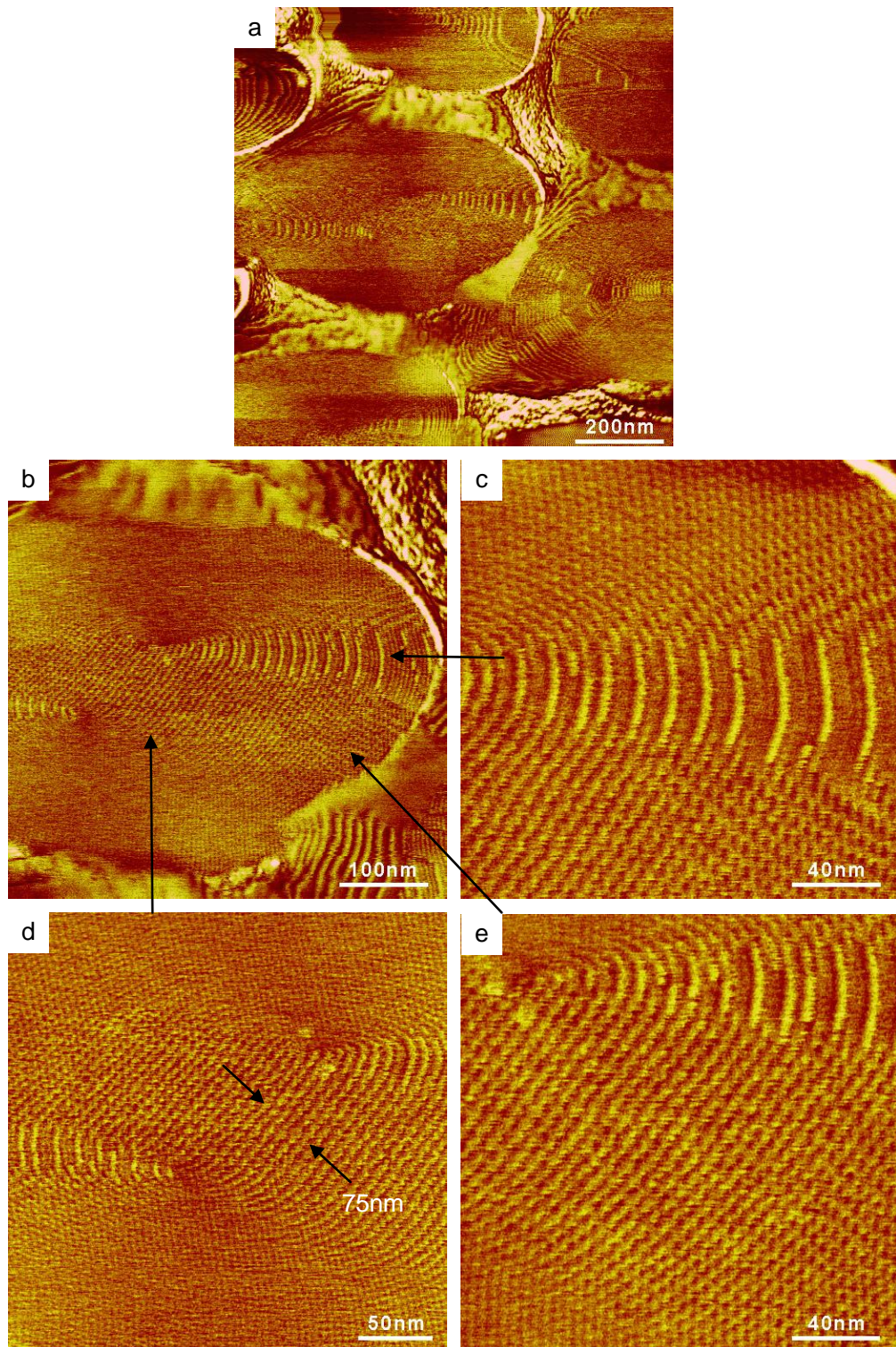


Figure 3.11 Tapping mode AFM phase images obtained on the tilted-cut fracture surface of the 400 nm AAO template filled with **A1**; b) zoom in image of one pore in a); c), d) and e) are high resolution images magnified from b); The small steps in c) are truncated columns left on the top of the surface. Two strength $S=1/2$ disclinations can be seen at the center in d).

Schematic drawing of the circular concentric columns cut at an angle is shown in Fig.3.12. On the right of Fig.3.12 it shows how it looks like when the part of columns above the cutting plane is removed.

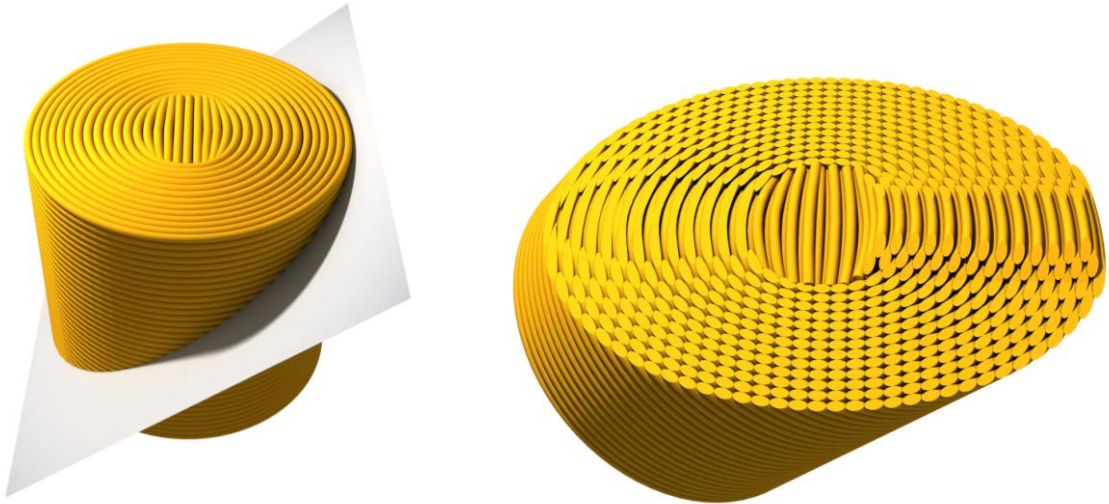


Figure 3.12 Schematic drawing of the circular concentric columns being tilted cut by a plane.

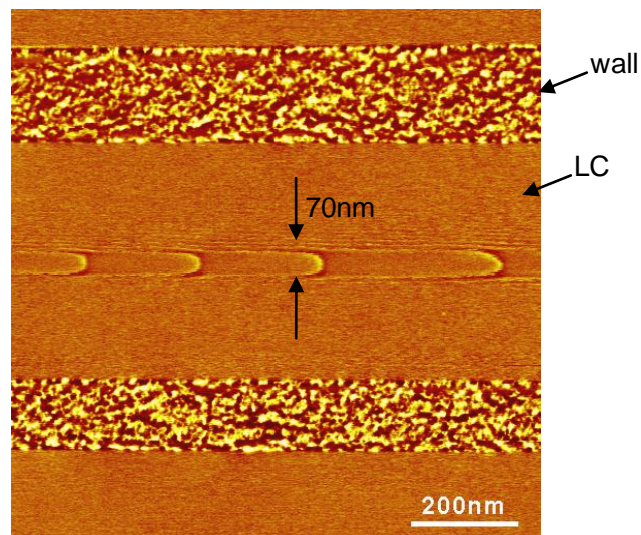


Figure 3.13 AFM phase image showing a nanochannel of the 400 nm AAO template filled with **A1** cut by the fracture surface nearly parallel to the long-axis. The rough areas are AAO.

Turning to the parallel-cut fracture surface, it shows a band structure running along the symmetry axis of the nanochannel (Fig.3.13). The width of the band is about 70nm, which is close to the width of the straight-grown columns that connect the two disclination, as

marked in Fig.3.11d. We suggest this is where the fracture plane cutting across the straight columns at the center of the cylinder and running between the two disclination lines parallel to the nanochannel. Thus the AFM observation gives decisive support for the concentric circular configuration with two disclination lines running parallel to the symmetry axis of the cylinder.

Now that we have determined the configuration of the columns inside the nanopores, the next question we need to answer is why the columns choose to orient perpendicular rather than parallel to the channel axis, since the latter seems to be a more reasonable solution for columns grown in 1-d cylinders where planar anchoring is favored. In circular concentric configuration the densely packed plane of the square lattice is parallel to the surface, as indicated previously by the SAXS patterns in Fig.3.4. Thus the free energy mainly comes from the bend deformation of the columns. On the other hand, in axial orientation where the columns are parallel to the channel the bend deformation would be totally released. However, since a dense plane of the 2-d square lattice prefers to lie parallel to the wall surface, it couldn't match the curved surface without distortion, particularly serious when approaching the center, as schematically drawn in Fig.3.14. Thus we speculate that axial orientation of columns is prohibited by the strain energy of the 2-d lattice caused by the curved surface. The lattice strain elastic constant appears to exceed the bend constant k_{33} by far.

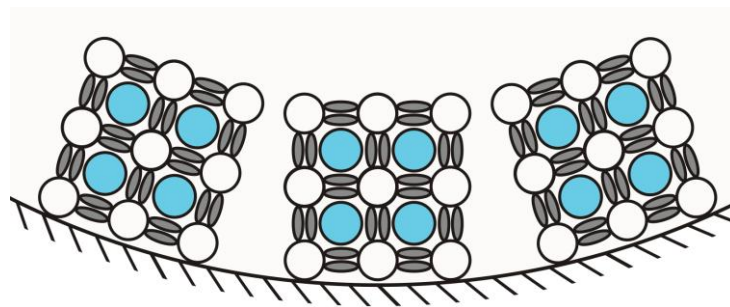


Figure 3.14 Sketch of the axially oriented Colsqu columns of compound **A1** lying on the wall surface of the 400 nm AAO template. The column axis is perpendicular to the plane of the paper. The curvature of the surface is not exactly to scale with the size of the square lattice.

A1 in 60 and 20 nm AAO templates

The orientation of the columns of A1 in 60 and 20 nm AAO templates were further examined by SAXS. As could be expected, the diffraction spots are considerably broader. The diffraction patterns (Fig.3.15) reveal that the columns are still perpendicular to the channel axis even in 20 nm AAO template and the (10) plane keeps parallel to the surface. Besides, it can be seen that the square lattice is distorted: the (10) reflections on the equator are apparently located at a smaller diffraction angle than the (01) reflections on the meridian, as indicated by the blue dashed circles. This means part of the square lattice was distorted into rectangular, with the average radial spacing $d_{(10)}$ bigger than the axial $d_{(01)}$. This unequal spacing can be explained by the model proposed for the configuration of A1 in 400 nm AAO template. Considering the size of the pores, the arrangement of A1 in 60 or 20 nm pores should be similar to that at the centre of the 400 nm pores where the columns are in the bipolar configuration, as schematically drawn in Fig.3.9b. For this configuration, the diffraction mainly comes from the splayed columns at the centre which take up most the volume of the cylinder and gives rise to the increased spacing $d_{(10)}$. Also the bipolar configuration may release some of the bend deformation while the increased curvature may largely distort the 2-d lattice if the columns go axial, which keeps the LC columns from axial orientation.

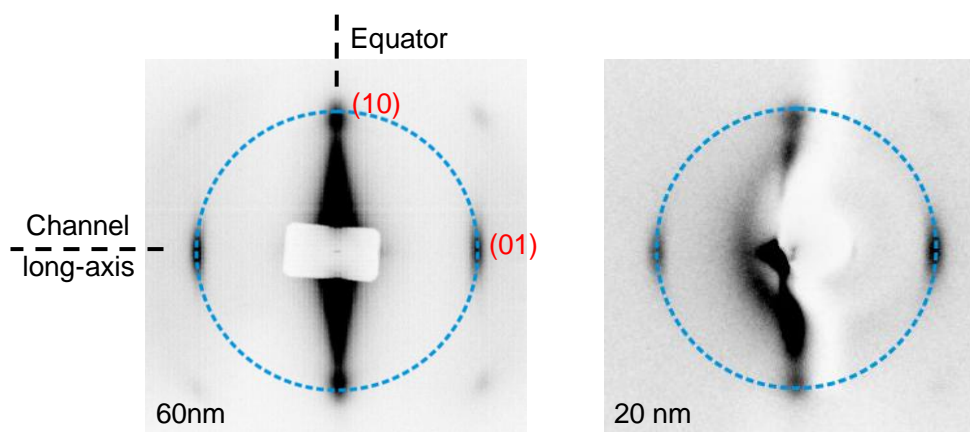


Figure 3.15 SAXS patterns of compound A1 filled in 60 and 20 nm AAO templates recorded at $\Phi=80^\circ$, respectively. The blue dashed circles are just guide to compare the d-spacing of (10) and (01) spots.

3.2.1.2 A2

Turning to compound **A2**, it has a shorter terminal group, and displays two different liquid crystalline phases^[87] (Table 3.1). In this chapter, only the p4gm phase was examined. The Col_{squ}/p4gm phase is also made up of cylinders, but in this case with a pentagonal cross-section, as shown in Fig.3.16. The polar lateral chains fill the interior of these cylinders, and the columns of the alkyl chains interconnect the cylinder walls. These pentagonal cylinders can only organize in a regular and periodic way if they form cylinder pairs (indicated by dotted green lines). These pairs have symmetry higher than that of the individual pentagonal cylinder and adopt a 90 ° turn herringbone-like packing, leading to the p4gm-lattice.

The periodic organization of pentagonal cylinders is the most remarkable cylindrical phase since the regular pentagon with identical sides and angles cannot tile up the plane. However, the liquid crystalline state allows sufficient deformation of the pentagon as required for the regular tiling. The rigid aromatic units also tend to restrict the side length of the polygons within relatively narrow limits, giving rise to columns with a well-defined polygonal shape.

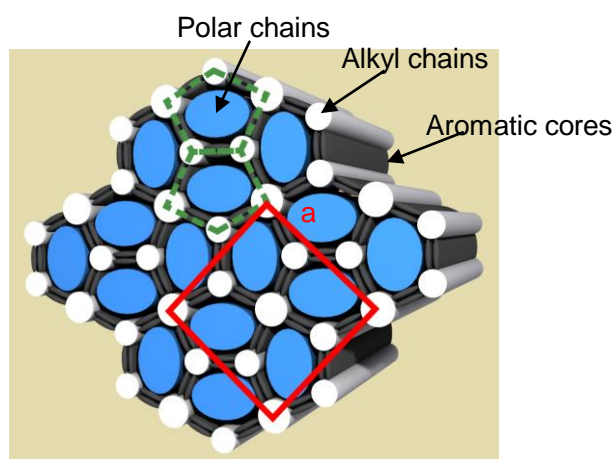


Figure 3.16 Model of the organization of compound **A2** in Col_{squ}/p4gm phase: blue columns incorporate the polar lateral groups; white columns incorporate the alkyl chains interconnecting the terphenyl units at the nodes. The green dashed lines indicate the pentagonal cylinder pairs.

The GISAXS pattern (Fig.3.17a) obtained from a well oriented film of **A2** on silicon wafer reveals that the 2-d square/p4gm lattice exhibits two orientations with respect to the substrate surface: the (10) plane in orientation **1** (as indicated by the red lattice), and the (21) plane in orientation **2** (blue lattice), are parallel to the surface, respectively. The organization of molecules of **A2** in the unit cell is schematically drawn in Fig.3.17b. It can be seen that when the lattice is cut along the (20) or (21) planes by the substrate surface, the interconnected pentagonal cells require least deformation, which is similar to the situation for **A1** where the square lattice chooses to be cut along the (10) plane.

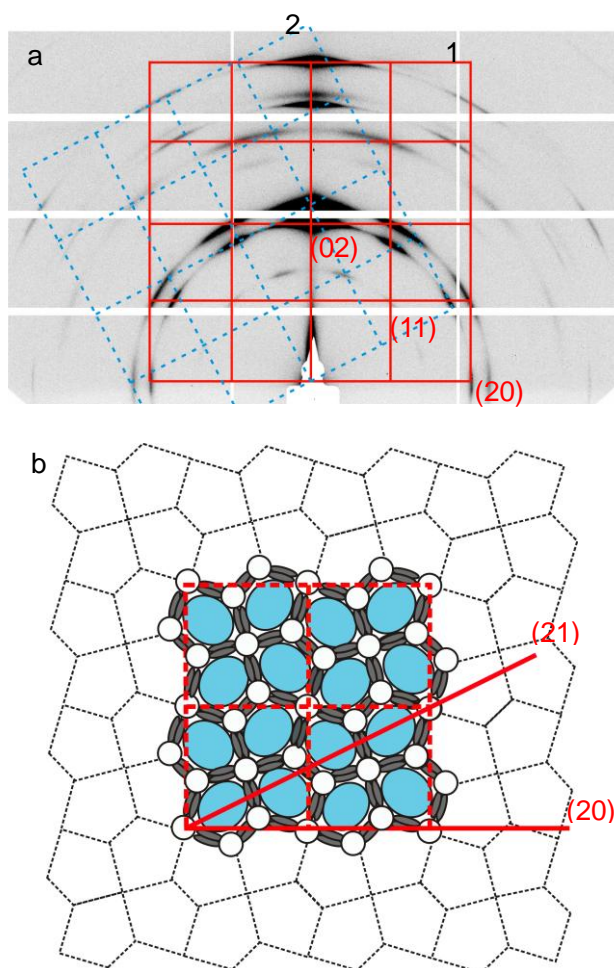


Figure 3.17 a) GISAXS pattern obtained from a thin film of **A2** casted on a silicon wafer; b) Schematic drawing of the 2-d lattice of $Col_{squ}/p4gm$ phase tiled by identical pentagons.

The configuration of Compound **A2** in 400 nm AAO template was studied by SAXS using

the same procedure and setup as that of compound **A1**. Fig.3.18 shows the SAXS pattern at $\Phi=79^\circ$ when the sample was heated from R.T to 60°C . The pattern can be indexed on a $p4gm$ lattice. It indicates that the columns of **A2** are oriented perpendicular to the long-axis of the nanochannels. Considering the planar anchoring condition of the columns, we conclude that the pentagonal columns also form concentric circular configuration in the nanochannels.

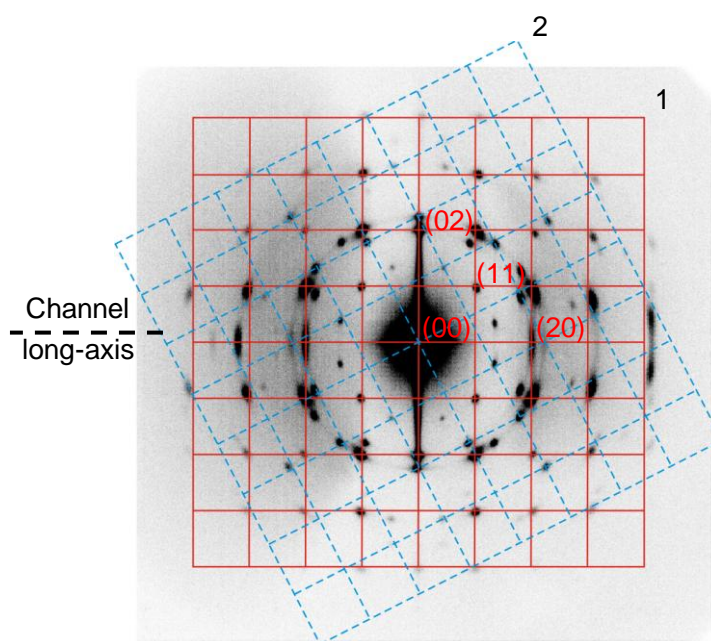


Figure 3.18 SAXS pattern of compound **A2** filled in 400 nm AAO template recorded at $\Phi=79^\circ$; The red and dashed black lattices indicate orientation **1** and **2** of the 2-d lattice, respectively.

Furthermore, the 2-d reciprocal lattice also adopts two preferred orientations with respect to the axes of the nanochannels, as indicated by the red and the blue dashed lattices. Comparing the diffraction pattern in Fig.3.17 with that in Fig.3.18, it can be seen that the two preferred orientations are the same: the (10) plane in orientation **1** and (21) plane in orientation **2** are both parallel to the LC/substrate interface, either with respect to the flat surface of the silicon wafer or the curved wall surface of the AAO nanochannel. It suggests that the columns with pentagonal cross-sectional shape lie on the surface of the curved wall in the same manner as that on the flat surface, in which the 2-d lattice is the least deformed

after being cut by the LC/solid interface. Besides it can be seen that the orientations of the 2-d lattice on the flat open surface are less fixed than that inside the nanochannel, as implied by the arch-shaped diffraction intensities in Fig.3.17a and the sharp spots in Fig.3.18. This could be explained by the fact that inside the nanopores the interface between the LCs and solid surface is much larger than that on the free surface, thus the surface effect on the orientation of the 2-d lattice is much stronger.

3.2.2 Hexagonal honeycomb phases

The second honeycomb phase investigated is a columnar hexagonal phase (Col_{hex}) formed by a facial amphiphile (compound **A3**^[87]) with relatively short terminal chains, as shown in the upper image of Fig.3.19. The model of the hexagonal honeycomb phase formed by **A3** is schematically drawn on the left of the image. In this model, the blue columns contain the polar laterally groups and arrange on a hexagonal 2-d lattice. Each polar cylinder is framed by six rod-like terphenyls (grey) in a stratum within the cylinder shells. The white columns at the cell corners contain alkyl terminal groups, which interconnect the wall of the cylinders.

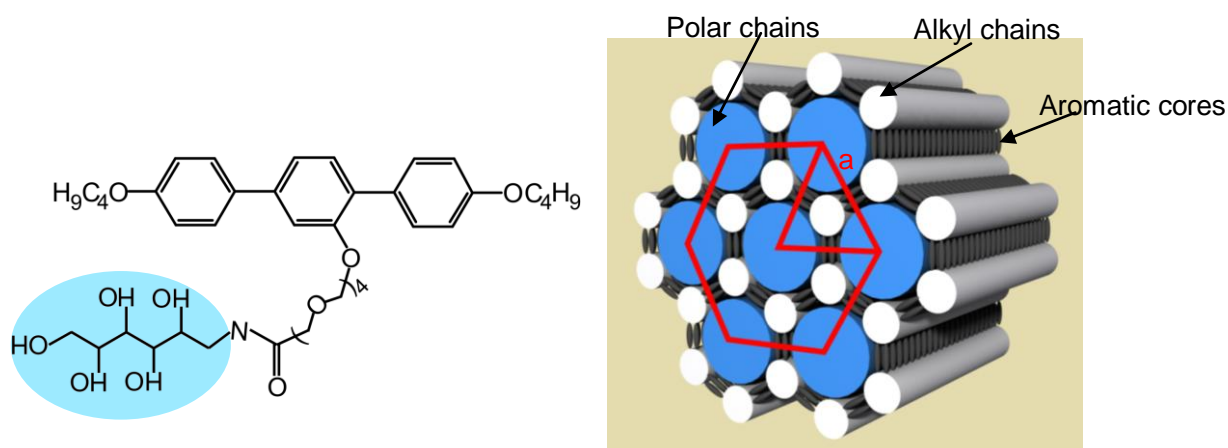


Figure 3. 19 The molecular structure of compound **A3** and the model of the molecular organization in the Col_{hex} phase. The polar units are covered by the blue shape. Phase transition temperatures: Cr 56 °C $\text{Col}_{\text{hex}}/\text{p6mm}$ 97 °C I; Col_{hex} phase lattice parameter: $a_{\text{sq}}=4.2\text{nm}$.

Fig.3.20a shows the birefringent texture of compound **A3** sandwiched between two glass slides. The typical fan-like texture indicates the columns are planar-anchored on the surface. The orientation of the 2-d lattice on the surface is further determined by GISAXS experiment. Fig.3.20b shows the GISAXS pattern obtained from a thin film of **A3** cast on the silicon wafer. It can be seen that the (10) plane is parallel to the substrate surface.

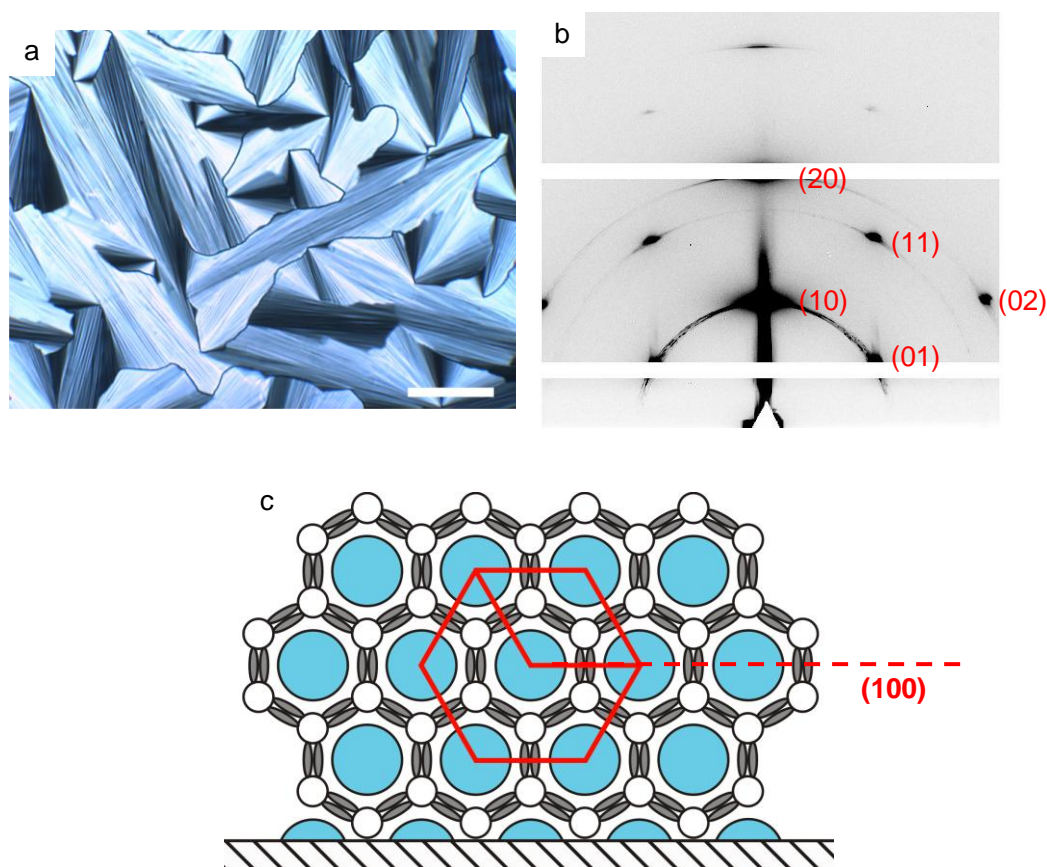


Figure 3.20 a) Birefringent texture of compound **A3** sandwiched between two glass slides (the bar represents 100 micron); b) GISAXS pattern of a thin film of **A3** cast on the silicon wafer; c) Schematic drawing of the 2-d hexagonal lattice of **A3** lying on the substrate with its (100) plane parallel to the surface. The axis of the column is perpendicular to the plane of the paper.

The orientation of the hexagonal lattice on the surface as determined is schematically drawn in Fig.3.20c: the hexagonal lattice is cut through by the substrate surface parallel to the (10) plane. It can be seen that for the hexagonal lattice, it is most intact when being cut in this way. Thus this oriented anchoring could be explained by the same mechanism as that of the $p4mm$ or $p4gm$ square lattice on the surface: the 2-d lattice chooses to be cut in a way that the lattice distortion energy is the lowest.

A3 in 400 nm AAO template

The orientation of **A3** in the AAO template with a diameter of 400 nm was then studied by SAXS experiment. The selected diffraction pattern is shown in Fig.3.21. The strongest reflection for **A4** is the (10) reflection of the 2-d hexagonal lattice. As Φ increases, the intensity condenses on the equator. When Φ reaches about 55° , a new set of (10) intensity maxima appears near the meridian and split and move rapidly away with Φ increasing further. At the largest accessible Φ angle of about 80° , the positions of the six intensity maxima on the (10) ring described close to a regular hexagon. Analogous behavior is also observed for the (20) reflections, taking account of the curvature of the Ewald sphere. Furthermore, equatorial (11) reflection arcs appear at around $\Phi = 25^\circ$, then splits and move off the equator with increasing Φ .

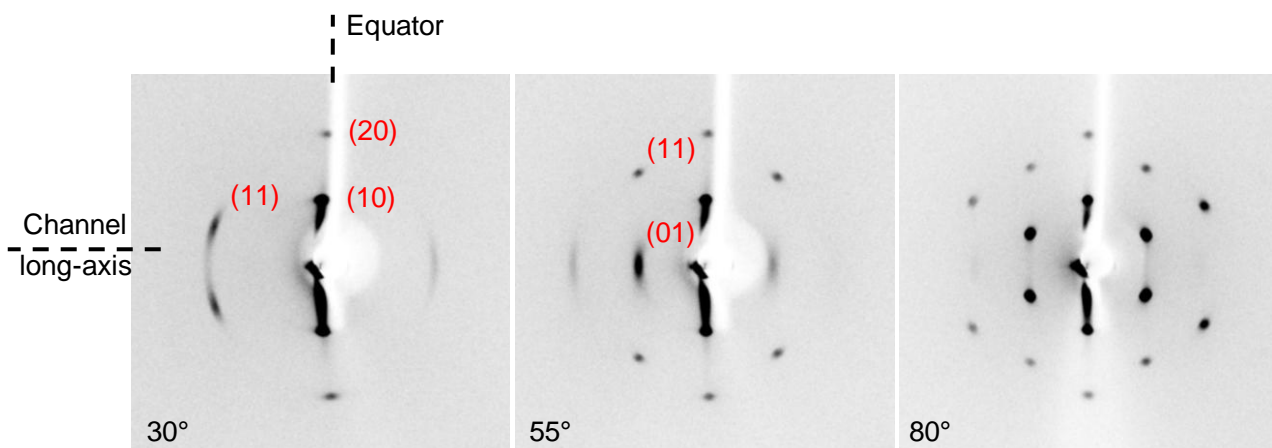


Figure 3.21 SAXS patterns of 400 nm AAO membranes filled with compounds **A3** recorded at a series of rotation angles Φ , as indicated at the corner of each pattern.

This change of the diffraction patterns reveals that the columns of the Col_{hex} phase are perpendicular to the long-axes of the nanochannels. Again, considering the planar anchoring-manner of the columns on the flat surface, we suggest the columns are in circular concentric configuration inside the nanochannels. The azimuthally narrow diffraction spots indicate that the 2-d hexagonal lattice is well oriented with its (10) plane parallel to the wall surface. This is consistent with the orientation of **A3** on the flat surface where the 2-d lattice chooses to be less distorted.

It is surprising that when A3 is filled in the 20 nm AAO template, the columns are still perpendicular to the long-axis of the nanochannel, as revealed by the SAXS pattern recorded at $\Phi=85^\circ$ (Fig.3.22). Compared with the diffraction pattern at $\Phi=80^\circ$ in Fig.3.21, the diffraction spots of the 20 nm template sample are elongated vertically. This is because the size of 2-d hexagonal lattice along the radius of the channel is now restricted to less than 20 nm and the reflection domain in the reciprocal space is elongated along the radius.

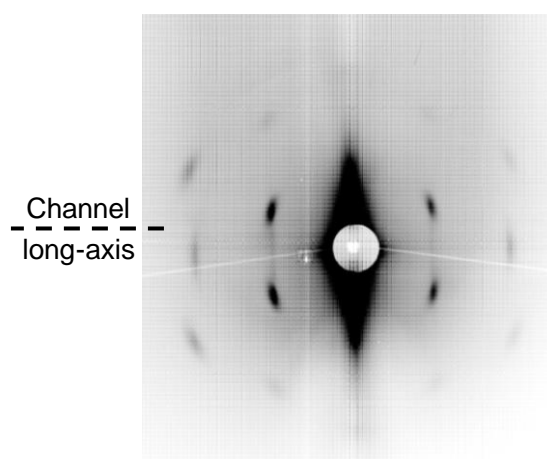


Figure 3.22 SAXS patterns of the 20 nm AAO membrane filled with compounds **A3** recorded at $\Phi=85^\circ$.

3.3 Glass capillaries

In the nanopores of AAO templates, no axial orientation was observed although it seems plausible that the planar-anchored columns should be parallel to the 1-d channel. We suggested this is because in axial orientation the polygonal cross-section of LC cylinders can't match the curved surface: the 2-d lattice would be strongly distorted and the distortion energy of the 2-d lattice (E_d) would exceed the bend deformation energy (E_b) in circular concentric orientation. When the pore size decreases, both E_d and E_b should increase. However, even in 20 nm pore we found the columns are still perpendicular to the channel. When the pore size increases, on the other hand, both E_d and E_b should decrease, thus the orientation could change depending on the relative rate of change of E_d and E_b with the curvature.

Conventionally anodization can yield ordered alumina nanopores with pitch and diameter up to 500 nm^[88,89]. In order to examine the orientation of the honeycomb columns in larger cavities, glass capillaries were employed in our study. The polarity of the inner wall surface of the glass capillaries is similar to that of alumina, thus the investigation of LCs in them can be considered as an extension of the study of AAO templates, which extends the examined cylinder sizes from tens of nanometers to hundreds of microns. Also they provide the opportunity to obtain the information of the orientation of columns from a single cylinder by X-ray diffraction, by which the configuration of the columns could be directly determined.

Besides, we used square capillaries to further change the balance between E_d and E_b : in the square capillary. The mismatch between the polygonal columns and the wall surface is largely released thus the bending energy should become dominant. As a result, axial orientation of the columns can be expected.

3.3.1 Round capillaries

Round capillary tubes with inner diameters (ID) of 0.1mm and 0.5mm were purchased from Capillary Tube Supplies Ltd, and 50 micron ID capillaries were purchased from CM Scientific Ltd. Other glass tubes with smaller sizes were obtained by stretching the 50 micron ID capillary at high temperature. LCs were melted and infiltrated into the capillaries by capillary force. All filled samples were slowly cooled (0.1 °C/min) from their isotropic temperatures into LC phases before further investigation.

Square honeycomb phase:

Compound **A1** was filled in a 6.5 micron ID capillary, which was obtained by drawing the 0.1mm ID capillary at high temperature. The diameter of the capillary was determined by optical microscope (Fig.3.23a). The orientation of the columns was first studied by POM.

When observed between two crossed polarizers, the tube filled with **A1** shows the strongest birefringence at 45° to one of the polarizers (Fig.3.23b) and the birefringence gradually becomes weak when the tube is rotated to close to parallel to one of the polarizers(Fig.3.23c). This indicates that the optic axis of the LC columns is either perpendicular or parallel to the long-axis of the capillary tube. A wedged retardation plate was used to further determine the orientation of the columns. The wedged plate was inserted at the position such that 1λ retardation was at the centre of the field with the slow axis at $+45^\circ$ to the polarizer. Thus without the sample present, a magenta color region would be seen at $+45^\circ$ to the polarizer. When a birefringent sample is observed through the microscope with the compensator in place, the color would change according to the orientation of the sample. If the slow axis of the sample and the compensator are parallel, the total birefringence is increased, and the stripe will appear second order blue. If the slow axis of the sample is orthogonal to that of the compensator, the total birefringence is decreased and the stripe will appear second order yellow. Fig.3.23.d,e shows the corresponding images with the compensator in place. From these images we can say that the orientation of the slow axis of the sample is parallel to the tube. Since the slow optical axis of the honeycomb columns is along the rod-like aromatic cores, which are perpendicular to the long-axis of the columns, we can conclude that the LC columns are perpendicular to the capillary tube.

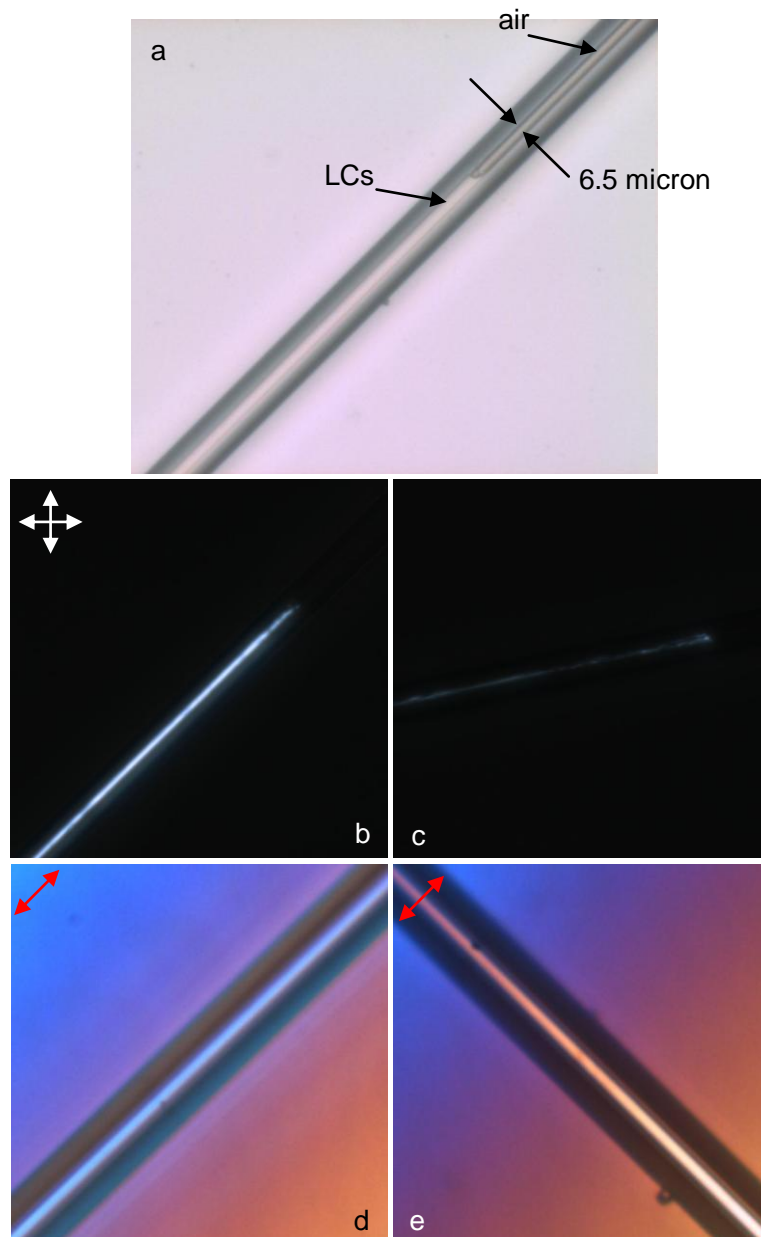


Figure 3.23 a) Optical microscope image of compound **A1** filled in a 6.5micron ID capillary without polarizer; b) the capillary is oriented 45° to the crossed polarizers; c) the capillary is oriented close to parallel to one of the polarizer. d) and e) with the compensator in place. The red line indicates the orientation of the slow axis, which is $+45^\circ$ to the polarizer.

The orientation of the columns was further studied by SAXS. The capillary was mounted horizontal and perpendicular to the incident beam. The tube could rotate about its long-axis and the rotating angle Φ was controlled by a goniometer. During the SAXS experiment, the capillary was rotated 180° about its long-axis and was exposed by every 5° . However, the diffraction pattern did not change as the capillary was rotated around its axis, as shown in Fig.3.24.a. Besides, the (10) plane of the square lattice is always parallel to the axis of the capillary tube, and the intensity of (10) on the meridian is always much higher than that of (01) on the equator.

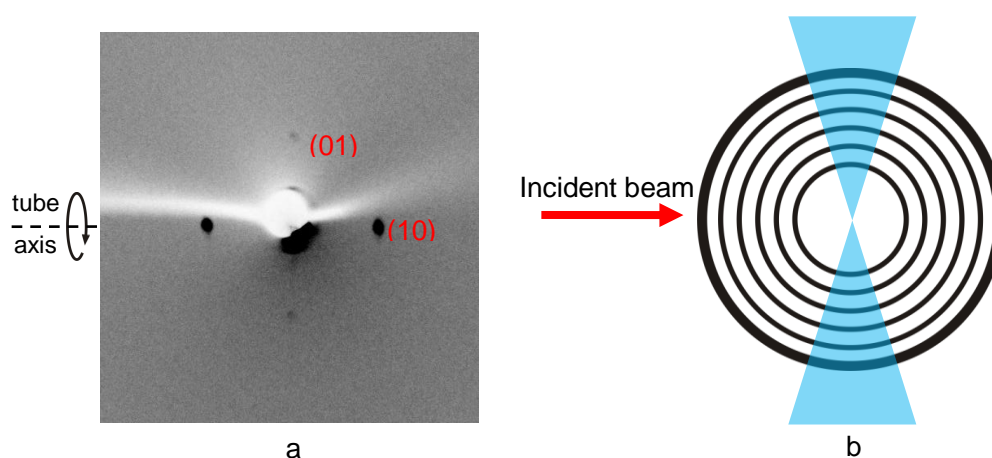


Figure 3.24 a) SAXS pattern of compound **A1** in 6.5 micron diameter capillary; b) Schematic drawing of columns inside the capillary tube: only columns in the blue areas can contribute to the (01) intensity.

These results indicate that the columns are in concentric circular configuration: in this configuration, as schematically drawn in Fig.3.24b, at any Φ angle, only columns in blue areas satisfy the condition of low-angle diffraction of a horizontally incident X-ray beam and contribute to the (01) intensity, while all the columns can contribute to the (10) intensity on the meridian, which explains the difference in the intensity of (01) and (10) spots.

When a 0.1mm inner diameter capillary was filled with compound **A1**, the diffraction pattern (Fig.3.25) showed concentric rings which can be indexed as (10), (11) and (20) according to their d-spacings. This indicates that the columns are randomly oriented. Thus

at this diameter the curvature of the cylinder circle cannot provide sufficient guidance for the columns: the deformation of the 2-d lattice and the bend deformation of the columns along the circle are both small and comparable to each other due to the small curvature and therefore the columns can grow in random directions.

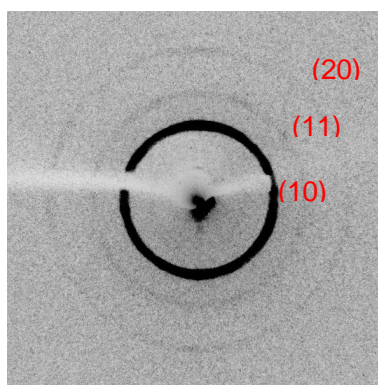


Figure 3.25 SAXS pattern of compound **A1** in 0.1mm diameter capillary.

Hexagonal honeycomb phase

For compound **A3**, the circular concentric configuration was found to be preserved in capillaries with diameters as large as 0.1mm. Fig.3.26 shows the SAXS pattern of **A3** in 50 micron, 100 micron and 0.5mm ID capillaries, respectively.

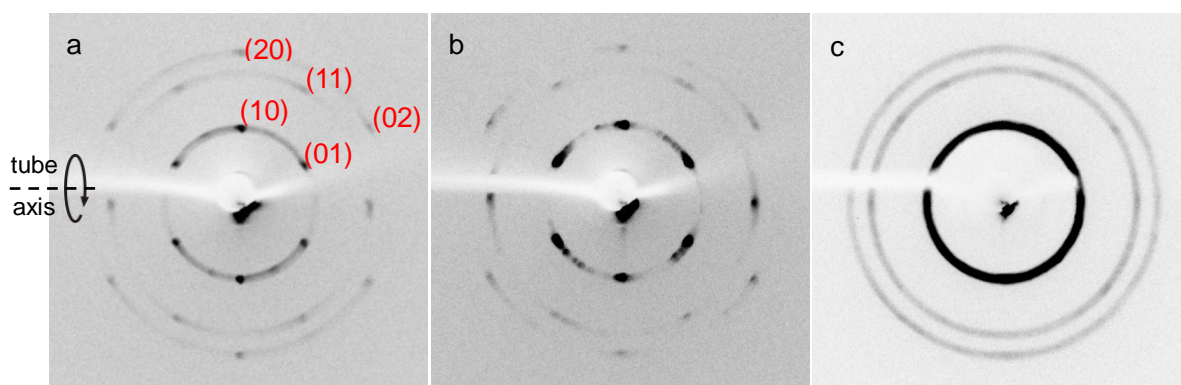


Figure 3.26 SAXS pattern of compound **A3** in round capillaries of different IDs: a) 50 micron; b) 100 micron; c) 0.5mm.

For 50 and 100 micron ID samples, the hexagonal pattern was observed at any Φ angle (Fig.3.26a,b), which suggests the circular concentric configuration of the LC columns. It is surprising how sensitive the orientation of the columns is to the tiny curvature of the wall, considering the huge difference between the radius of the column and the tube. Besides, the (10) plane of the 2-d lattice is still parallel to the long-axis of the tube. It again indicates that the orientation of the 2-d lattice is determined by how it prefers to be cut by the LC/solid interface. However, when **A3** was filled in 0.5mm capillary the orientation of the columns became isotropic, as indicated by the diffraction rings in Fig.3.26c.

3.3.2 Square capillaries

Square capillaries with 50×50 micron internal cross-section were purchased from CM Scientific. Fig.3.27 shows the reflection mode optical micrograph of the cross-section of the square capillary. The capillary was originally open at both end, and the LC sample was filled at its isotropic temperature by capillary force.

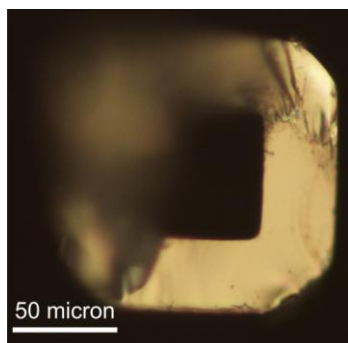


Figure 3.27 Reflection mode optical microscope image of the cross-section of the 50×50 micron ID square capillary.

The orientation of compound **A3** in the square capillary was investigated by SAXS. Fig.3.28 shows the diffraction patterns obtained at different rotation angles Φ about the long-axis of the capillary. During the rotation, at one point the diffraction pattern shows only sharp (10) spots on the equator (Fig.3.28a). Let's arbitrarily assign $\Phi=0^\circ$ at this

direction. When the tube rotates to $\Phi=1.5^\circ$, one of the (10) spots disappears first (Fig.3.28b), then the other one disappears as Φ increases. Two weak arc-like intensities flash at $\Phi=30^\circ$ (Fig.3.28c) and $\Phi=60^\circ$ (Fig.3.28d) respectively. When Φ reaches 90° (Fig.3.28e), the two strong (10) spots appear on the equator again, with another four off-equator (10) spots. Similar series of patterns at the specific Φ angles could be repeated even when the capillary was moved along the axis for about 2.5 mm.

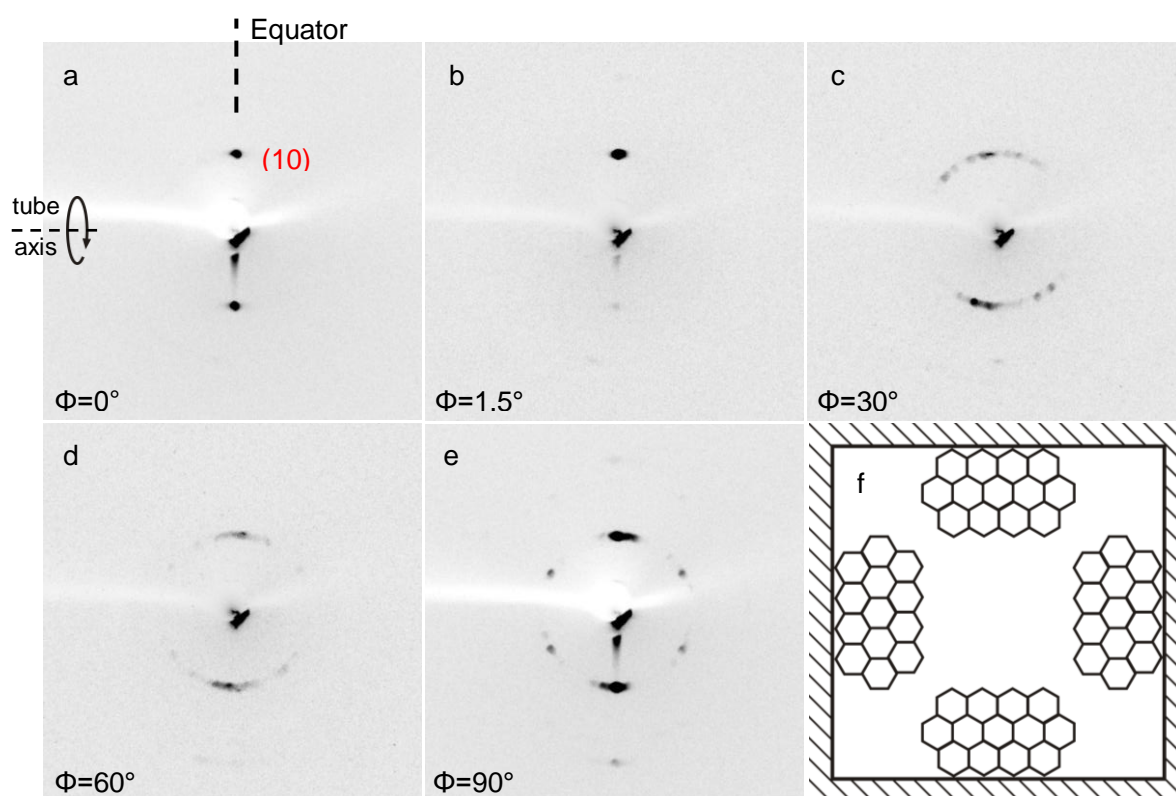


Figure 3.28 SAXS patterns of compound A3 filled in 50×50 micron ID square capillary. a) to d) are obtained at different rotation angles of the capillary about its long-axis: a) 0° ; b) 1.5° ; c) 30° ; d) 60° ; e) 90° . f) Schematic drawing of the cross section of the square capillary. Cross sections of A3 columns are symbolized by hexagons.

Considering the planar anchoring manner of A3 on the flat surface, these changes of the diffraction pattern indicate the columns are mainly oriented along the tube, and the 2-d hexagonal lattice mainly has two orientations, either of them are with the (10) plane parallel to the wall surfaces. The diffraction patterns in Fig.3.28a and e should be obtained

when the incident beam was perpendicular to the square capillary surface. However the columns are not all strictly parallel to the tube axis but can tilt away with certain distribution angles, as indicated by the arc-like (10) spots in Fig.3.28c and d. Besides there is still a small portion of columns are perpendicular to the tube axis and go across the tube from one side wall to the opposite side, as can be told from the four weaker off equator intensities in Fig.3.28e. Indeed in this organization the mismatch between the two perpendicular oriented domains of hexagonal lattice could be expected, and there should be grain boundaries at the corner of the square in Fig.3.28f. However, compared with the concentric circular configuration, the bend deformation is now largely released. Most importantly, the distortion energy of the 2-d lattice at the wall surface in the axial orientation due to the curvature of the round capillary is also released by the square profile of the tube. The square capillary filled with sample **A1** was also examined. However the orientation is quite poor.

3.4 Conclusions

In this chapter we studied the orientation of square and hexagonal honeycomb phases in cylindrical confinement where the planar-anchoring is favored at the wall surface. In 400 nm AAO template the configuration was determined to be concentric circular for all the samples examined, and two disclination lines were directly observed by AFM for compound **A1**. However in 60 and 20 nm templates, this configuration is suggested to transform to bipolar due to the increased curvature. Furthermore, the 2-d lattice was found to have preferred orientations with respect to the wall surface, in which the polygons are least deformed after being cut by the LC/solid interface.

Further, we used glass capillaries to extend the study of honeycomb phases in cylindrical confinement to micrometer scale. In 6.5 micron round capillary, circular concentric configuration of **A1** was revealed directly by SAXS experiment, and it was surprising that for compound **A3** the circular concentric configuration can be preserved in capillaries up to

100 micron ID tube. When further increasing the tube diameter the orientation of the columns became random. In a 50 micron square capillary, the columns of **A3** were revealed to be oriented along the tube. Two orientations of the hexagonal lattice coexist, due to the square profile of the tube.

Thus we suggested the orientation of the honeycomb columns inside the cylindrical confinement is determined by the competition between the distortion energy of the 2-d lattice and the bend energy E_b of the columns. When $E_d > E_b$ the columns are willing to bend and follow the tangential alignment, and when $E_d < E_b$ the columns can be axially aligned. For the round cavity, E_d and E_b both decrease as the curvature of the wall decreases. However, no axial orientation was observed for any size of circular pores examined, implying that E_d is always larger than E_b . In the square capillary, on the other hand, the distortion of the 2-d lattice on the wall surface is largely released, and the axial orientation becomes possible.

CHAPTER 4 Homeotropic-anchored Honeycomb Phase in Cylindrical Confinement

4.1 Introduction

In this chapter the orientation of hexagonal honeycomb columns in cylindrical confinement where homeotropic anchoring applies is studied. For the planar anchoring condition, as described in chapter 3, the columns choose to bend and follow the circle of the cylinders and the energy cost is mainly due to the bend of the columns. For homeotropic-anchoring, on the other hand, the situation is totally different: close to the wall surface the columns favor ordering in the radial direction, thus there would be competition between the surface and the splay energy of the columns; also there arises problem of how the polygons of the end of the columns tile the curved surface.

In the study of nematics in cylindrical confinement, it was first thought that with perpendicular boundary conditions the nematic director field would consist of only a radial component with a line disclination along the cylinder axis^[36]. Cladis and Kleman^[37] and Meyer^[38] have shown that the high cost of splay deformation energy in the center of the cylinder could be relieved by introducing a finite amount of bend deformation. This results in a continuous director field that is planar radial near the cavity wall but escapes into the third dimension along the cylinder axis. In the honeycomb phase, the polygonal shaped columns have large width and axial connectivity, therefore the splay constant K_{11} is much higher than that of the nematics. Here we studied the orientation of the honeycomb phase in the nanopores of AAO templates and glass capillaries by means of POM, x-ray diffraction and AFM.

4.2 The compound

In contrary to the planar-anchored honeycomb columns studied in the previous chapter, the homeotropic-anchored honeycomb columns consist of T-shaped bolaamphiphiles^[28] (compound **B1**). The molecular structure of compound **B1** is shown in Fig.4.1, in which the position of the amphiphilic groups is reversed to that in facial amphiphiles: the polar units (highlighted by blue ellipses) are at the termini of the aromatic core, and the alkyl chain is attached to a lateral position.

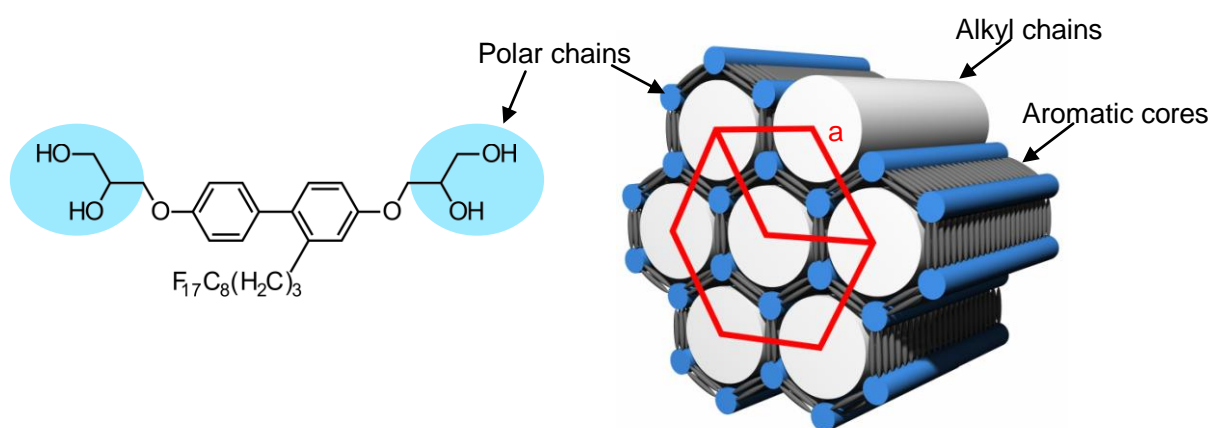


Figure 4.1 The molecular structure of compound **B1** and the schematic drawing of Col_{hex} phase. The polar units are covered by the blue shapes; Phase transition temperatures: Cr 20 °C Col_{hex} /p6mm 161 °C I; Col_{hex} phase lattice parameter: $a_{\text{sq}}=3.5\text{nm}$.

The hexagonal honeycomb phase formed by **B1** is schematically drawn on the right of Fig.4.1, in which the rigid rod-like biphenyls (grey) make up the walls, the diol terminal groups form the cell corners (blue columns), and the semiperfluorinated laterally attached alkyl chains (white columns) fill the interior of the cells. There are several distinct effects of perfluorinated chains which can influence the self-organization of such molecules. First, the perfluorinated segments are incompatible with hydrogenated molecular parts and also with polar segments. This fluorophobic effect usually increases segregation and stabilizes the mesophases. Second, perfluorinated chains occupy a significantly larger volume than alkyl chains of the same length. Finally, such chains have preferred conformations (helical) which are different from those adopted by alkyl chains.

When cooled from isotropic state (0.1C %min) to R.T, the thin film of compound **B1** sandwiched between two glass slides showed dendritic textures with a weak contrast in transmitted non-polarized light (Fig.3.18a). However, when cross-polarizers were used, the film became dark (Fig.3.18b) independent of the rotational position of the sample between the polarizer and the analyzer. This observation is characteristic of homeotropic alignment where the optic axis of the columns, which is parallel to the column axis, is perpendicular to the substrate. As a consequence, the polarized light travelling through the sample does not change and is totally stopped by the analyzer. The bright straight lines in Fig.3.18b are tumbling defects between neighboring domains. When the two glass slides were sheared with respect to each other, the whole film became bright under the cross-polarizers (Fig.4.2c), indicating the columns were tilted by the shearing force.



Figure 4.2. Optical microscope images of **B1** sandwiched between two glass slides: a) observed without polarizer; b) with cross polarizers; c) the two glass slides were sheared with respect to each other.

4.3 AAO templates

4.3.1 B1 in 400 nm AAO template

The orientation of **B1** in the 400 nm AAO template was first studied by SAXS. The membrane was filled as described in chapter 3. Before X-ray exposure, the sample was heated to 165 °C and then cooled to R.T at 0.1 °C/min. Selected diffraction patterns are shown in Fig.4.3. The strongest reflection for **B1** is the (10) reflection of the 2-d hexagonal lattice. As Φ is increased, the intensity condenses on the equator. When Φ reaches about 55°, a new set of (10) intensity maxima appears near the meridian and split and move

rapidly away with Φ increasing further. At the largest accessible Φ angle of about 80° , the positions of the six intensity maxima on the (10) ring described close to a regular hexagon. Analogous behavior is also observed for the (20) reflections, taking account of the curvature of the Ewald sphere. Furthermore, meridional (11) reflection arcs appear at around $\Phi = 25^\circ$, then split and move off the equator with increasing Φ .

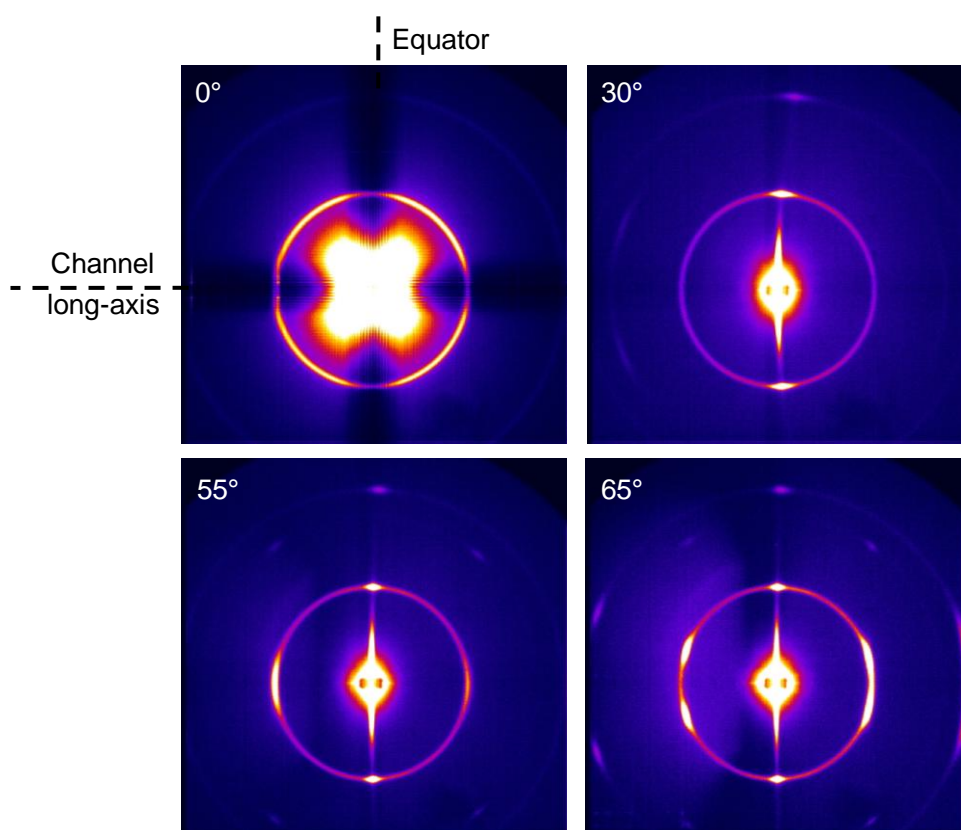


Figure 4.3 SAXS patterns of 400 nm AAO membranes filled with compounds **B1** recorded at a series of rotation angles Φ , as indicated at the corner of each pattern.

The complete reciprocal space mapping of the three strongest small angle reflection groups $\{10\}$, $\{11\}$ and $\{20\}$ for compound **B1** confined in the AAO template are shown in Fig.4.4. This map is consistent with the hexagonal 2-d reciprocal net being rotationally averaged around the axis of the nanochannel. Hence the column orientation in the nanopores again cannot be axial but either radial or tangential.

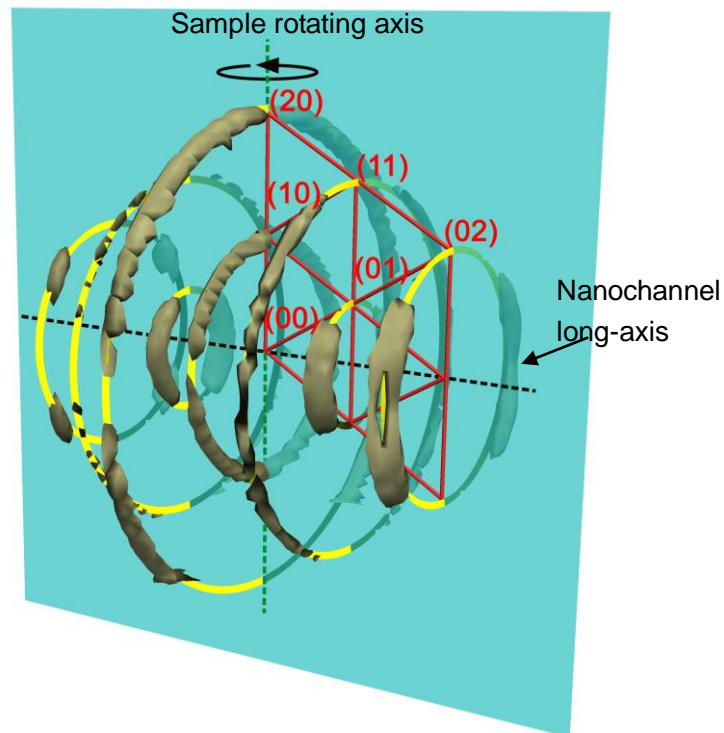


Figure 4.4 3-d diffraction patterns of **B1** confined to AAO with a pore diameter of 400 nm in reciprocal space coordinates. The dashed black line indicates the orientation of the nanopores in the AAO. The continuous background scatter predominantly originating from AAO was subtracted by means of a custom-written 3-d fitting algorithm. The breaks in the rings are mainly due to absorption of X-rays by the AAO. They are most prominent in the plane containing the nanopore axis and the axis of rotation (the blue semitransparent plane), as diffraction for $\Phi = 90^\circ$ is not accessible. The yellow lines are guides to the eyes.

Based on the SAXS results, there are two possible solutions for the homeotropically anchored columns: radial or polar configurations, as shown in Fig.4.5. In radial configuration the orientation of the columns is radial everywhere and disclination line of strength $S=1$ runs along the cylinder axis. While in polar configuration the columns cross the cylinder with splay and bend at the two ends, and two $S=1/2$ disclination lines run along the walls parallel to the cavity axis.

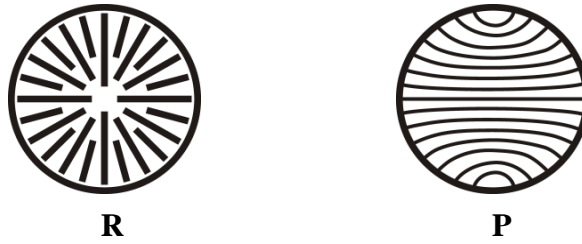


Figure 4.5 Possible order modes for homeotropic anchoring condition: radial configuration (**R**) and polar configuration (**P**).

The free energy of these two structures formed by nematics has been treated in detail^[44], which could shed some light on the system discussed here. In radial configuration, the columns mainly undergo splay deformation, and the free energy of a confined liquid crystal per unit length of the cylinder in radial configuration, which is pure splay energy, can be expressed as:

$$F_R = \pi K_{11} \ln(R/\rho) \quad (4.1)$$

where K_{11} is the elastic constant of splay deformation, R is the radius to the outer surface of the LC, and ρ is the radius of the line disclination at which the elastic theory breaks down. This configuration is independent of anchoring strength since the director is perpendicular to the wall surface.

The polar configuration, on the other hand, involves both splay and bend deformations. Under strong homeotropic anchoring condition, it has been calculated for nematics that if we assume that $K_{11}=K_{33}$ (elastic constant of bend deformation), the free energy per unit length of the cylinder can be determined as:

$$F_R = \pi K \ln(R/2\rho) \quad (4.2)$$

For the above mentioned approximation, the free energy of polar structure should be always lower than that of radial structure.

Whether the alignment is radial or polar can also be deduced from the broadening of the diffraction peaks. In practice, the X-ray reflection peaks would be broadened by

instrumental factors such as the finite breadth and divergence of the X-ray beam, as well as the finite size of the crystal^[90]. After instrumental broadening had been deconvoluted, the measurement of such broadening in the vertical direction can then provide additional information on the size of the coherently diffracting domain in the direction perpendicular to the long-axis of the nanochannel.

Based on the Scherrer equation^[90] the correlation lengths L of the 2-d lattice of the columnar LC phases in 400 nm AAO template was calculated (the detailed calculation is described in A.1) and the results are listed in Tab.4.1.

Radial			Axial		
$d_{(10)}$	Δq_r	L_r	$d_{(01)}$	Δq_z	L_a
3.17	0.0038	165	3.14	0.0016	400

Table 4.1 Interplanar spacings d , corrected line broadening Δq , and coherence lengths L_r in the radial and L_a axial directions for compound **B1** in 400 nm AAO template ($\Phi=80^\circ$). All values are in nm.

It can be seen that the correlation length in the radial direction is less than half that in the direction of the pore axis. One can argue that the L value of 165 nm in 400 nm pores is rather high and is inconsistent with the model of radial column orientation (Fig.4.6a). Here the main diffraction comes from those only few columns (blue shadowed area) close to the horizon satisfy the condition of low-angle diffraction of a horizontally incident X-ray beam. However, the experimental L value is fully compatible with the polar configuration model in Fig.4.6b. Here the columns are straight and well ordered in most of the pore volume, with curvature and splay confined only to the surface layer closest to the pore wall. In this model, the main diffraction comes only from those relatively few pores whose column in the central bulk volume are in the correct orientation, i.e. nearly parallel to the X-ray beam. Other 400 nm pores may contribute only a minor part to the diffraction with their small favourably oriented surface domains of bent columns.

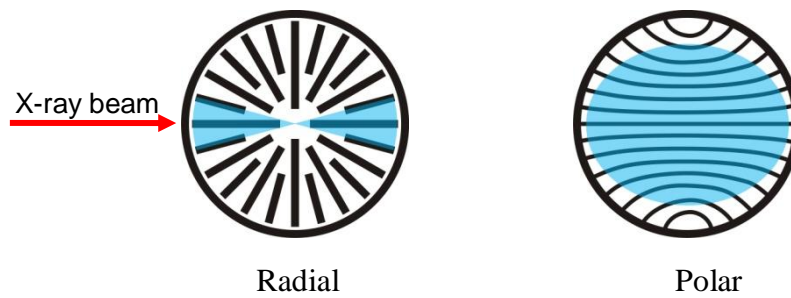


Figure 4.6 a) radial configuration (**R**); b) polar configuration (**P**). Blue areas in the images satisfy the condition of low-angle diffraction of a horizontally incident X-ray beam.

Tapping mode AFM imaging was performed on the fracture surface of the 400 nm AAO template filled with **B1** to further verify the orientation of the columns inside the nanochannels. The sample was prepared following the same procedure as described in chapter 3. Fig. 4.7a. shows the phase image of one channel cut open by the fracture surface, in which most of the material remains. The width of the groove is about 145 nm, which means the 400 nm diameter cylinder was cut off-center. Bundles that are perpendicular to the vertical wall of the groove can be clearly seen, and they are broken off at different lengths. The width of these bundles is varying, and the smallest distinguishable size is about 10 nanometers. Although it is difficult to identify individual LC columns from these bundles since the surface is not smooth, we infer that they are bunches of LC columns that are aligned crossing the cylinder. This morphology implies that the LC columns are in polar configuration.

In another groove, however, the LC forms terrace-like structure grown parallel to the channel (Fig. 4.7b). The corresponding height image data of Fig. 4.7b was analyzed by Nanoscope software. Section analysis was performed on a small area of the terrace containing one step to assess the thickness of the layer structure, as shown in the lower left of Fig. 4.7b. After being flattened, the thickness of the layer was estimated to be about 3.5 nm, which matches well the thickness of one column of the Col_{hex} phase. Further, the high-resolution phase image resolved vertically oriented LC columns on the surface of the layer (Fig. 4.7c) with width of about 3.5 nm. The inserted image on the upper right of Figure 10c is a two-dimensional fast Fourier transform filtered image.

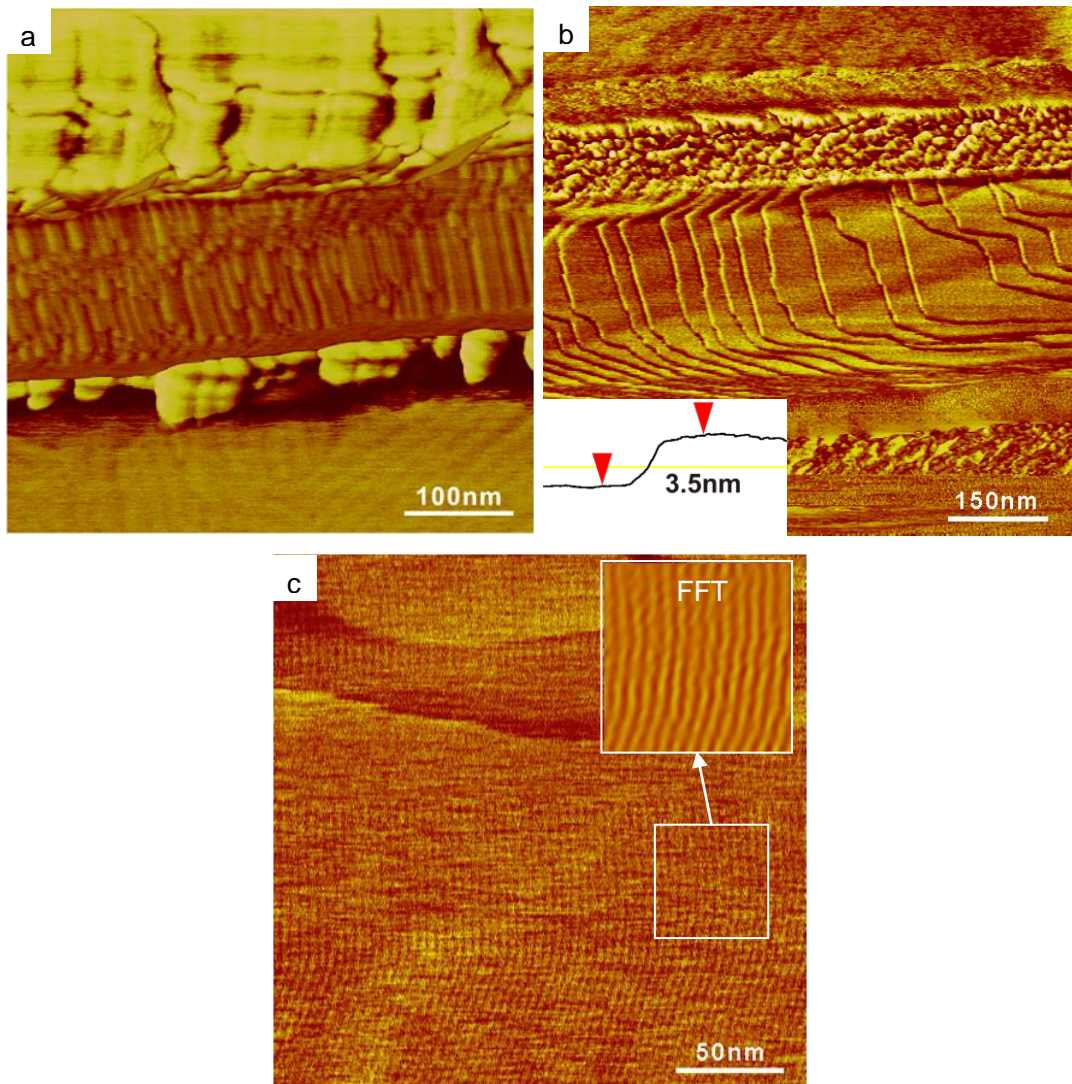


Figure 4.7 AFM phase images obtained on the fracture surface of the 400 nm AAO template filled with **B1**: a) bundles of columns observed in a groove with width of 145nm; b) terrace-like structure in another groove. The lower left is the section scan across the step to measure the step height. c) high resolution phase image of a layer in b).showing individual columns.

The formation of terrace-like structure in Fig.4.7b again confirms that the honeycomb columns inside the nanopore are in polar radial configuration with one of the (10) plane of the hexagonal lattice parallel to the channel axis. This could be illustrated by the model presented in Fig.4.7d,e.

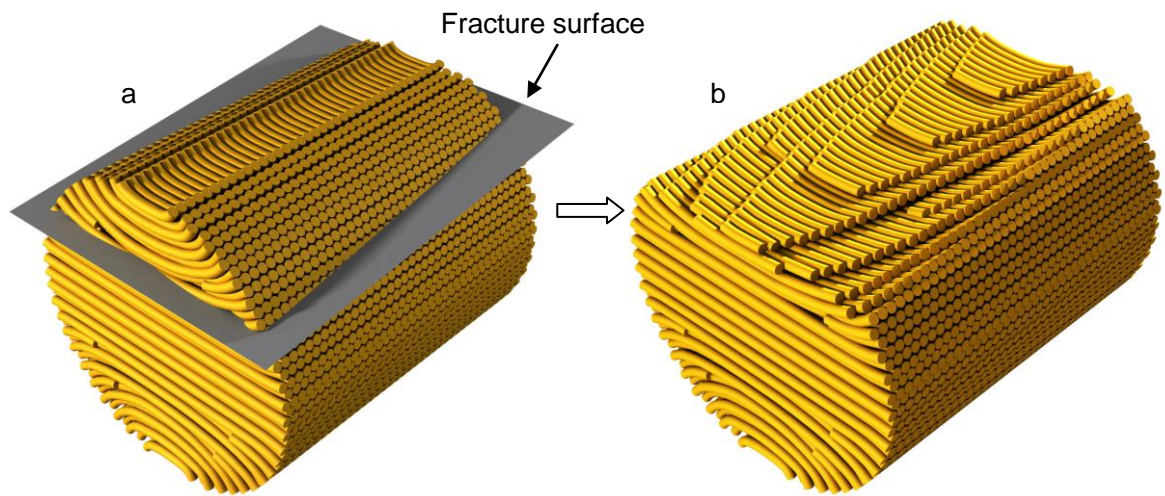


Figure 4.8 a) Schematic drawing of the hexagonal columnar LC in polar configuration in the 400 nm pore being tilted cut by a plane; b) the volume above the cutting plane is removed and the columns are peeled off.

When the fracture surface of the AAO membrane is accidentally cut through the honeycomb slightly tilted to the (10) plane (Fig.4.8a), the columns could be smoothly peeled off layer by layer along the (10) planes forming terrace-like structure (Fig.4.8b). At the same time, in Fig.4.7a the bundles are formed when the fracture surface is not parallel to the (10) plane and cuts through the columns. Thus, by combining the SAXS and AFM experimental results it can be concluded that the columns of **B1** in Col_{hex} are in polar configuration in the 400 diameter pores of the AAO template.

4.3.2 B1 in 60 and 20 nm AAO template

The configurations of **B1** in pores with 60 and 20 nm were further explored by SAXS. The samples showed similar diffraction patterns as that of the 400 nm template sample at a series of Φ angles, which indicates the columns are still perpendicular to the nanochannels. Fig.4.9 shows their SAXS patterns at $\Phi=85^\circ$.

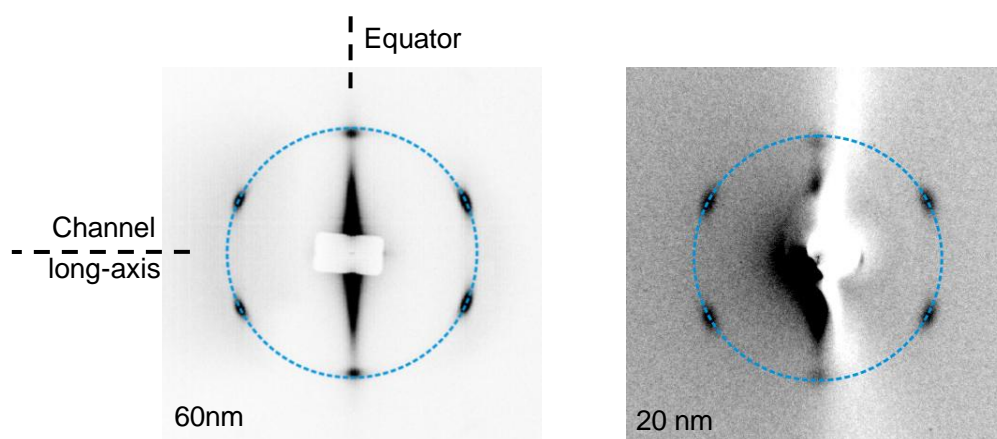


Figure 4.9 SAXS patterns of compound **B1** filled in 60 and 20 nm AAO templates recorded at $\Phi=80^\circ$, respectively. The blue dashed circles are just guide to compare the d-spacing of (10) and (01) spots.

However, it can be seen that the (10) reflections on the equator are clearly centered at a smaller diffraction angle than the other equivalent reflections, which indicates the $d_{(10)}$ spacing along the radial direction is larger than that of the other directions. This breaking of hexagonal symmetry is consistent with the polar configuration model since in the small pores most of the diffraction comes from the splayed peripheral domains. The correlation lengths L along the radial of the 60 nm template was calculated as 39 nm, which is rather high compared to the size of the pore. This again agrees with the polar configuration.

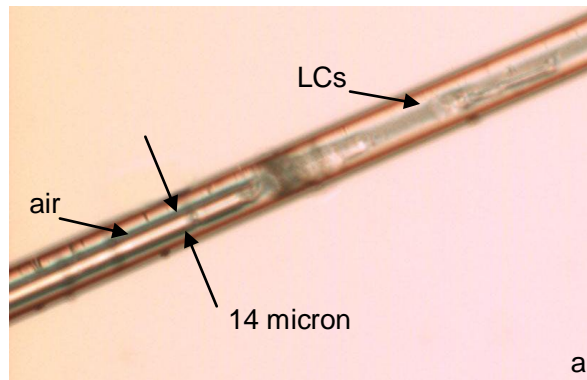
4.4 Glass capillaries

We have observed that the homeotropically anchored honeycomb columns mainly exhibit polar configuration in AAO templates with pore diameters up to 400 nm. In this section, round glass capillaries were used to explore the configuration of **B1** in micrometer-sized cylindrical confinement. Three sizes of capillaries were used: 14, 50 and 100 micron inner diameters (ID). In the round cylinder the anchoring force points to the center anywhere throughout the cross-section. In this section we also used rectangular capillaries to direct the anchoring force in specific directions.

4.4.1 Round capillaries

14 micron ID round capillary

A 14 micron ID capillary obtained by stretching the 100 micron ID capillary at high temperature was filled with compound **B1**. The diameter was determined by optical microscope (Fig.4.10a). The orientation of the columns over the whole tube was first studied by POM. When observed between cross polarizers, the tube filled with **B1** shows the strongest birefringence at 45° to one of the polarizers (Fig.4.10b) and it gradually becomes dark when it orients close to parallel to one of them (Fig.4.10d). This indicates that the optical axes of the LC columns are either perpendicular or parallel to the long-axis of the capillary tube. Fig.4.10e,f shows the corresponding images with the compensator in place. The slow axis of the compensator is indicated by the red double-arrow. The capillary is yellow/blue when it is perpendicular/parallel to the slow axis of the compensator, respectively. Since the slow axis is perpendicular to the columns, it can be concluded, as in Chapter 3, that the LC columns are perpendicular to the capillary tube.



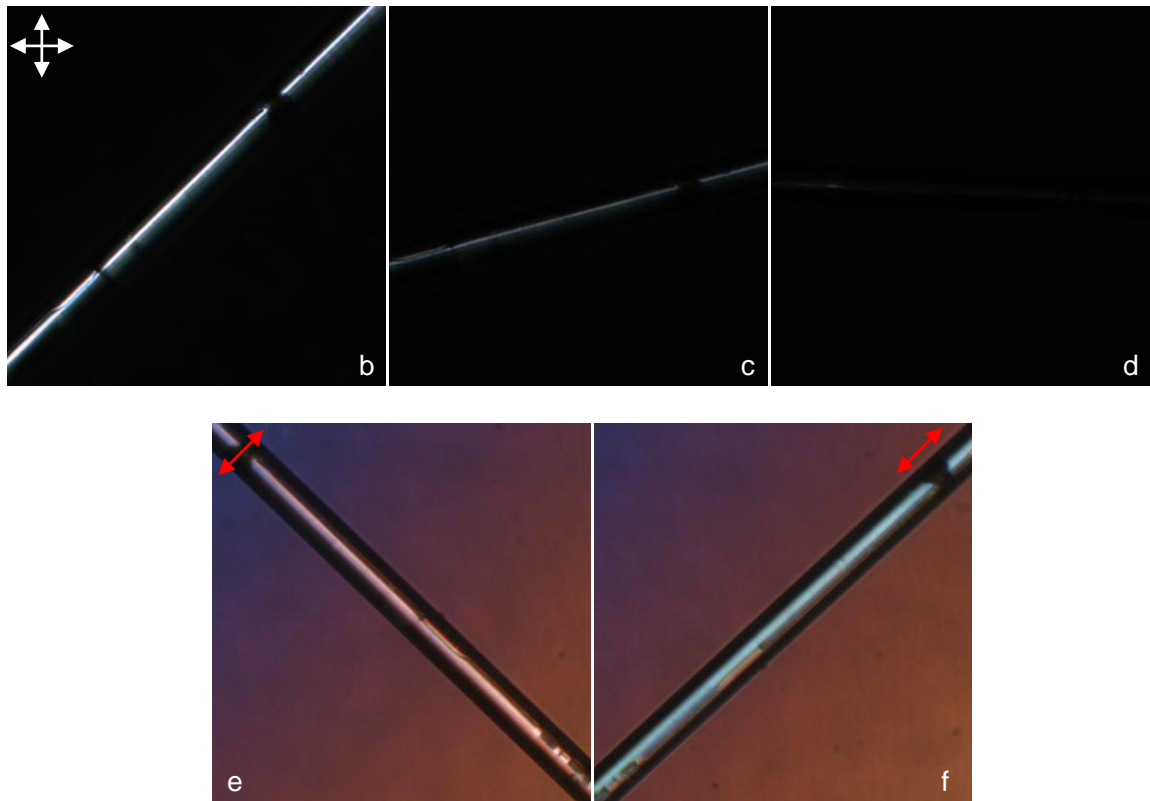


Figure 4.10 a) Optical microscope image of compound **B1** filled in a 6.5 micron ID capillary without polarizer; b-d) the capillary is oriented 45° , 15° and 0° to the horizontal polarizer, respectively; e) and f) with the compensator in place. The red double-arrow indicates the orientation of the slow axis of the compensator.

The orientation of the columns was further studied by SAXS. The capillary was mounted horizontally and perpendicular to the incident beam. During the SAXS experiment, the capillary tube was rotated around its long-axis and the diffraction patterns were recorded at different α angles. $\alpha=0^\circ$ is arbitrarily assigned to the angle at which the hexagonal pattern appears, as shown in Fig.4.11a. The sharp diffraction spots indicate the orientation of the hexagonal lattice is quite uniform. As α increasing the four off-meridian (10) intensity maximum first became weak and then disappeared (Fig.4.11b,c). When α reached 60° , the two intensity maxima close to the meridian started to fade away. These observed changes indicate that at $\alpha=0^\circ$ the reciprocal 2-d hexagonal lattice is lying on the Ewald sphere, then it rotates about the meridian and the lattice points gradually move away from the Ewald sphere. Thus, the columns are in polar configuration in which they cross the cylinder from one side to the other with expected bend and splay at the end of the columns.

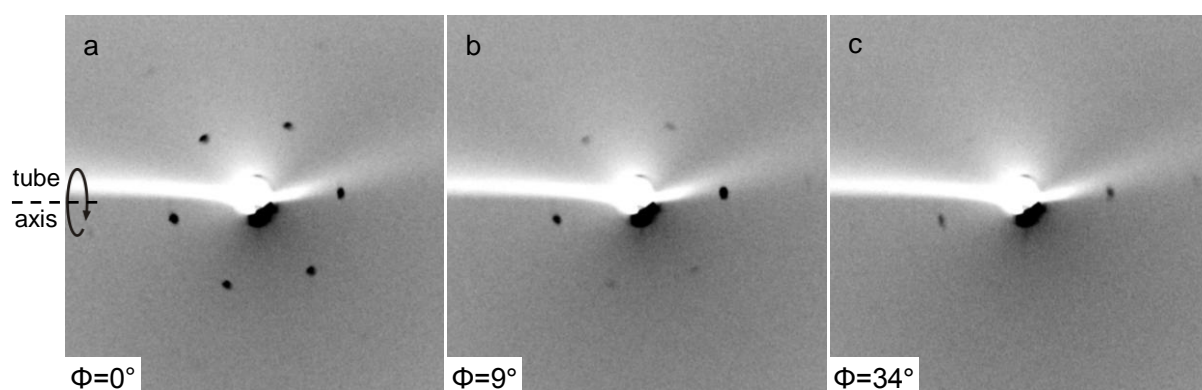


Figure 4.11 SAXS pattern of compound **B1** in a 14 micron ID capillary recorded at different rotation angle α as indicated at the corner of each images.

It remains for us to comment on the in-plane orientation of the hexagonal lattice. In the nanopores up to 400 nm the (10) plane is always parallel to the nanopore axis, however, in the micrometer tube it is close to perpendicular to the tube axis, i.e. the hexagonal lattice has turned in-plane by 30° . In chapter 3, the 2-d lattice in the circular-concentric configuration is perpendicular to the wall surface and we suggested that it orients in a way that the lattice is the most intact at the LC/solid interface. For polar configuration, on the other hand, the 2-d lattice is parallel to the surface and the situation is quite different. On a flat substrate a homeotropically oriented columnar LC has no preferred in-plane orientation, yet here, even with only mild curvature the hexagonal lattice is perfectly oriented as can be seen from the sharp reflections.

We suspect that in the nanopores the size of the hexagon is close to the curvature and the orientation of the 2-d hexagonal lattice could be affected by how the hexagonal lattice tiles the curved surface. Indeed, Irvine and coworkers^[91] have studied the tiling of hexagonal lattice of positively charged PMMA particles on the curved oil-glycerol interfaces. They showed that on the barrel surface, the hexagonal lattice orients with one of its (100) planes parallel to the axis of the barrel (Fig.4.12). This result coincides with the orientation of the 2-d hexagonal lattice of **B1** in nanopores.

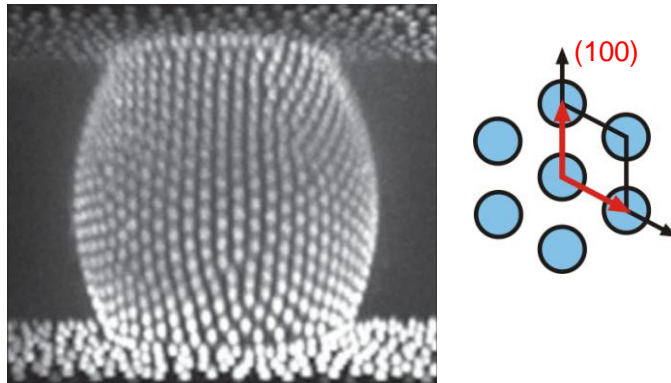


Figure 4. 12 Fluorescent PMMA particles bound to oil-glycerol interface in the shape of barrel (from ref[91]).

In the capillary tube, however, the radius of the curvature is far larger than the diameter of hexagon that it becomes less selective on the orientation of the hexagonal lattice. On the other hand, the columns start growing spontaneously toward the radial direction on the wall surface upon cooling (Fig.4.13a). When they grow further there is no enough space in the plane of the cross section for the ends to develop and defects must be introduced to solve the spacial problem. In this case the transverse edge dislocation is the most possible solution, as drawn on the periphery of the circle in Fig.4.13a. When the hexagonal lattice orients with the (10) plane perpendicular to the channel axis only one defect line is required in order to keep the symmetry (Fig.4.13b). Otherwise there must be two defect lines or screw dislocation and thus higher energy (Fig.4.13c,d).

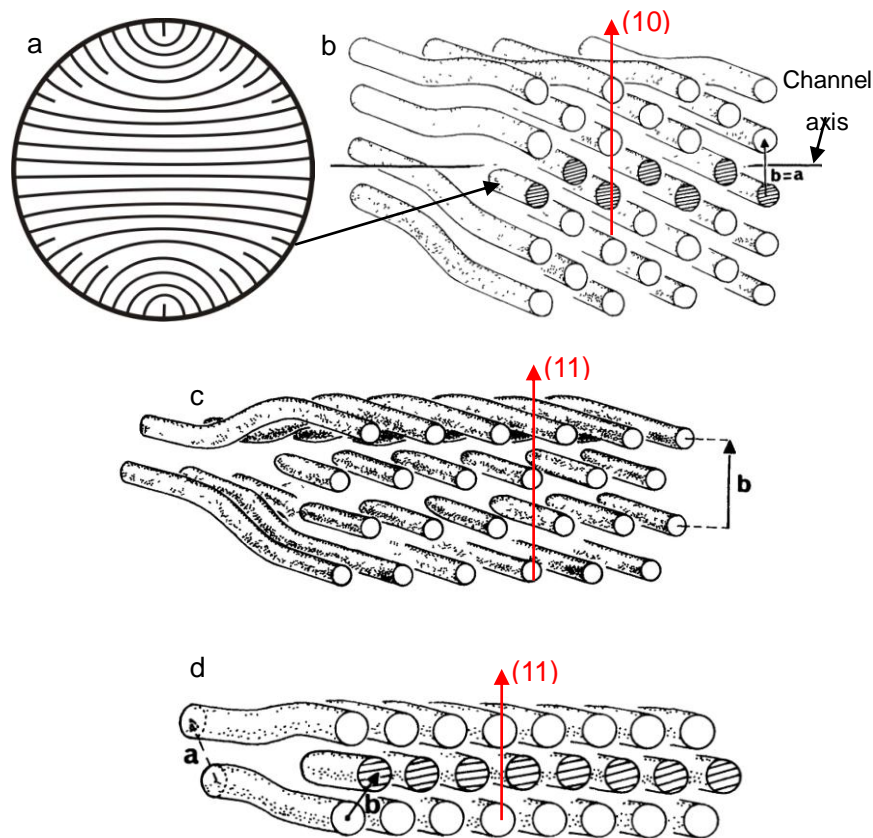


Figure 4.13 a) Schematic drawing of the polar configuration with dislocations; b-c) transverse edge dislocation with the defect line along different planes; d) a combination of transverse edge dislocation and screw dislocation.

Surprisingly, as the capillary moves along the long-axis at a fixed α angle, the diffraction pattern keeps almost unchanged over a long distance. For example, at $\alpha=0^\circ$ the six spots appears at the same position as the capillary moves horizontally. It reveals that the curvature induced orientational order of the columns propagates along the capillary. This can also be directly observed from the birefringence of the sample. In Fig.4.14 the left side shows the optical images of the sample without polarizer while the right side shows the corresponding birefringence textures obtained with crossed polarizers. The red ovals are used as reference area to make sure that the same segment of the tube is in the view. As the capillary was rotated about its axis, the birefringence changed uniformly along the tube. This indicates that the columns orient in the same direction over hundreds of microns. This result implies that the columns of the honeycomb are strongly interconnected and the twist deformation energy is quite high.

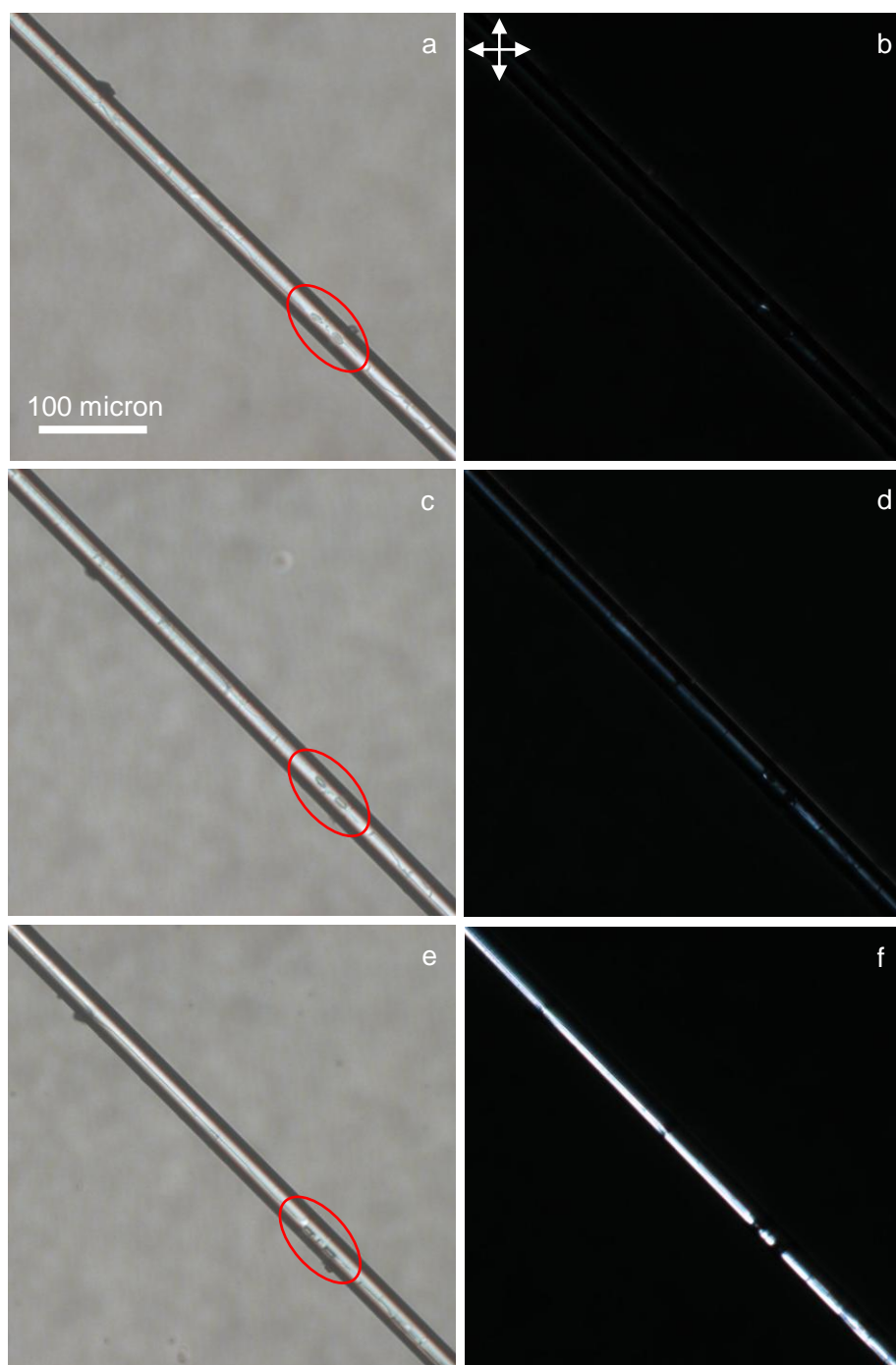


Figure 4.14 Optical microscope images of the 14 micron ID capillary filled with **B1** at different rotation angles about the tube axis, with (right side) and without (left side) cross polarizers. The red ovals are used as a reference area to make sure the same segment of the tube is in the view.

50 micron ID round capillaries

When compound **B1** was introduced into a 50 micron ID capillary, the SAXS pattern shows that no matter how the capillary rotates about or moves along the tube axis, the intensity maxima are always concentrated on the equator (Fig.4.15). It indicates the reciprocal 2-d lattice points are distributed on concentric rings perpendicular to the axis of the tube. Thus the honeycomb columns are parallel to the capillary axis.

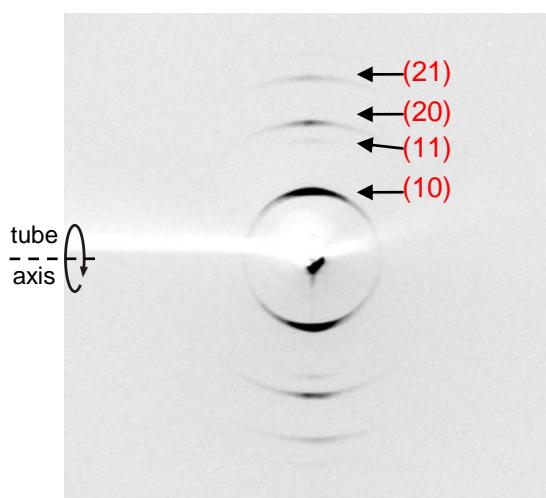


Figure 4.15 SAXS pattern of compound **B1** filled in a 50 micron ID capillary.

Earlier theoretical studies focusing on nematics phase in cylindrical confinement have shown that when the radius of the cylinder was sufficiently large, the total energy could be reduced by allowing the molecules to relax out of the plane, i.e., to release the splay energy by including a finite amount of bend deformation and form so called escaped radial configuration. For honeycomb phase confined in the large capillary, the columns should be still radially oriented close to the wall surface due to the homeotropic anchoring; while close to the center the splay deformation increases rapidly as the columns are forced to bend to the axial direction in order to release some of the splay energy. Thus we speculate the honeycomb columns are in escaped radial configuration, but with a thin sheath of non-axial splayed configuration close to the glass surface. A similar configuration was observed for **B1** in the 100 micron capillary.

4.4.2 Rectangular capillary

20×200 micron ID rectangular capillary

Rectangular capillaries with 20×200 micron ID were purchased from CM Scientific. The reflection mode optical microscopy images of the cross-section of the rectangular capillary are shown in Fig.4.16, in which it can be seen that the corner of the rectangle is relatively sharp, and the two sets of walls are perpendicular to each other. Since the LC columns prefer homeotropic anchoring on the LC/solid interface, the two sets of wall surfaces would deliver conflicting orientation instruction to the columns. Therefore, the system may either attain a randomized equilibrium state, with orientational constraints being respected at the local scale but with no long-range order, or displaying a long-range preferred alignment, only following one set of orientational instructions. The selection between these two possibilities depends on many parameters, among which are the elastic properties of the columns, the energy cost of grain boundaries, and the difference between the dimensions of the opposite walls.

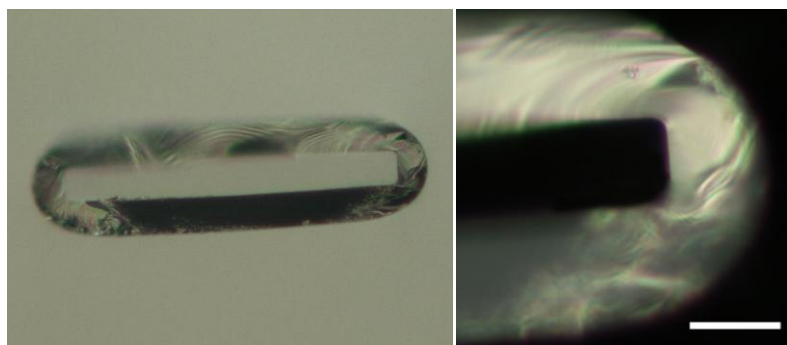


Figure 4.16 Reflection mode optical microscope images of the cross-section of the 20×200 micron ID rectangular capillary. The bar represents 20 micron.

The capillary was originally open at both end, and **B1** was melted and admitted to the capillary. Then the sample was cooled to R.T at a rate of 0.1 °C/min. The overall orientation of the LC columns was first studied by POM. When observed between cross polarizers with the wide side of the tube face-on, most part of the filled tube is totally dark (Fig.4.17b)

independent of the rotational position of the sample between the polarizer and the analyzer, and only close to the opening of the capillary it shows strong birefringence. This indicates that the columns inside the rectangular capillary are mainly directed by the wide sets of walls and oriented perpendicular to them. Fig.4.17c shows the end of the tube where the orientation of the columns changes due to the contact with air.

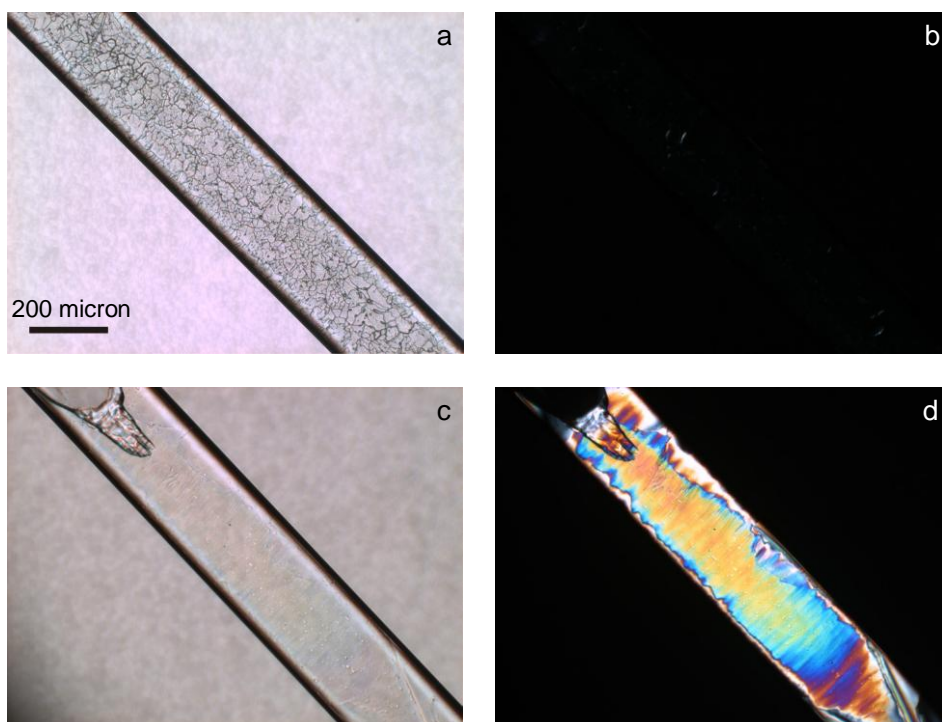


Figure 4.17 Optical microscope images of the 20×20 micron ID rectangular capillary filled with **B1**. Left side images are with cross polarizers and right side images are the corresponding images without polarizer. c) is obtained close to the end of the tube.

The orientation of the hexagonal honeycomb phase was further studied by SAXS. The capillary was mounted horizontally with the wide wall perpendicular to the incident beam. Hexagonal patterns were obtained as shown in Fig.4.18. Surprisingly, the orientation of the hexagonal lattice is quite uniform, as revealed by the azimuthally narrow diffraction spots. For example, the hexagonal lattice shown in Fig.4.18a aligned with its (10) plane close to parallel to the channel axis. This orientation keeps constant as the capillary moves along the long-axis for about 1mm, and then it tilts slightly into the orientation shown in

Fig.4.18b. Comparing these diffraction patterns with that of the round capillary sample it can be seen that the orientations of the hexagonal lattice are quite similar. In fact, the corners of the rectangular tube are not sharp but round relative to the size of the LC columns. Thus they may provide the same guidance for the orientation of the hexagonal lattice as that of the round capillary except this guidance only happens at the four corners.

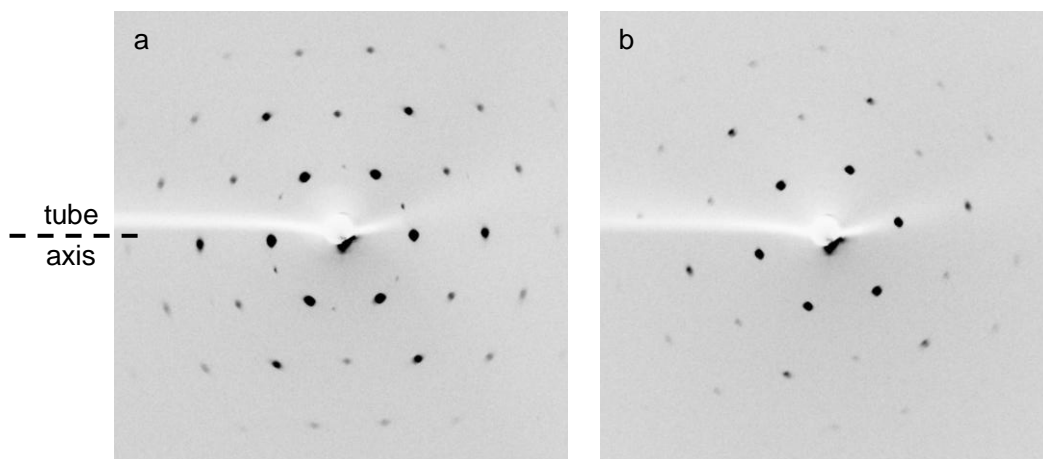


Figure 4.18 SAXS pattern of compound **B1** filled in a 0.02×0.2mm ID capillary. a) and b) were obtained at different positions along the tube.

4.5 Conclusions

To conclude, the configuration of the hexagonal honeycomb phase formed by T-shaped molecule (**B1**) in cylindrical confinement where the homeotropic-anchoring is favored at the wall surface was studied. In the 400 nm AAO template the columns were determined to be in the polar configuration by SAXS and AFM experiments. This configuration was suggested to be preserved down to 20 nm template by SAXS.

Glass capillaries were used to examine the configuration of **B1** in cavities of micrometer scale. In 14 micron ID round capillary the polar configuration was observed directly by SAXS experiments and the uniform orientation of the columns was found to propagate along the round capillary for a surprising long distance. It indicates that the correlation

between the honeycomb columns is quite strong and the twist deformation energy of the columns is high. In 50 micron ID round capillary, the columns are oriented mainly parallel to the long-axis of the tube, as revealed by the SAXS pattern. Considering the homeotropic anchoring condition, we suggest the columns are in escaped radial configuration, as that theoretically and experimentally proved in the nematics systems. Further, rectangular capillary was used to provide anchoring forces directed perpendicular to each other. It was found the columns are perpendicular to the wide wall of the tube with the hexagonal lattice oriented uniformly.

It was interesting to notice that the orientation of the hexagonal lattice changes as the pore diameter is increased: in nanopores the (10) plane is parallel to the channel axis, while in micrometer capillaries it orients with the (10) plane perpendicular to the tube. We suggested that in the small channels the orientation is determined by how the hexagonal lattice prefers to tile the curved surface, while in the large tube it is determined by the direction of the transverse edge dislocation line.

CHAPTER 5 3d Phases in Cylindrical Confinement

5.1 Introduction

In this chapter, the orientation of a more complex LC phase formed by T-shaped facial amphiphiles, the channeled-layer phase (ChL) confined in cylindrical cavities is investigated. Unlike in the honeycomb phase where the rod-like aromatic cores are perpendicular to the columns and form polygons, in the ChL phase the aromatic molecules are parallel to the columns^[92]. As a result, the rigidity of the columns in ChL phase should be much higher. Indeed, this mesophase shows very high viscosity. Thus different orientation of the ChL phase inside the cavities could be expected due to the competition between the high rigidity of the columns, the surface anchoring strength and the deformation energy of the 2-d lattice, as discussed in the previous chapters. Besides, the ChL phase resembles the smectic phase in that they both have aromatic cores and the alkyl chains segregated into distinct sublayers. The difference lies in the fact that the lateral polar group of the T-shaped facial amphiphiles in the ChL phase aggregates into ordered domains. The polar groups are quite flexible and thus they are likely to be disturbed by the confined geometry.

Two T-shaped facial amphiphiles that can form hexagonal channeled-layer phase (ChL_{hex}) are studied in this chapter. For both compounds, we showed that the ChL_{hex} phase can be suppressed in small cavities and the smectic phase becomes stable. For the ChL_{hex} phase, axial orientation of the columns was observed, which is interpreted in terms of the rigidity of the columns and flexibility of the hexagonal lattice.

5.2 Compounds

The molecular structures of the two T-shaped facial amphiphiles that can form the ChL_{hex} phase are shown in Fig.5.1. For compound **C1**, the lateral polar chain is terminated by lithium salt, and it shows only a ChL_{hex} mesophase. For **C2**, the polar chain is a bulky carbohydrate unit (1-acylamino-1-deoxy-D-sorbitol derivatives) and it shows a Col_{sque} honeycomb phase above the ChL_{hex} phase^[30]. In contrast to the columnar phase, the ChL_{hex} phase consists of alternating layers of aromatic units and aliphatic chains and exhibits positional order along the columns. As schematically shown in Fig.5.1c, the terphenyls (black rods) are positioned perpendicular to the layer planes and form periodic layers between the alkyl layers (white), while the polar domains form cylinders (blue) that arrange on a hexagonal 2D lattice and penetrate the layer structure. The phase transition temperatures and lattice parameters of the compounds are summarized in Table 5.1.

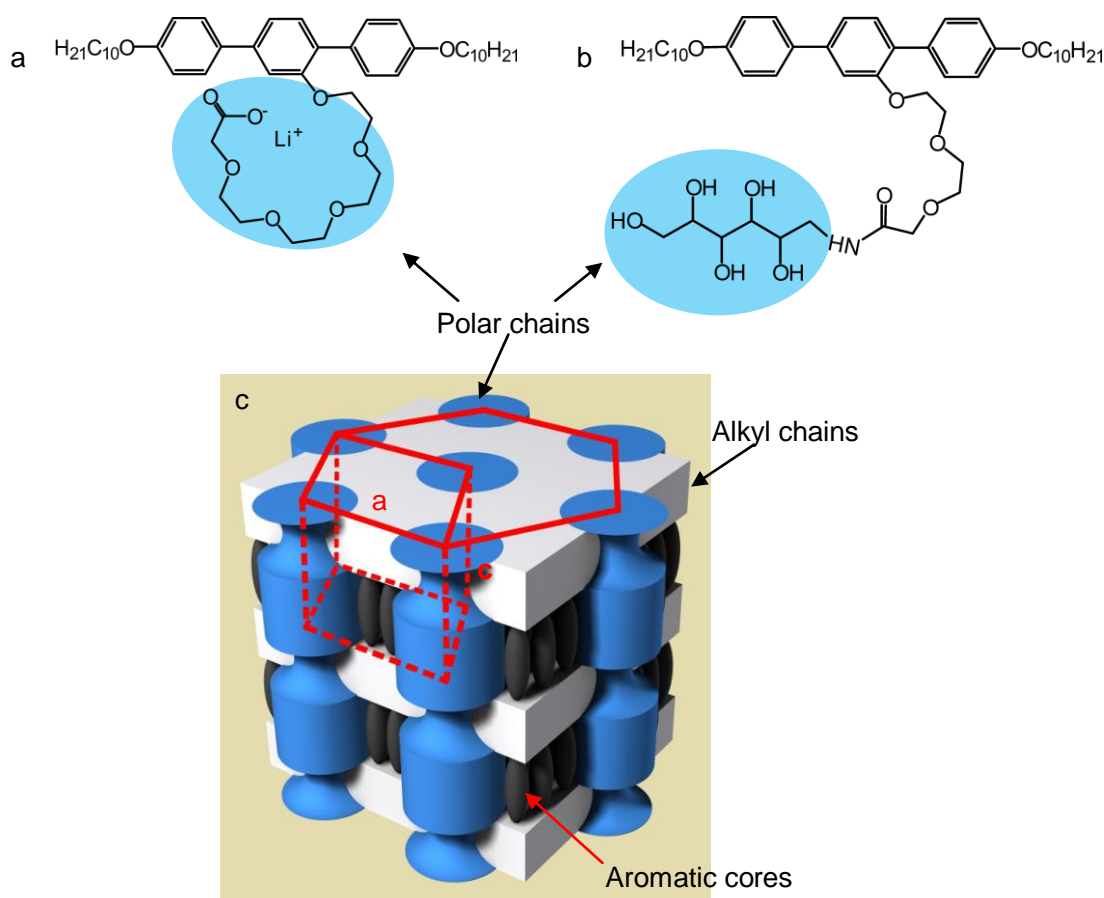


Figure 5.1 a) and b): the Molecular structures of **C1** and **C2**; c) sketch of the ChL_{hex} mesophase.

Compound	Phase transition (°C)	Lattice parameter/nm
C1	7 ChL _{hex} 99 I	$a_{\text{hex}}=3.78, c=3.65$
C2	Cr 38 ChL _{hex} 107 Col _{squ} /p4gm 143 I	$a_{\text{hex}}=4.4, c=3.8; a_{\text{squ}}=3.7$

Table 5.1 LC phase transitions and lattice parameters of compound **C1** and **C2**. Col_{squ}=square columnar phase; ChL_{hex}= hexagonal channeled-layer phase; Cr=crystal; I=isotropic liquid.

5.3 Results and discussions

5.3.1 C1

C1 in AAO templates

Compound **C1** has only one ChL_{hex} mesophase, in which the optical axis is along the columns. When sandwiched between glass slides, the texture is characterized by strong birefringent mosaics (Fig.5.2a). Rotating the mosaic texture between crossed polarizers can bring bright grains into extinction position or dark grains into bright. If annealed near the isotropic temperature, these domains can grow to a large size, as shown in Fig.5.2b.

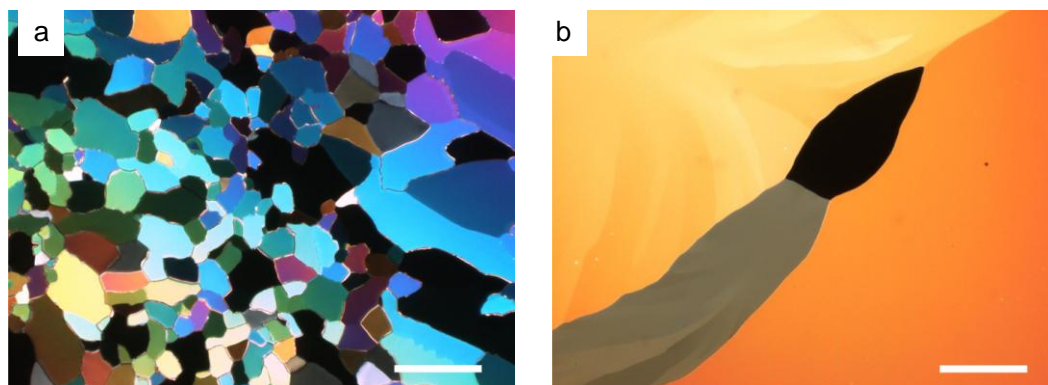


Figure 5.2 Mosaic texture of **C1** sandwiched between two glass slides, as seen between crossed polarizers. a) cooled from iso to R.T at 0.5 °C/min; b) cooled at 0.1 °C/min from iso to 98 °C and annealed. The dark area is where the optical axis (or its projection on the plane) is parallel to one of the polarizer. Bar=200micron.

The different levels of color within the mosaic areas arise from the different angles of the layers of the ChL_{hex} phase to the substrate surface, as depicted in Fig.5.3. Within areas of uniform optical appearance the director is oriented along a constant direction, which varies

from grain to grain. The mosaic texture is usually observed in Smectic B phases. In fact the structure of the channeled-layer phase is quite similar to that of the Smectic B phase: the director of the rod-like molecules is perpendicular to the layer, and in each layer there is long range orientational order of the hexagons.

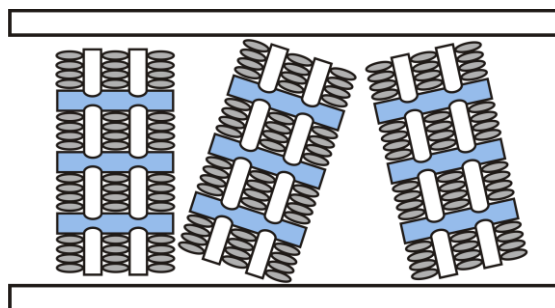


Figure 5.3 Schematic illustration of the ChL_{hex} phase configuration in the mosaic texture between two glass slides.

The orientation of **C1** in the 60 and 400 nm AAO templates were examined by SAXS. The samples were cooled from the isotropic phase to RT at 0.1 °C/min. The SAXS pattern of the 60 nm sample is shown in Fig.5.4a. The (001) intensities, which correspond to the layer structure, appear very strong on the equator but weak on the meridian. It indicates that the layers are mainly parallel to the channel axis. However the (100) reflections corresponding to the hexagonal order of the polar columns (blue columns in Fig.5.1c) are very faint and diffuse. In the ChL_{hex} phase the polar columns are the "soft" bit of the structure: the rod-like mesogens can arrange laterally in different ways and the continuous polar columns are not essential to the structure. However, the layer separation between aromatic and aliphatic chains is essential. Thus we speculate that in such small pores the compound behaves like a smectic: the layers are wound up homeotropically concentric inside the curved wall, and the system gives up on the hexagonal column packing.

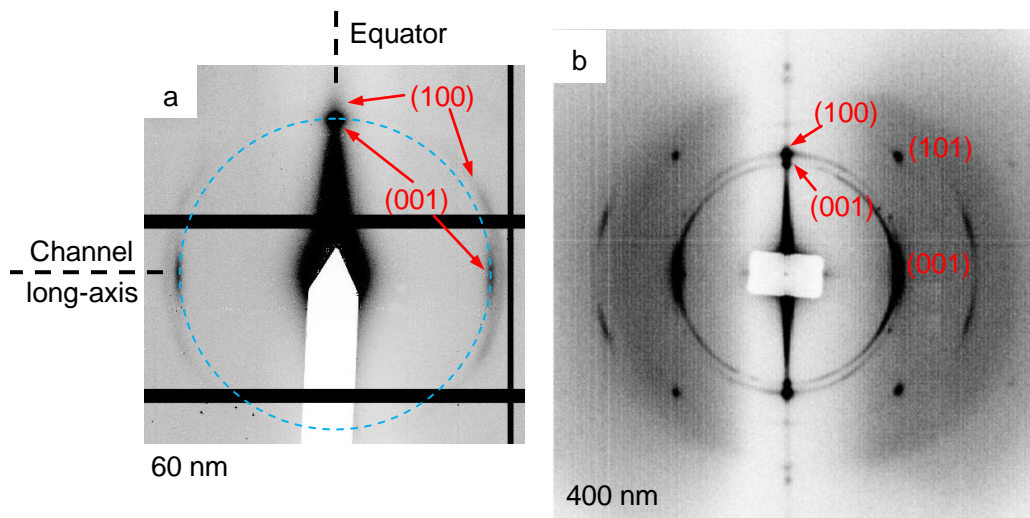


Figure 5.4 SAXS pattern of C1 filled in AAO templates: a) 60 nm; b) 400 nm. $\Phi=80^\circ$

For the 400 nm sample strong (100) intensities appear on the equator, while the (001) intensities are strong on the meridian (Fig.5.4b). This indicates that the columns of the ChL_{hex} are parallel to the long-axis of the nanochannel (axial configuration). In chapter 3 we revealed that the planarly anchored honeycomb columns prefer to bend and follow the circumference of the cylindrical cavities, which we explained as due to the distortion energy of the hexagonal lattice exceeds the bend energy of the columns. In the ChL_{hex} phase, however, the hexagonal lattice does not have to be particularly distorted in the axial configuration because there are no laterally lying rigid rods having to be squashed in such a deformation. On the other hand, the aromatic rods are parallel to the polar columns, which would increase the bend constant along the column direction.

Besides, there is still a small fraction of layers parallel to the channel axis, as can be seen by the relatively weak (001) reflections on the equator. However, these layers do not show obvious hexagonal reflection. Thus we suggest that this small portion of material behave like a smectic similar to that observed in the 60 nm template. Compared to the 60 nm pores, the curvature now is not so severe here and most columns can orient axially and pack on a hexagonal lattice.

C1 in a round glass capillary

By introducing **C1** into glass capillaries with a diameter of the order of a micrometer, we further investigated the effect of increasing the size of the cylinder on the orientation of the ChL_{hex} phase. Compound **C1** was first loaded into an 8 micron ID capillary, obtained by drawing the 50 micron ID capillary at high temperature. The diameter of the capillary was determined by optical microscope (Fig.5.5a). When observed between two crossed polarizers, the tube filled with **C1** shows strong birefringence when it is parallel to one of the polarizer (Fig.5.5b,e). When the tube is rotated away from the direction of the polarizer, the birefringence gradually fades away (Fig.5.5c-d). This indicates that the optic axes of the LC are tilted away from the long-axis of the capillary tube.

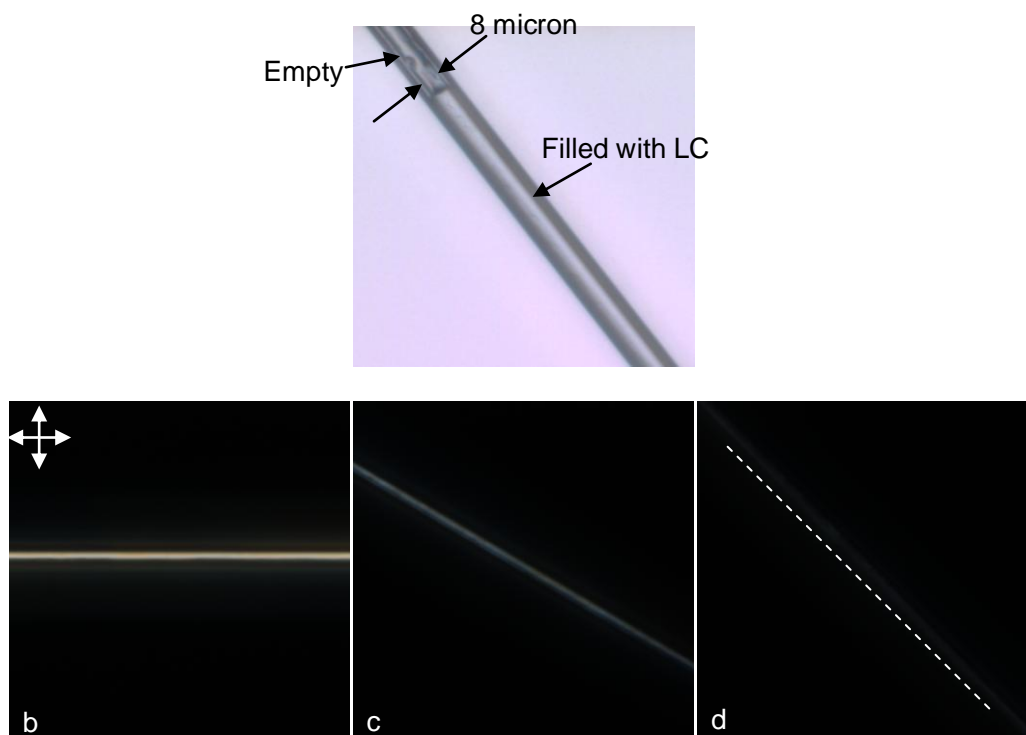


Figure 5.5 a) Optical microscope image of compound **C1** filled in an 8 micron ID capillary without polarizer; b) the capillary is oriented parallel to one of the polarizer; c) the capillary is rotated away from the horizon; d) 45 ° to the crossed polarizers. The dashed white line in d) indicates the orientation of the tube.

SAXS experiment was performed to further confirm the tilted orientation of the 3-d columns. The capillary was mounted horizontally and perpendicular to the incident beam. As the glass tube was rotated about its long axis, sharp pairs of spots sequentially showed up and then disappeared as shown in Fig.5.6(a-d). The rotation angle α is indicated at the

corner of each image (0° is assigned to the angle at which the first pair of (100) spots shown up). These reflections can be indexed as (100), (010), (110) and (001) according to their d-spacings. Thus the orientation of the LC columns can be determined as tilted 70° to the long-axis of the glass tube, as indicated by the red dashed line in Fig.5.6d. In this case the channeled-layer phase forms a monodomain in the tube and behaves more like a crystal.

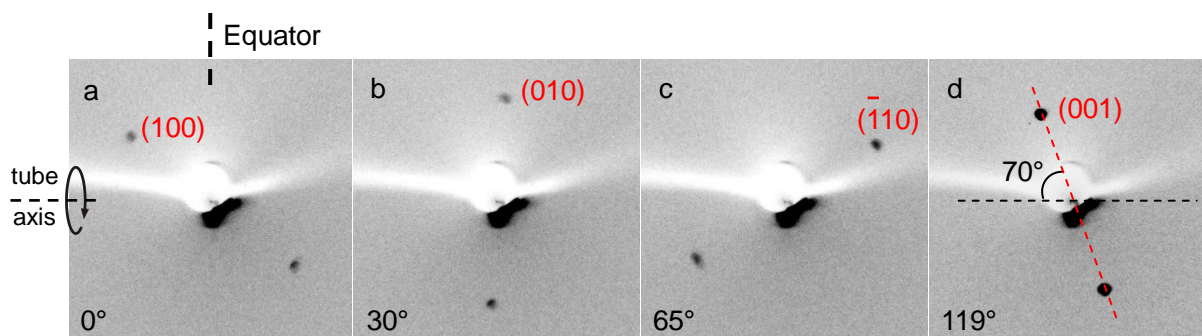


Figure 5.6 SAXS patterns of compound **C1** filled in 8 micron ID round capillary obtained at different rotation angle α about its long-axis, as indicated at the corner of each image. 0° is assigned to the angle at which the first pair of (100) spots appeared. The red dashed line in d) indicates the orientation of the LC columns.

Similar tilted orientation of the 3-d columns was observed in a 2 micron ID capillary (Fig.5.7a) except that the tilting angle is smaller: the (001) reflections shown in Fig.5.7b indicate that the LC columns are tilted about 40° to the long-axis of the capillary. Thus it can be seen that the tilting angle of the columns from the channel axis increases as the curvature decreases.

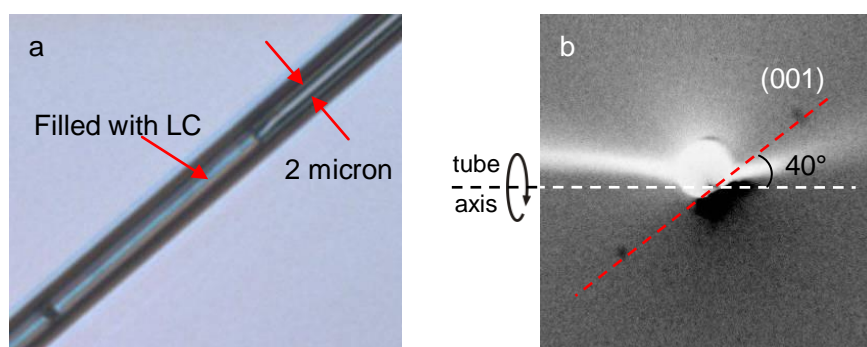


Figure 5.7 (a) Optical microscope image of compound **C1** in a 2 micron ID capillary; (b) SAXS patterns of compound **C1** filled in a 2 micron ID round capillary. The red dashed line indicates the orientation of the LC columns.

5.3.2 C2

Compound **C2** exhibits a Col_{squ} honeycomb phase above the ChL_{hex} phase. The anchoring manner of **C2** sandwiched between two glass slides was examined by POM. Upon cooling from isotropic into the ChL_{hex} phase at $1\text{ }^\circ\text{C}/\text{min}$, the columns show planar-anchoring in most areas of the film (bright areas in Fig.5.8a). While in a few optical isotropic regions they are homeotropically anchored (black areas in Fig.5.8a). Interestingly, when further cooling the sample into the ChL_{hex} phase, the bright areas gradually become dark while the dark areas turn bright (Fig.5.8b-d), which indicates that the anchoring manner of the columns is reversed during the phase transition.

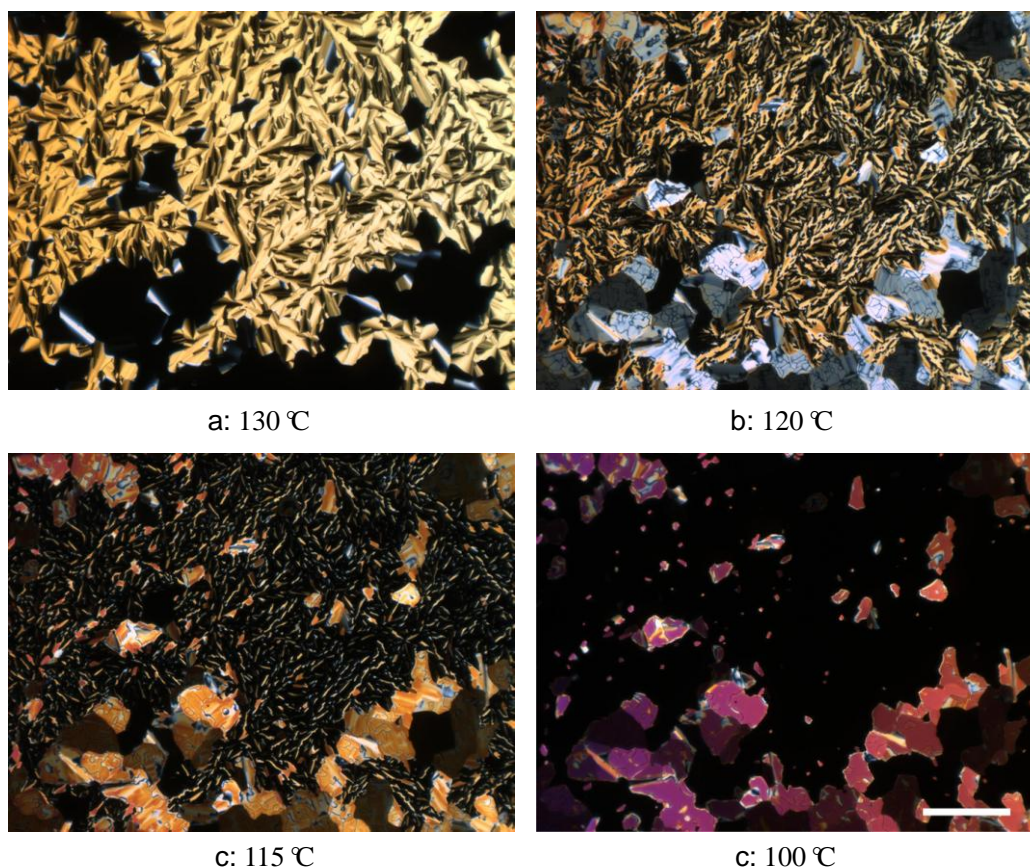


Figure 5.8 POM images of **C2** sandwiched between glasses cooled at $1\text{ }^\circ\text{C}$ from isotropic into the Col_{squ} phase (a) and gradually into the ChL_{hex} phase (b-d). Bar=200micron. Notice the bright and dark areas in (a) and (b) are exchanged, which indicates the anchoring manner of the two phases is reversed.

This behavior could be understood by considering how the aromatic molecules rotate during the phase transition, which is mainly responsible for the change of birefringence. On the flat silica wafer, the (10) plane of the Col_{squ} phase is parallel to the surface, as revealed by the GISAXS pattern in Fig.5.9a. In this configuration, the aromatic cores are

either parallel or perpendicular to the substrate surface. When transfer to the layered phase, the aromatic cores have to be parallel to each other. If they rotate in the square lattice plane, the orientation of the rods would undergo minimum change and some of them don't have to reorient at all. Fig.5.9b shows the fan-like texture in the thin film of Col_{sq} phase with one λ retardation plate. The slow axis of the compensator is indicated by the red arrow. The yellow and blue colors reveal that the orientation of the high-index axis is radial rather than tangential. Since the high-index axis is known to be parallel to the terphenyl long axis, the square columns could be determined to be curved in the fan, as illustrated on the lower right of Fig.5.9b. Due to this in-plane curvature of the square columns, only when the aromatic cores rotate to the normal direction of the substrate during the phase transition there would be no splay deformation in the resulted layered-phase.

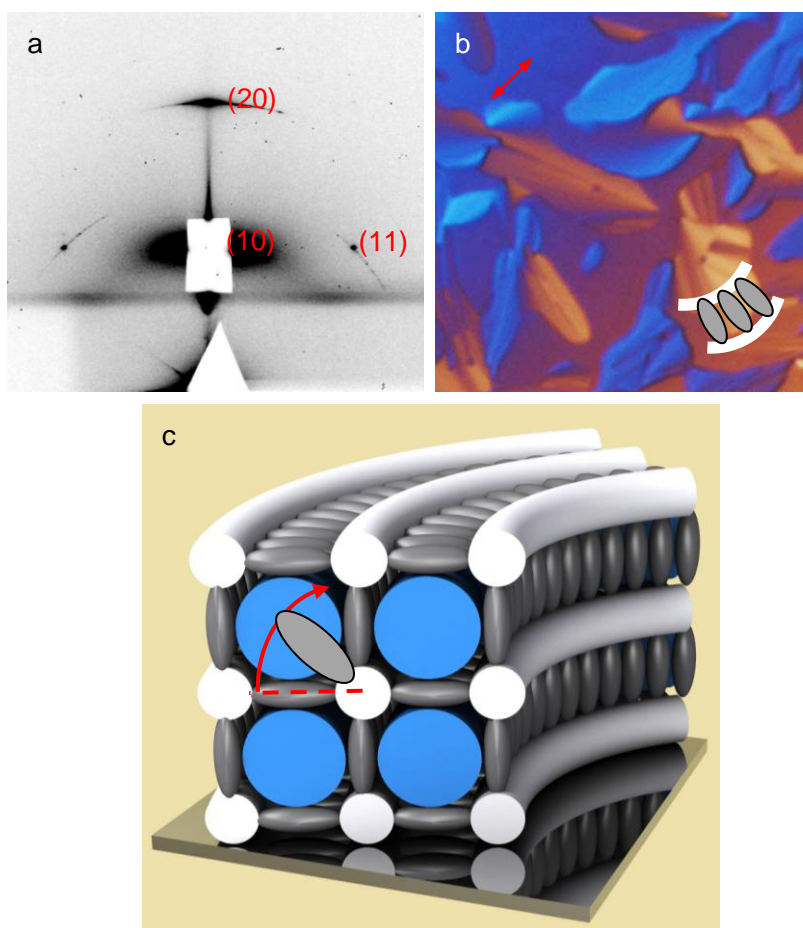


Figure 5. 9 a) GISAXS pattern of the thin film of **C1** in the Col_{sq} phase; b) birefringence texture of **C1** with λ retardation plate in place (he red arrow indicates the slow axis of the compensator); c) scheme of the planar-anchored square columns. The red arched arrow indicates the possible rotation direction of the aromatic molecules during phase transition from Col_{sq} to ChL_{hex} .

C2 in AAO template

The organization of **C2** in a 400 nm AAO template was investigated by SAXS. For the Col_{squ} phase, the orientation of the columns is perpendicular to the channel axis, as indicated by the square pattern in Fig.5.10a. The configuration then could be deduced to be mainly concentric circular since the columns are planar on the wall surface. Coincidentally, $d_{(10)}$ of the Col_{squ} phase (3.7 nm) is very close to $d_{(100)}$ of the ChL_{hex} phase (3.8 nm), and $d_{(100)}=d_{(001)}$, thus one cannot distinguish the reflections on the meridian (Fig.5.10b) simply by measuring the d-spacing. When cooled at 0.5 °C/min to 50 °C, the position of the reflections kept unchanged. Since no hexagonal (100) reflections can be seen, it can be deduced that the spot on the meridian is (001) reflection and thus the columns of the ChL_{hex} phase are parallel to the long axis of the channel. Besides, the intensity of the reflections on the equator is much stronger than that on the meridian, which is unlikely for a pure axially oriented ChL_{hex} phase. In this case we suggest that **C2** mainly forms a smectic phase in the 400 nm pores and the layers form concentric cylinders on the curved wall with homeotropic anchoring. Meanwhile a small portion of the compound forms axially oriented ChL_{hex} phase.

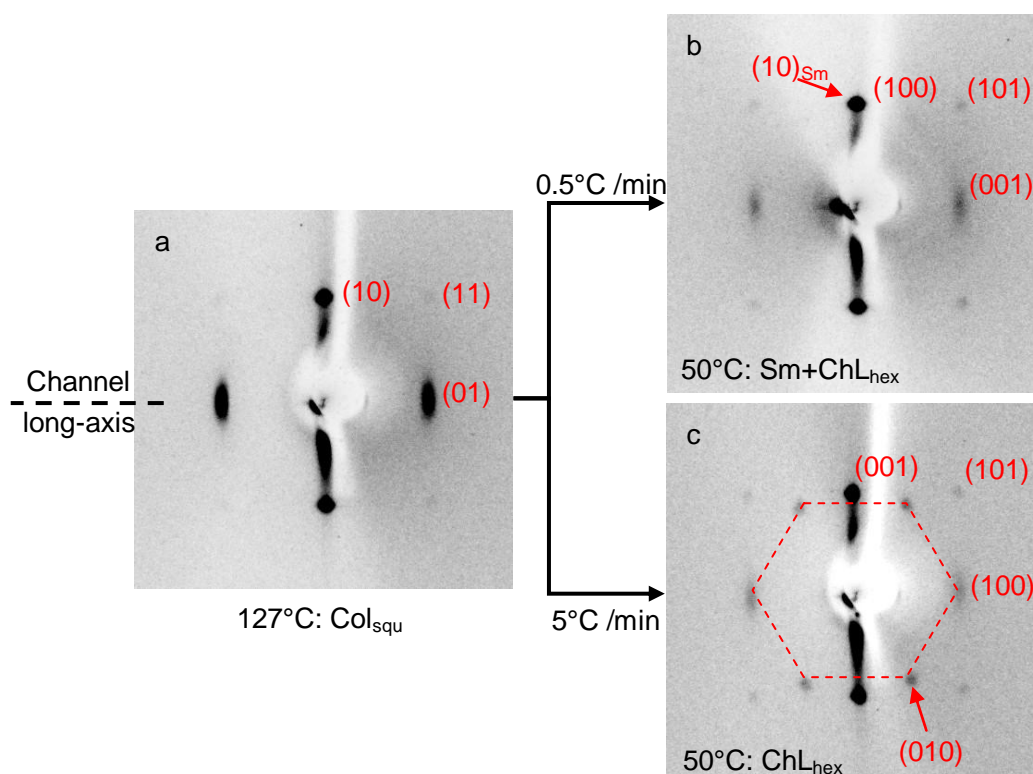


Figure 5.10 SAXS patterns of **C2** in 400 nm AAO template recorded at $\Phi=80^\circ$. Cooled from 127 °C at 0.1 °C/min (b) and 5 °C/min (c) to 50 °C, respectively.

When the sample was cooled at 5 °C/min to 50 °C, the reflections on the equator are also stronger than that on the meridian. Besides, the (100) and (010) reflections of a hexagonal lattice appear (Fig.5.10c). These indicate that the compound forms ChL_{hex} phase, and the columns are perpendicular to the channel. However there still could be smectic phase mixed with the ChL_{hex} phase considering the strong reflections on the equator.

These observations are consistent with the model of the in-plane rotation of the aromatic molecules during the phase transition on the flat surface. In the Col_{squ} phase, the columns are in a circular concentric configuration and the square lattice plane is parallel to the channel axis. Thus the terphenyl molecules are either perpendicular to the wall surface or parallel to the channel axis. During the phase transition, the molecules can rotate to both the radial and the axial directions. The former suffers from splay energy in each layer while the later causes the deformation of the hexagonal lattice. We suspect the splay energy is lower and the concentric circular configuration of the layers is favored in the cylindrical geometry. Also the terphenyl may favor homeotropic anchoring on the surface. At a slow cooling rate, the molecules turn slowly and simultaneously towards the radial direction and the aromatic cores and the alkyl chains segregate into concentric layers. However the polar columns are disturbed and the polar chains may form hexagonal ordered clusters within the terphenyl sub layers. On the other hand, under fast cooling the aromatic molecules still prefer to rotate to the radial direction. However, the rotation speed could be uneven at different locations due to the thermal fluctuation and the layer structure may develop faster in one direction and grow straight across the channel. Thus it indicates that the concentric circular smectic phase is thermodynamically more stable but the growth of the ChL_{hex} phase is kinetically favored.

C2 in round glass capillary

A thin capillary with an ID about 2.5 micron was successfully drawn from a 50 micron ID round capillary and filled with **C2**. The birefringence textures of the sample under three different thermal conditions were observed. First, in its Col_{squ} phase the tube appeared brightest when placed 45 ° to one of the cross polarizers (Fig.5.11a), indicating that the LC columns are either parallel or perpendicular to the tube. Second, the sample was cooled

into the ChL_{hex} phase at $0.1\text{C}/\text{min}$ and the birefringence became much stronger (the tube is also the brightest at 45° to the cross polarizer) (Fig.5.12b). Third, the sample was fast cooled from the CoI_{squ} phase into the ChL_{hex} phase ($20\text{C}/\text{min}$) and the brightness of the tube become non-uniform (Fig.5.13c).

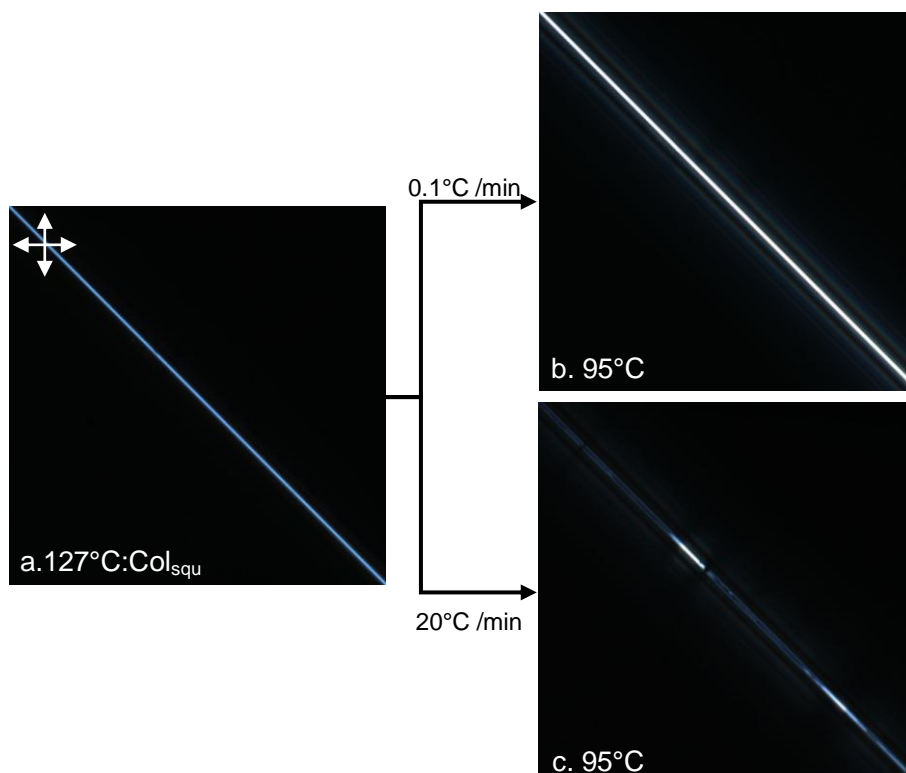


Figure 5.11 a) Birefringence textures of compound **C2** filled in a 2.5 micron ID round capillary at different temperatures: a) cooled from iso to 130°C at $1^\circ\text{C}/\text{min}$; b) slowly cooled from 130°C to 95°C at $0.1^\circ\text{C}/\text{min}$; d) fast cooled from 130°C to 95°C at about $20^\circ\text{C}/\text{min}$.

SAXS patterns of the sample under these different thermal treatments were recorded with the incident beam perpendicular to the tube axis. Fig.5.12a shows the diffraction pattern of **C2** in the CoI_{squ} phase, in which the (01) reflections on the meridian are much stronger than the reflections on the equator. When the tube was rotated the position and intensity of the four spots didn't change. Thus it reveals that the columns are in a circular-concentric configuration. For the slowly cooled sample, as the tube is rotated, the reflections show up on the equator at several α angles, but those on the meridian remained constant (Fig.5.12b). Thus the intensities on the meridian can be deduced to be (001) and the columns are axially

oriented. In this scale, the capillary can no longer support the concentric smectic layers probably due to the increased splay energy of the aromatic cores.

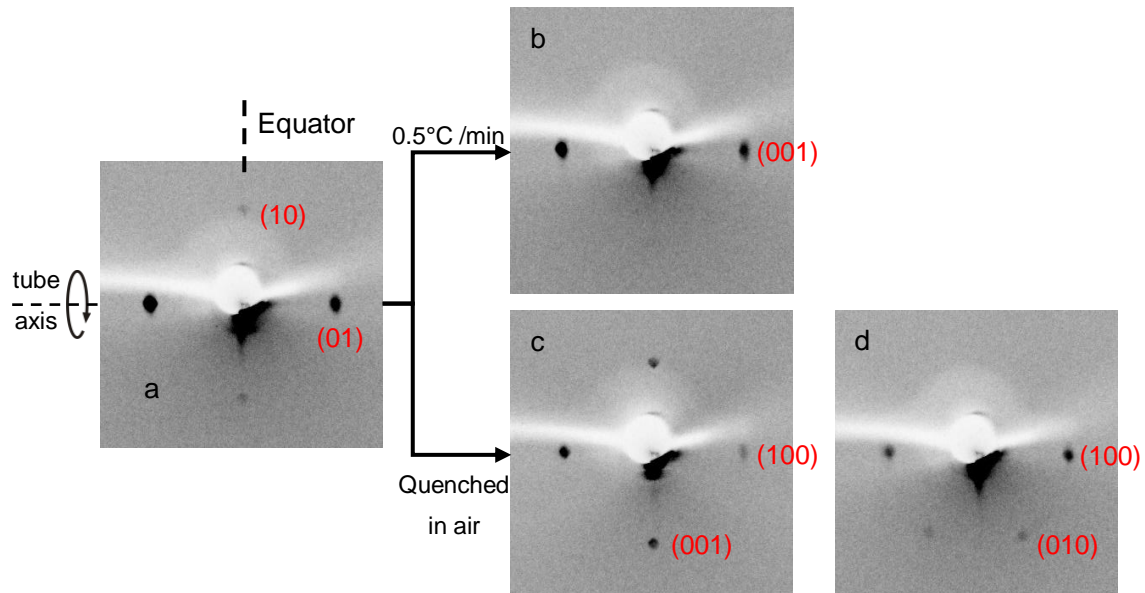


Figure 5.12 SAXS patterns of **C2** in a 2.5-micron ID capillary: (a) at 127 °C the Col_{squ} phase is in concentric circular configuration; (b) cooled at 0.5 °C /min from 127 °C to 50 °C; (c) and (d) cooled at 5 °C /min from 127 °C to 50 °C; (d) α rotated 90° from (c). The asymmetry of the intensities in (c) is resulted from the curved capillary.

For the fast cooled sample, the reflections on the equator were recorded at angle α_1 (Fig.5.12c), and when α_1 was increased by 90°, the off-equator hexagonal spots show up (Fig.5.12d). It indicates that the polar columns are oriented radially across the tube. These results are in agreement with the POM observation. In the circular-concentric Col_{squ} phase only the portion of columns parallel to the observation plate can contribute to the birefringence, resulting in weak brightness (Fig.5.11a); upon slow cooling, the columns of the ChL_{hex} phase became axially oriented and thus largely enhanced the birefringence (Fig.5.11b). In Fig.5.11c the dark area is probably due to the polar configuration of the homeotropic-anchored columns where the LC columns cross through the tube and are perpendicular to the observation plate.

5.4 Conclusion

In this chapter we studied the configuration of ChL_{hex} phase in cylindrical confinement. For compound **C1**, the 3d phase is suppressed in the 60 nm pores, instead the layers are wound up concentrically on the curved wall with homeotropic anchoring and form smectic phase. When the pore size was increased to 400 nm, it formed an axially oriented ChL_{hex} phase. This was suggested to be the result of the rigid columns and the relatively flexible hexagonal lattice of the ChL_{hex} phase. Further increasing the cavity size to 2 micron by using a capillary tube resulted in a monodomain of the ChL_{hex} phase, in which the columns tilt 40° away from the tube axis. This tilting angle increased to 70° in an 8 micron capillary.

For compound **C2**, it was demonstrated how the cooling rate can affect the phase transition and the final configuration of the LC in the cylindrical geometry. During slow cooling from the Col_{squ} phase, the compound mainly forms smectic phase in the 400 nm pores. In this case, the splay energy in the smectic layers is probably lower than the distortion energy of the hexagonal lattice in the ChL_{hex} phase. However the curvature can no longer support the circular concentric smectic phase when the cylinder increased to 2.5 micron due to the increased splay energy and instead an axially oriented ChL_{hex} phase forms. While under fast cooling the ChL_{hex} phase orients with the columns perpendicular to channel axis both in the submicron and micrometer cylinders. It indicates that the concentric circular smectic phase is thermodynamically more stable but the growth of the ChL_{hex} phase is kinetically favored.

CHAPTER 6 Columnar Discotic Liquid Crystals in Cylindrical Confinement

6.1 Introduction

In this chapter, the alignments of columnar discotic liquid crystals (CDLCs) in cylindrical geometries are investigated. Compared to the columns formed by T-shaped molecules, the formation of discotic columns is quite straightforward: the disk-like molecules stack into columns as a result of their flat shape and the π - π interaction of the polyaromatic cores. Thus the rigidity of the discotic columns could be higher than that of the honeycomb columns which are either filled by flexible alkyl chains or polar groups. Also, the inter-columnar interaction could be weaker than that of the interconnected honeycomb network. As a result different phenomena could be expected for the discotic system confined in the cavities. The effect of the size of the confinement, the rigidity of the CDLCs columns and the surface anchoring condition on the orientation of the discotic columns in cylindrical confinement are investigated. To evaluate the effect of cavity size, AAO templates with nano-scale pores and micrometer glass capillary tubes were used; to modify the rigidity of the columns, different discotic molecules and doped systems were investigated; to change the surface anchoring manner of the columns, surfactant was used to modify the polarity of the inner surface of the cavities.

6.2 Compounds

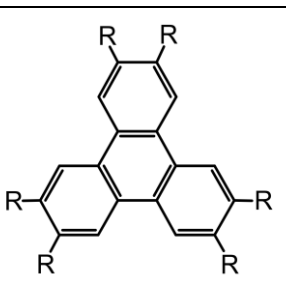
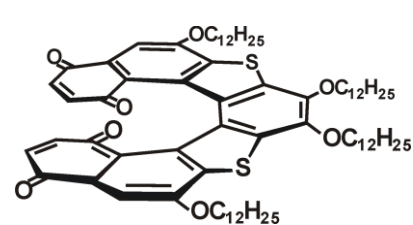
Name	Molecular Structure	Phase transition (°C)	$a_{\text{hex}}(\text{Å})$
D1		Cr 69.5 Col _h 100 iso	18.7 (at 80 °C)
D2		Cr 62 H 70 Col _h 93 iso	18.37 (at 80 °C) 18.74 (at 65 °C)
D3		rt Col _h /215 iso	40

Table 6.1. Molecular formulas, phase transition temperatures and lattice parameters of compounds **Dn**. Cr=crystal; Col_h=columnar hexagonal phase; a_{hex} =lattice parameter of hexagonal phase; iso=isotropic liquid; H=helical phase; rt=room temperature.

6.3 Triphenylene-based mesogens

Triphenylenes are the most synthetically accessible discogens and the only discogen currently made on a commercial scale^[93]. The triphenylene core is composed of three benzene rings that give a planar rigid aromatic unit, which tends to lie on top of each other due to the π - π interaction and form columnar mesophases. The six peripheral alkyl chains are highly disordered and crucial to the formation of the columnar phase^[94]. In this section two triphenylene derivatives were used. Compound **D1** is a symmetrical hexaether derivative of triphenylene, 2,3,6,7,10,11-hexakisethoxy- triphenylene. Compound **D2** has similar structure except the oxygen atoms are replaced by sulphur. It was reported to exhibit an additional helical (H) phase below the columnar hexagonal phase^[95]. The new, more ordered phase has been characterized to possess a superimposed helical structure of the columnar stacks, and the charge carrier mobility is found to be substantially greater in this phase^[96].

6.3.1 Homeotropically anchored columns

On cooling from the isotropic into the hexagonal columnar phase, a face-on orientation of the discotic molecules was generally found to be more favorable at the substrate/LC interface, leading to the homeotropic anchoring of the columns^[97]. The anchoring manner of **D1** on the glass surface was determined by POM. The thin film of **D1** sandwiched between two glass slides was cooled from isotropic temperature to 80 °C at 0.1 °C/min. It was totally dark when observed by POM with two cross polarizers in place (Fig.6.1b), which is evidence of homeotropic anchoring of the columns. The Col_{hex} phase of **D2** also shows homeotropic anchoring. Thus the anchoring manner of the discotic columns inside the pores of AAO template are expected to be homeotropic as well, considering the similar polarity of the glass and alumina surfaces.

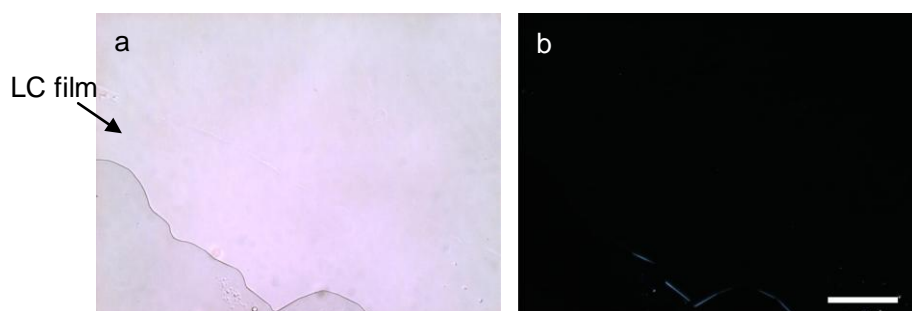


Figure 6.1. Optical microscope images of **D1** sandwiched between two glass slides: a) observed without analyzer; b) with cross polarizers. The bar represents 200 micron.

60 and 20 nm AAO template

The orientation of compound **D1** in 60 and 20 nm AAO templates were examined by SAXS. All samples were heated to isotropic temperature and slowly cooled at 0.1 °C /min to 80 °C before SAXS exposure. For the discotic columnar phase, the dominant reflection is the (100) peak.

When **D1** was admitted in the 20 nm template, only powder-like (100) diffraction rings were obtained by SAXS at lower α angle. However, when the template was rotated to higher α , the intensity became stronger on the meridian, as shown in Fig.6.2a. This indicates that columns are still mainly perpendicular to the channel axis, otherwise the (100) intensity would have concentrated on the equator. However, the columns have no preferred in-plane orientation of the hexagonal lattice. That is the orientation of the hexagonal lattice is randomized around the column axis, which, in turn, is randomized in a plane perpendicular to the pore axis. The reciprocal space is schematically drawn in Fig.6.2b. For all pores in which the columns lie in one particular direction normal to the pore axis, the reciprocal {100} points describe a ring lying in a plane parallel to the pore axis. For example, the green dashed line indicates one direction normal to the pore axis, and the reciprocal {100} points of columns parallel to this direction form a green ring lying in a plane perpendicular to the green dashed line. Since the diffraction pattern gives the average orientation distribution over the entire irradiated volume which covers many nanopores, the direction of the columns is randomized around the channel axis. Thus, while only those (100) reciprocal rings lying exactly on the Ewald sphere contribute to the intensity of the ring in the diffraction pattern, all (100) rings would cross the poles and contribute to the (100) intensity on the meridian.

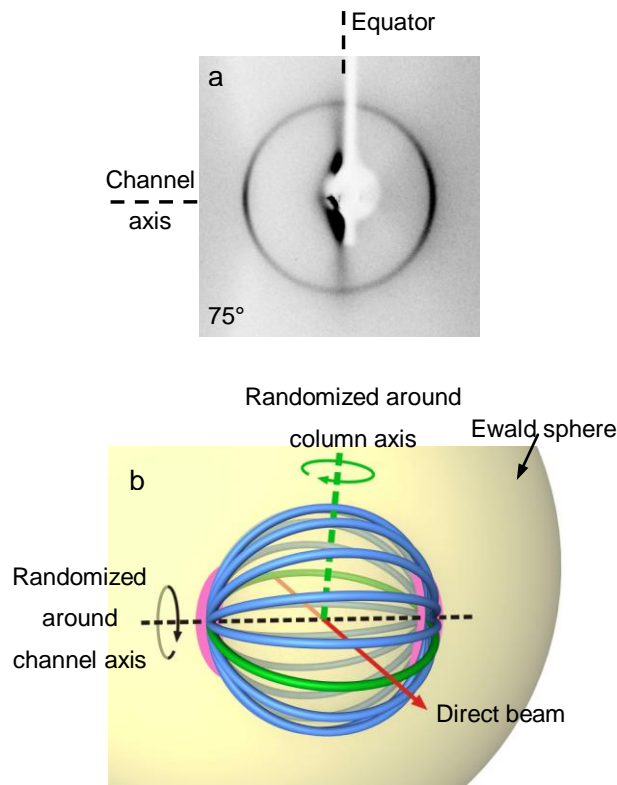


Figure 6.2 (a) SAXS pattern of **D1** in a 20 nm AAO template recorded at $\Phi=75^\circ$; (b) scheme of the reciprocal space of $\{100\}$ reflection group, from many pores, cutting the Ewald sphere at $\Phi=90^\circ$.

Fig.6.3 shows the SAXS patterns of the 60 nm AAO template filled with **D1** at selected rotation angles. At $\Phi=0^\circ$ it shows a uniform (100) diffraction circle. As Φ increases, a set of (100) intensity maxima condenses on the equator (Fig.6.3a). When Φ reaches about 54° , a new set of (100) spots appears near the meridian (Fig.6.3b), which split and move rapidly away with Φ increasing further (Fig.6.3c). As Φ angle increases further, the positions of the six intensity maxima on the (100) ring gradually form a regular hexagon (Fig.6.3d). Note that the intensities become weak at high Φ angle due to the strong absorption of the X-ray by the AAO membrane, especially on the equator in the direction of which the refracted beams go through a long path inside the template. No distortion of the lattice was observed as all the intensity maxima are lying on a circle. Also the d-spacing of (100) reflection is calculated the same as that of the bulk material, which indicates the confinement does not change the intercolumnar distance.

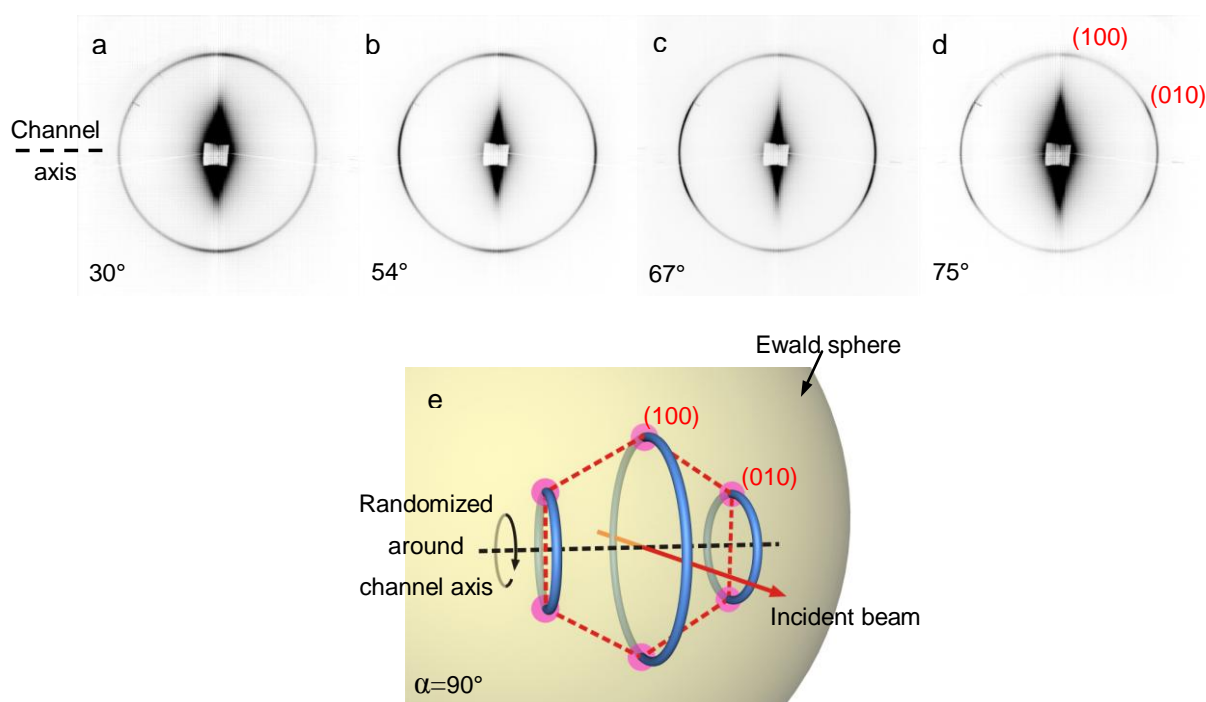


Figure 6.3. (a-d) SAXS patterns of **D1** in 60 nm AAO template recorded at a series of Φ angles. The rotation angle Φ is indicated in each image. Note that at $\Phi=80^\circ$ the intensities are weak and those on the equator are invisible due to the strong absorption of the X-ray by the template. (e) scheme of the reciprocal space of {100} reflection group, from many pores, cutting the Ewald sphere at $\Phi=90^\circ$.

Based on the changes of the diffraction pattern, the reciprocal space is illustrated in Fig.6.3e. It indicates that the columns are mainly perpendicular to the nanochannel, with the (100) plane of the hexagonal lattice parallel to the channel axis. However the arch-like intensity maxima reveal that the orientation of the hexagonal lattice is poor. In fact at any Φ angle a powder-like (100) diffraction ring always coexists with the diffraction spots, which indicates that some of the hexagonal domains are randomly oriented.

400 and 200 nm AAO templates

Fig.6.4 shows the diffraction patterns of **D1** in 400 nm AAO template at a series of Φ angles. As Φ increases, there is no intensity maximum that shows up on the equator as observed for 20 and 60 nm samples. When Φ reaches about 30°, a set of (100) intensity

maximum appear near the meridian and splits rapidly away with Φ increasing further. At the largest accessible Φ angle of about 80° , a new set of (100) intensity appears on the meridian and the positions of the six intensity maxima described close to a regular hexagon. The hexagonal diffraction pattern indicates that the LC columns are mainly perpendicular to the long axis of the nanochannel.

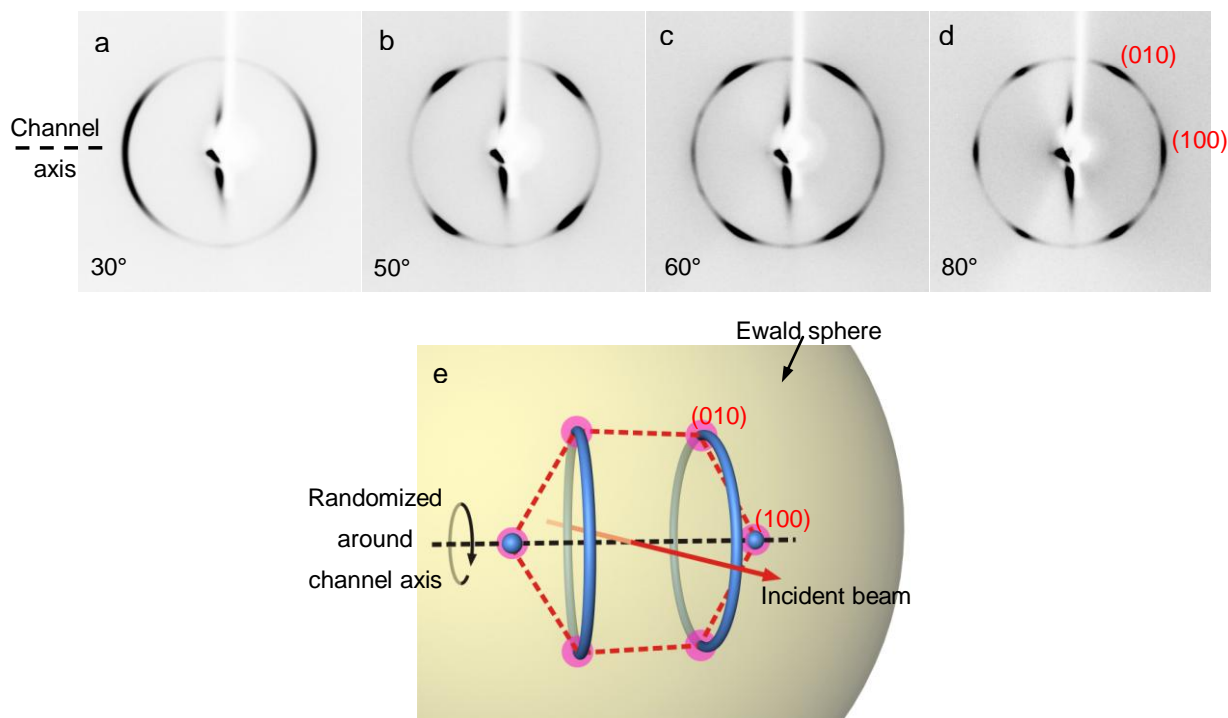


Figure 6.4 (a-d) SAXS patterns of HAT6 in 60 nm AAO template recorded at a series of Φ angles. The rotation angle Φ is indicated in each image. Note that at $\Phi=80^\circ$ the intensities are weak and those on the equator are invisible due to the strong absorption of the X-ray by the template. (e) scheme of the reciprocal space of {100} reflection group, from many pores, cutting the Ewald sphere at $\Phi=90^\circ$.

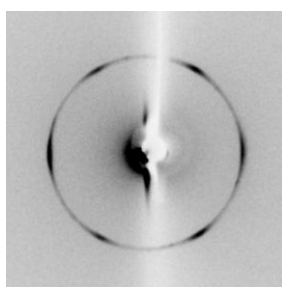


Figure 6.5 SAXS patterns of D1 filled in 200 nm AAO template recorded at $\Phi=80^\circ$.

Compared with the 60 nm sample, the in-plane orientation of the 2-d lattice in the 400 nm diameter pore has turned in-plane by 30° . Now the (100) plane is perpendicular to the channel axis. In the case of the 200 nm AAO template filled with **D1**, the hexagonal lattice shows the same orientation as in 400 nm pores (Fig.6.5). This is similar to what we observed for the homeotropic-anchored honeycomb phase in chapter 4, and could be explained by the same mechanism.

Turning to compound **D2**, similar SAXS pattern was obtained for the 20 nm template sample. However, the reflection spots for the 60 nm sample are much narrower azimuthally than those of **D1** (Fig.6.6). A plausible reason is that the sulphur atoms increase the inter-columnar interaction, resulting in a stronger tendency for the hexagonal lattice to align on the curved surface with the (10) plane parallel to the long-axis of the channel in the nucleation stage of the Col_{hex} phase.

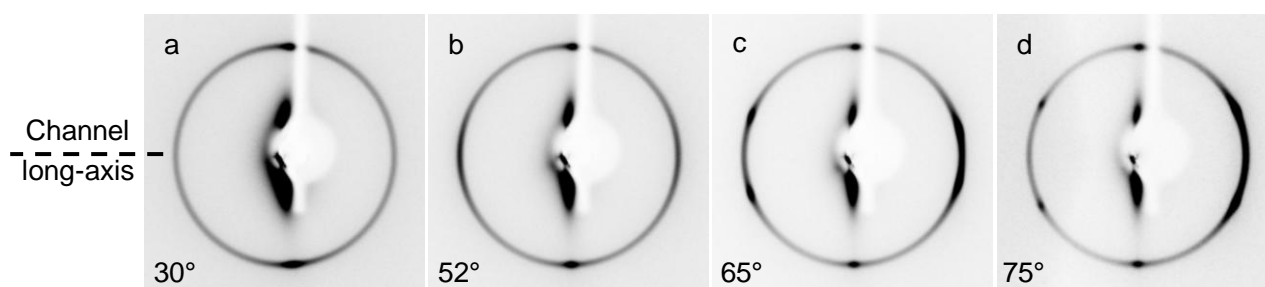


Figure 6.6. SAXS patterns of **D2** in 60 nm AAO template recorded at a series of Φ angles. The rotation angle Φ is indicated in each image.

When introduced in the 400 nm template, **D2** also shows the orientational change of the hexagonal lattice (Fig.6.7), as observed for **D1**. However, (100) peaks of relatively low intensity can also be seen on the equator. This is not accompanied by four additional arcs around 60° away azimuthally as in the case of the 60 nm template. This can only be interpreted as meaning that some columns are axially oriented. This is likely due to the increased column rigidity brought about by the strong intermolecular interactions of the sulphurs.

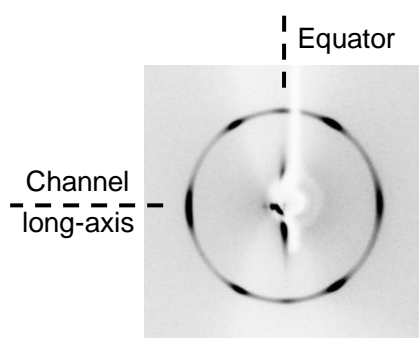


Figure 6.7. X-ray diffraction patterns of **D2** filled in the 400 nm AAO template. $\Phi=75^\circ$.

So far the results of our study of the columnar phase of triphenylene derivatives confined in the AAO templates contradict the previously reported conclusion^[52] that the columns are mainly parallel to the nanochannel (as introduced in chapter 1.4.2). There are two main issues that may have caused the difference:

1. The orientation of the 2-d hexagonal lattice with respect to the axis of the channel was not considered in the previous report. With the XRD setup, they could only collect the (100) intensity on the meridian. However, in the 60 nm diameter pore, none of the reciprocal hexagonal lattice point is located on the meridian (Fig.6.2), and the intensity they recorded is from the weak (100) ring, which is contributed from the randomly oriented hexagonal lattice.
2. They didn't consider the difference between the absorption of the X-ray by the AAO membrane when recording the (100) and (001) reflections using $\theta/2\theta$ scan. As schematically illustrated in Fig.6.8, the X-ray beam is directed at the sample surface at an angle θ of 2.65° to record the (100) reflection, corresponding to an intercolumnar distance of 1.85nm. At this incident angle the beam would be strongly absorbed by the AAO membrane as it passes through a long path in the AAO membrane. On the other hand, the incident angle is about 17.75° to the sample surface when recording the (001) reflection. In this case the path through the membrane is much shorter and thus less absorption of the X-ray beam. Thus the comparison between the (100) and (001) intensities may give wrong

information about the ratio between the homeotropically and axially oriented columns.

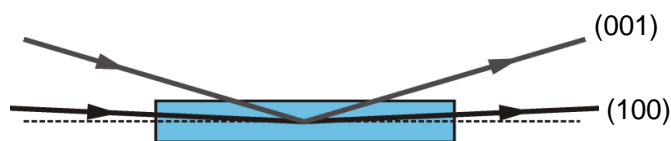


Figure 6.8. Schematic drawing of the path of the X-ray beam inside the AAO membrane when recording the (100) and (001) reflections of the discotic columnar phase using $\theta/2\theta$ scan in ref [chap1(7)].

Glass capillaries

The capillary samples were prepared using the same procedure as described in chapter 1. Three pore sizes were used in the study of compound **C1**: 3.4, 50 and 100 μm in inner diameter (ID). For the 3.4 micron sample, when observed between two crossed polarizers the tube exhibited a maximum in transmission when it was oriented at 45° to the polarizers (Fig.6.9a) and almost no light transmission when parallel to one of the polarizers. This indicates that the optical axes of the LC columns are either perpendicular or parallel to the long-axis of the capillary tube, with uniform orientation. A wedged retardation plate was used to further determine the orientation of the columns. The wedged plate was inserted at the position that 1λ retardation was placed at the centre of the optical path of the microscope with the slow axis at $+45^\circ$ to the polarizer. When a birefringent sample is observed through the microscope with the compensator in place, the colour would change according to the orientation of the sample. If the slow axes of the sample and the compensator are parallel, the total birefringence is increased, and the stripe will appear second order blue. If the slow axis of the sample is orthogonal to that of the compensator, the total birefringence is decreased and the stripe will appear second order yellow. Fig.6.9 (b, c) reveal that the orientation of the slow axis of the sample is parallel to the tube. Since the slow optical axis of a discotic column is perpendicular to it, we can conclude that the LC columns are perpendicular to the capillary axis.

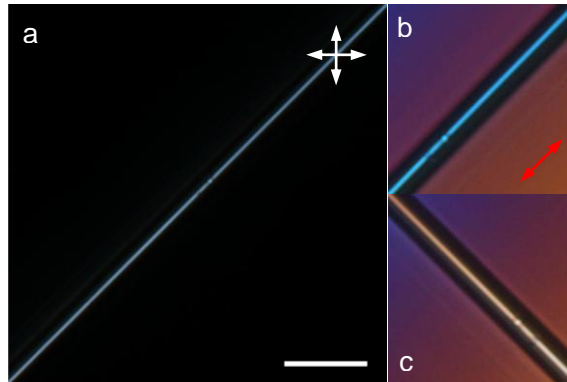


Figure 6.9 HAT6 filled in a 3.4 μm ID capillary: (a) the capillary is oriented 45° to the crossed polarizers; (b, c) the orientation is $\pm 45^\circ$ to the polarizers with the compensator in place. The red line indicates the orientation of the slow axis of the compensator.

To further confirm the orientation of the columns as well as the hexagonal lattice, a SAXS experiment was performed on the capillary sample. During the SAXS experiment, the capillary tube was mounted horizontal and perpendicular to the incident beam. The tube was rotated around its long-axis and a series of diffraction patterns were recorded at different α angles, as shown in Fig.6.10. $\alpha=0^\circ$ is arbitrarily assigned to the angle at which the hexagonal pattern appears, as shown in Fig.6.10a. As α increasing the four off-meridian (100) intensity maximum first became weak and then disappeared, as shown in Fig.6.10(b-c). It indicates that the columns are in polar configuration in which the columns grown perpendicular to the wall surface and cross the cylinder from one side to the other, with expected bend and splay at the end of the columns. The cross section of the capillary corresponding to different α angle is schematically shown below each diffraction pattern, in which the black curves represent the director of the columns and the red arrows represent the incident X-ray beam at different α angles. Compared with the arch-like diffraction intensities obtained from the 400 nm template, the sharp diffraction spots indicate that the hexagonal lattice is much better oriented with its (100) plane perpendicular to the cylinder axis. In the μm meter capillary, the splay deformation is largely increased. Thus this observation is consistent with our assumption that the columns prefer to splay along the (100) plane of the hexagonal network, which gives rise to the orientational change of the hexagonal lattice when the size of the cylinder increases.

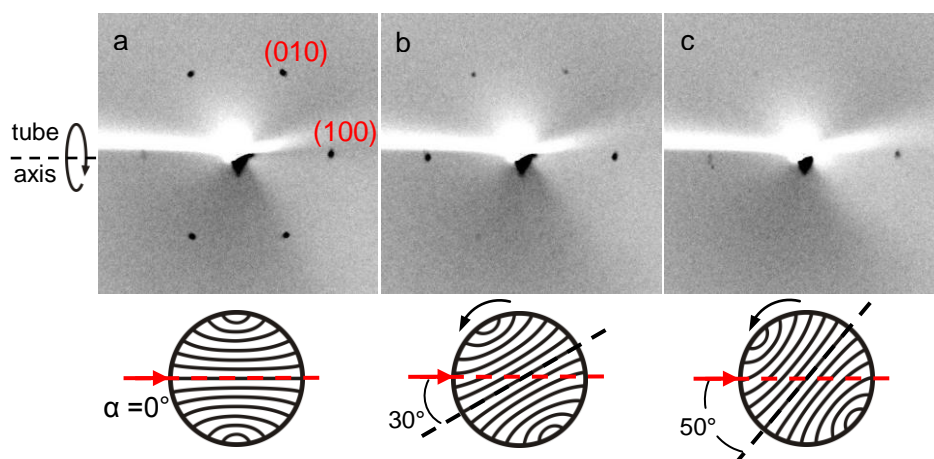


Figure 6.10 (a-c) SAXS pattern of HAT6 in a 3.4 μm ID capillary recorded at different rotation angle α as indicated at the corner of each images; Corresponding sketch of the cross section of the capillary are shown below each diffraction pattern. The black curves represent the director of the columns and the red arrows represent the incident X-ray beam at different α angles.

For the 50 μm ID capillary, the columns still show radial configuration, as revealed by the diffraction patterns in Fig.6.11. However the (100) plane of the hexagonal lattice is tilted away from the long-axis of the cylinder tube.

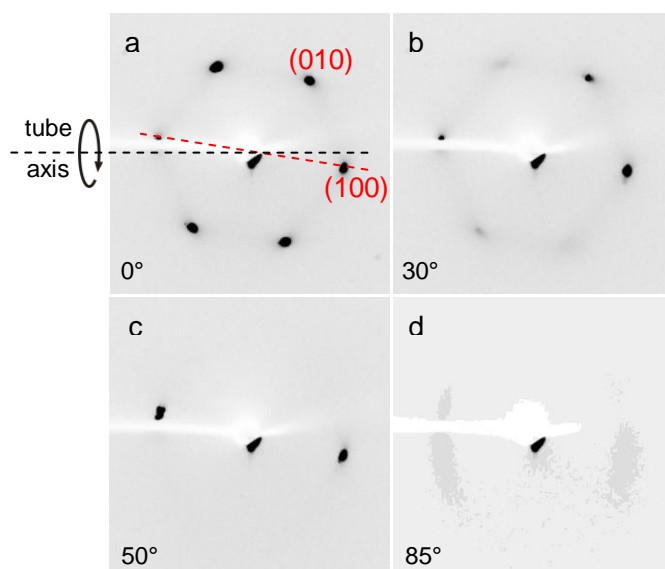


Figure 6.11 SAXS patterns of HAT6 in a 50 μm ID capillary recorded at different rotation angles α as indicated at the corner of each image.

When the inner diameter of the capillary was increased to 100 micron, the configuration of **D1** showed some variations. In some segments of the tube, polar configuration was observed directly by SAXS as that in the 50 micron sample, while in others different diffraction patterns were obtained, as shown in Fig.6.12. $\alpha=0$ is arbitrarily assigned to the rotation angle at which the hexagonal pattern was obtained (Fig.6.12a). It is obvious that the intensity of the spots on the equator is much stronger than that of the off-equatorial spots. As illustrated in chapter 3, the hexagonal intensities come from the hexagonal columns that are perpendicular to the tube, while the strong intensities on the equator indicate there are more columns oriented parallel to the tube. As the tube rotates, the reflections on the equator gradually fade away; meanwhile the four off-equator spots move toward the equator and finally merged on the equator. These mark the crossing of the Ewald sphere by the $\{10\}$ reciprocal rings and the (10) , $(\bar{1}0)$ reciprocal spots generated by the rotating of the hexagonal lattice plane around a $[10]$ direction. Based on the observed changes in the diffraction pattern at increasing α , the reciprocal space of the $\{10\}$ reflection group inside the glass tube was schematically drawn as green contour in Fig.6.12f. Here the $\{10\}$ reflection group is separated in two rings and two spots in reciprocal space. Accordingly, the orientation of the LC columns can be deduced, as shown in Fig.6.12g. It represents the escaped radial configuration, as observed in nematics confined in cylindrical cavities. The columns are homeotropic near the wall surface, and bend to escape to the third dimension along the axis of the tube.

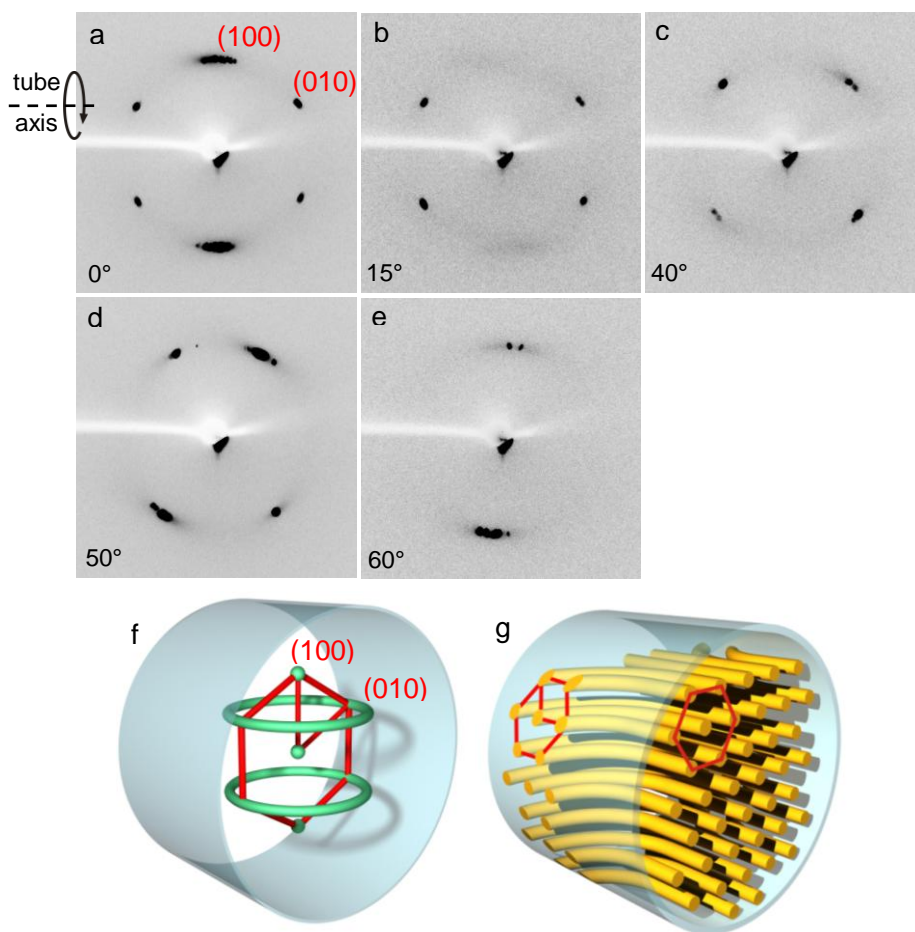


Figure 6.12. a) to e): SAXS pattern of compound **D1** in a 100 micron ID capillary recorded at different rotation angles α as indicated at the corner of each image; f) sketch of the geometry of the reciprocal space in the tube. The green circles and spheres represent the reciprocal space of the $\{10\}$ reflection group, and the red hexagon indicates the orientation of the reciprocal space; g) sketch of the Col_{hex} phase inside the tube.

6.3.2 Planar-anchored columns

In this section, the configuration of the discotic columns in cavities where planar anchoring is favored at the solid/LC interface is explored. Geerts' group reported the planar alignment of a phthalocyanine derivative, attached to eight oligo(ethyleneoxy) peripheral substituents,

between two hydrophobic surfaces (glass slides coated by the benzocyclobutene-based cross-linked polymer)^[98]. In our study, we studied the anchoring manner of **D1** sandwiched between two glass slides coated by hexadecyltrichlorosilane (HTS) self-assembled monolayer (see the detailed procedure in chapter 2). The birefringence textures between cross polarizers confirmed that at different cooling rate, the alignment of **D1** is always planar in the very thin film, as shown in Fig.6.13a.b.

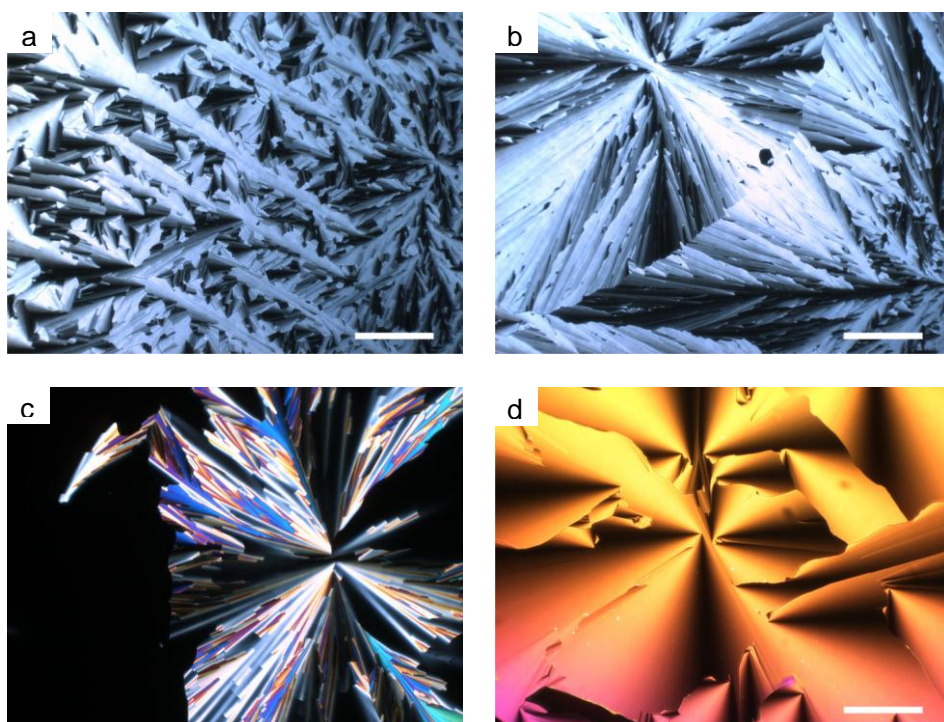


Figure 6.13. Birefringence textures of **D1** sandwiched between two HTS modified glass slides. a) and b) are very thin film, cooled at 0.1 and 1 °C /min, respectively. c) and d) are thicker film, cooled at 0.1 and 1 °C /min, respectively. The bar represents 200 micron.

However, in the thicker film a slow cooling rate (0.1 °C /min) leads to a mixture of homeotropic and planar alignments (Fig.6.13c), and only under faster cooling rate (≥ 0.5 °C /min) a pure planar alignment could be obtained (Fig.6.13d). To ensure the planar anchoring in the cavities as well as to obtain an equilibrium configuration, we used a cooling rate of 0.5 °C /min for all the samples studied in this section.

Silane-modified 20 and 60 nm AAO templates:

As discussed before, the diffraction pattern of the 20 nm template filled with D1 shows in-plane random orientation of the hexagonal lattice, as indicated by the intensity maxima on the meridian (Fig.6.14a). However, for the HTS treated 20 nm AAO template sample, it shows the hexagonal pattern, which indicates the (100) plane of the 2-d hexagonal lattice is parallel to the channel axis (Fig.6.14b). The SAXS pattern of the treated 60 nm template sample is shown in Fig.6.14d. Compared with the arch-like intensity maxima obtained from the untreated 60 nm template sample (Fig.6.14c), the reflection spots are narrower azimuthally. These indicate that after the surface treatment the hexagonal lattice of the columnar phase becomes well oriented with its (100) plane parallel to the channel axis. It is interesting that for the planar-anchored Col_{hex} phase of **D1** on the flat surface, the orientation of the 2-d lattice is with the (100) plane parallel to substrate surface, as revealed by GISAX (Fig.6.15a). This is probably due to the fact that in this orientation the hexagonal network is the least deformed by the LC/solid interface (Fig.6.15b), as similar to that observed for the honeycomb phases. We suggest that the anchoring manner of the columns inside the nanopores has been changed to planar, and the improved orientation of the hexagonal lattice comes from its preferred orientation on the wall surface.

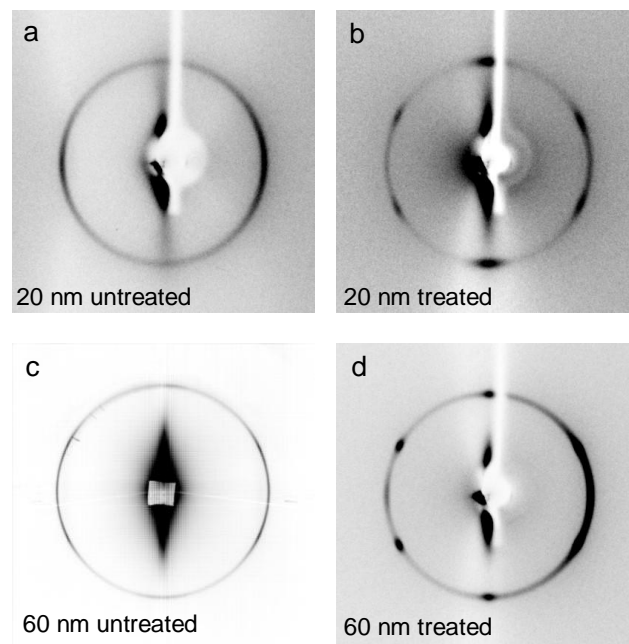


Figure 6.14. SAXS of treated (right side) and untreated (left side) templates filled with **D1**. $\alpha=75^\circ$.

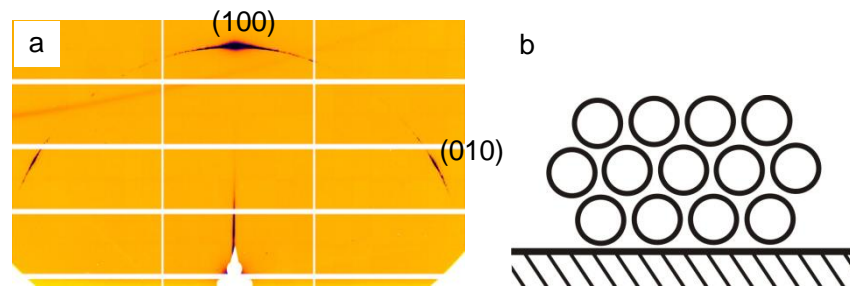


Figure 6.15. a) GISAX pattern of the planar-anchored Col_{hex} phase of **D1** on glass surface; b) schematic drawing illustrating the orientation of the hexagonal lattice on the substrate surface. Cross sections of **D1** columns are symbolized by circles.

For the 20 nm sample, it can be noticed that the (100) intensity maxima on the equator are stronger than the others, considering the strong absorption of the reflection by the membrane on the equator and the fact that a Lorentz-type correction would enhance the equatorial intensity still further. The correction involves multiplication of intensity by $\sim \sin\rho$, where ρ is the polar angle, i.e. the angle between the 100 reciprocal vector and the pore axis). The excess equatorial intensity implies that some columns have become axially oriented. An assumption could be that in such small pores, the columns are forced to align along the channel axis close to the center of the cylinder in order to relieve the bend deformation energy.

Silane-modified 400 nm AAO template:

We have observed in the untreated 200 and 400 nm diameter pores that the hexagonal lattice of **D1** orients with its (100) plane perpendicular to the channel axis (Fig.6.4, 6.5). However, when filled in the modified 400 nm template, the orientation of the 2-d lattice changes again to be with the (100) plane parallel to the channel axis, as can be told by the sharp hexagonal spots in Fig.6.16b.

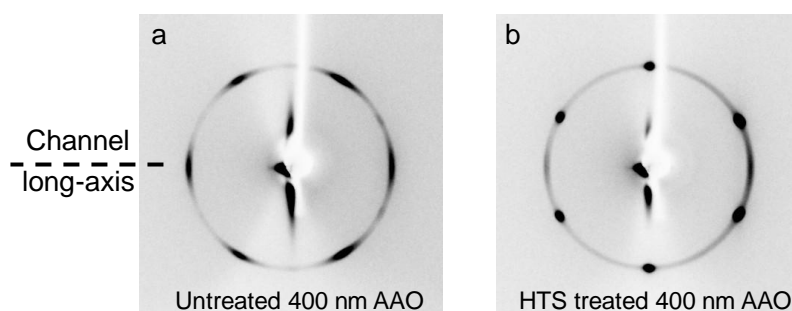


Figure 6.16. SAXS patterns of **D1** in 400 nm templates: a) untreated; b) treated by HTS. $\alpha=80^\circ$.

This result is consistent with that of **D1** in the modified 20 and 60 nm templates, and also with that of the planar-anchored hexagonal honeycomb. Thus it proves again that the orientations of the hexagonal lattice in homeotropic and planar anchoring environments are determined by different mechanism.

Silane-modified 50 micron ID glass capillary

We have discussed in chapter 3 that planar anchored hexagonal columns may grow along the curvature to form circular concentric or bipolar configuration, or else align along the axis of the cylinder to form axial configuration. In the first case the columns mainly undergo bend deformation, while in the latter there is in-plane distortion of the hexagonal lattice. As the diameter of the cylinder decreases, both the bend deformation energy of the columns and the distortion energy of the hexagonal lattice increase. So far we have observed that in AAO nanopores the discotic columns prefer to bend rather than grow along the cylinder axis even when the pore diameter is as small as 20 nm. To examine column orientation in large cavities, we filled a HTS-treated glass capillary with **D1**.

The orientation of **D1** in a 50 micron ID modified glass capillary was observed by POM. Interestingly, extinction lines that are tilted about 30° away from the tube axis can be seen, the direction of which is indicated by the red arrow in Fig.6.17. Unlike the untreated 50 micron ID capillary sample, the birefringence of the modified sample does not become the brightest placed 45° to the crossed polarizers (Fig.6.17a), nor does it extinguish when turned parallel to the polarizer (Fig.6.17c). Instead the optic axis is along these striations, as revealed by Fig.6.17b and d. From these images we can see that the orientation of the columns is not simply perpendicular or parallel to the tube axis but tilted. In Fig.6.17e it can be seen that the orientation is changed and a defect occurs.

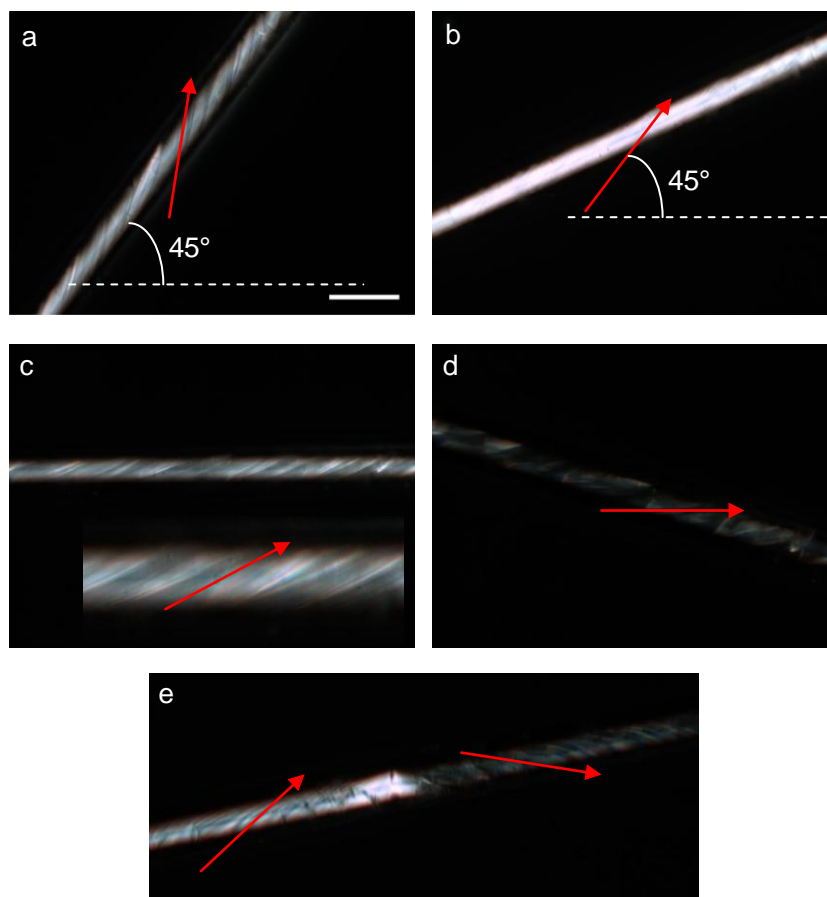


Figure 6.17. POM images of modified 50 micron ID capillary filled with **D1**. The red arrow indicates the direction of the extinction lines. a) and b): the tube or extinction lines are 45° to the analyzer, respectively. The bar in a) represents 100 micron.; c) and d): the tube or the extinction lines are parallel to the analyzer, respectively. The image is amplified in c). e) the direction of the extinction lines changes.

SAXS experiment was performed to further determine the orientation of the LC columns. As α increases four of the (100) reflection spots start to fade away (Fig.6.18b-c). Finally only two intensity maxima left (Fig.6.18d). The hexagonal pattern in Fig.6.18a indicates some of the columns are perpendicular to the tube; while the two spots in Fig.6.18d represent columns orient about 60° to the tube axis.

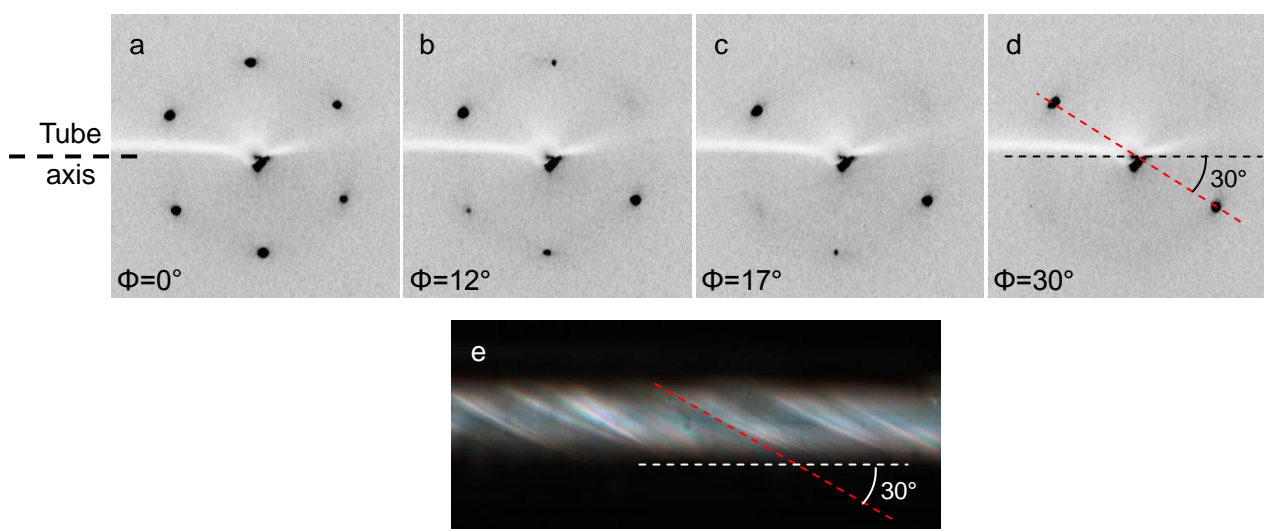


Figure 6.18. SAXS pattern of compound **D1** in a 50 micron ID capillary recorded at different rotation angle α as indicated at the corner of each images. The red dashed line indicates the orientation of the LC columns, which is perpendicular to the direction of the extinction lines.

Since the diameter of the incident X-ray beam is about 400 micron, which covers several segments of different orientations of the columns, the obtained diffraction patterns may be a mixture of different segments. However the orientation of the columns in Fig.6.18d is consistent with the POM observation and it can be deduced that the columns are perpendicular to the fiber-like texture, as illustrated by the red dashed line. Thus these observations evidence a tilted orientation of the discotic columns with respect to the axis of the cylinder. This is probably due to the large radius of the tube that the distortion energy of the hexagonal lattice caused by the curvature decreases and the columns chose to orient at certain direction in which the deformation energy of the 2-d lattice balances with the bend energy of the columns.

6.3.3 Influence of the dopant

Small electron acceptors can interact with mesogenic electron donor and stabilize the stacking of discotic columns^[99]. 2,4,7-trinitro-9-fluorenone (TNF) is such an acceptor, the molecular structure of which is shown in Fig.6.19a. Kruglova and coworkers^[100] have studied the liquid crystalline structure of **D1**/2,4,7-trinitro-9-fluorenone (TNF) complex. They suggested that the TNF molecules are located between the columns within the tails of the discotic molecules (Fig.6.19b), which increases the rigidity of the columns and enhance the interaction between columns. Indeed they observed a decrease of the intercolumnar distance and an increased stability range of the columnar phase. Here we studied the orientation of the Col_h phase of **D1**/TNF (1:1) complex in cylinders. By comparing the result with that of the pure **D1**, we hope to verify the effect of the elastic properties of the discotic columns on their configuration in cylindrical confinement.

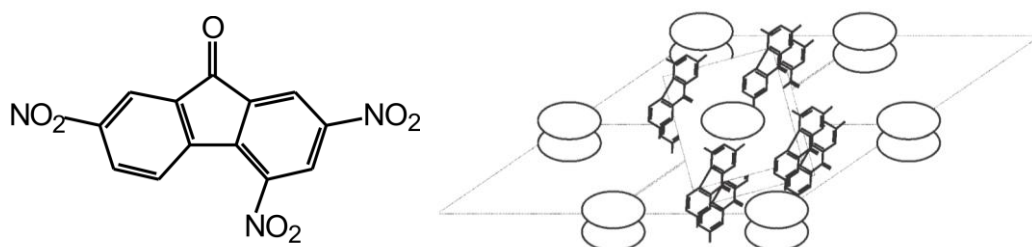


Figure 6.19. a) Structural formulas of 2,4,7-trinitro-9-fluorenone (TNF); b) Schematic representation of a possible **D1**-TNF arrangement (from ref [100]). Discs represent triphenylene cores. TNF lies between columns and forms columns itself.

Adding TNF extends the Col_{hex} phase temperature range from below R.T to 273 °C. The anchoring condition of the Col_{hex} phase of the complex on flat surface was first examined by POM. The thin film of **D1**/TNF sandwiched between two glass slides was slowly cooled from iso to R.T at 0.5 °C /min. When observed without analyzer it shows a dendritic texture (Fig.6.20), while with the analyzer in position, it turns totally black. This indicates the anchoring manner of the complex is also homeotropic on the glass surface as that of the pure **D1**.

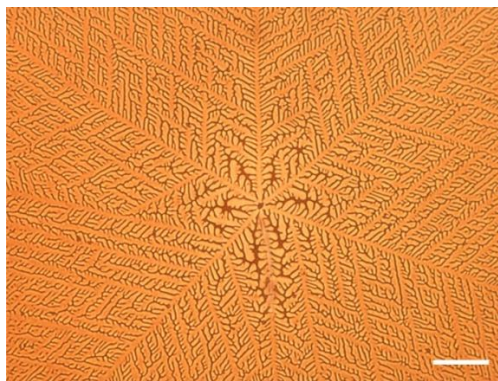


Figure 6.20. Optical microscope images of **D1/TNF** sandwiched between two glass slides observed without analyzer. The bar represents 50 micron.

AAO templates

The orientations of the Col_{hex} phase of **D1/TNF** in 20, 60, 200 and 400 nm AAO nanopores were first studied by SAXS. All samples were slowly cooled from iso temperature to R.T at a rate of $0.5^\circ\text{C}/\text{min}$. For the 20 nm template, at $\alpha=80^\circ$ the (100) spots on the equator and the (001) reflections on the meridian (Fig.6.21a) reveal that the columns are axially oriented. This can be explained by the fact that the TNF stiffens the columns and increases the bend modulus above the deformation modulus of the 2-d lattice. Thus the 20 nm modified AAO template can provide effective guidance for the columns of HAT6/TNF to orient parallel to the channel axis. Considering the large temperature range of the Col_{hex} phase of HAT6/TNF and its increased charge carrier mobility, it could be used to develop a way of fabricating organic nanowires with high conductivity. However, in a 60 nm template, the columns of **D1/TNF** are already perpendicular to the channel axis, as revealed by the hexagonal diffraction pattern at $\alpha=80^\circ$ (Fig.6.21b). The intercolumnar distance is calculated as 15.53\AA . Compared with the diffraction pattern of pure **D1** in 60 nm template (Fig.6.3), the intensity maxima are much sharper, indicating that the orientation of the 2-d lattice is much more ordered with the (100) plane parallel to the channel axis. This improved orientation is quite similar to that observed for sample **D2** and can be explained by the similar fact that the interaction between columns was increased by the dopant, which made the orientation of the hexagonal lattice more sensitive to the curvature.

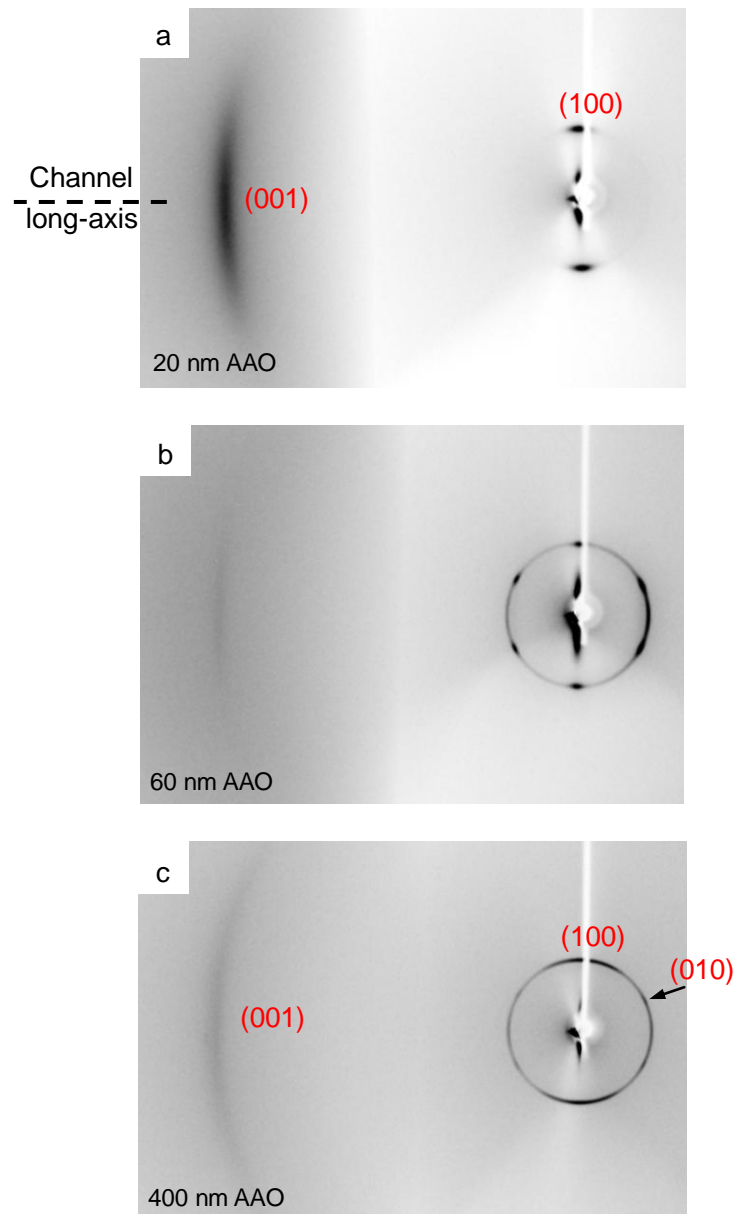


Figure 6.21. SAXS images of **D1/TNF** in (a) 20 nm, (b) 60 nm, (c) 400 nm AAO templates recorded at $\alpha=80^\circ$.

A similar SAXS pattern to that of the 60 nm sample was obtained for the 200 nm template. Surprisingly, for the 400 nm sample, the two $\{100\}$ intensities on the equator are strong while other four are barely visible (Fig.6.21c). Meanwhile the (001) intensities corresponding to an intra-columnar disc-disc distance of 3.15 \AA show up on the meridian. These reveal that the columns are mainly grown along the channel. Also the arch-shaped (100) intensities on the equator indicate that the columns are not perfectly parallel to the channel but have distribution angle with the channel axis. Besides, there coexist four weak

off-equator (10) reflections, which indicate a small portion of the columns is still perpendicular to the channel axis. Under homeotropic anchoring condition, we suspect that the columns are in escaped radial configuration in which the columns are perpendicular to the LC/solid interface close to the pore wall but bend to the axial direction close to the center of the cylinder. This is probably due to the large splay deformation energy in the center of the cylinder as a result of the increased inter-columnar interaction, which could be relieved by introducing certain amount of bend deformation^[101,102]

50 micron ID Glass capillary

When the **D1**/TNF complex is filled in a 50 micron ID capillary, the (100) SAXS intensity maxima always condense on the equator (Fig.6.22) and do not change as the capillary tube is rotated or moved along the long-axis. This is indicative of axial orientation of the hexagonal columns.

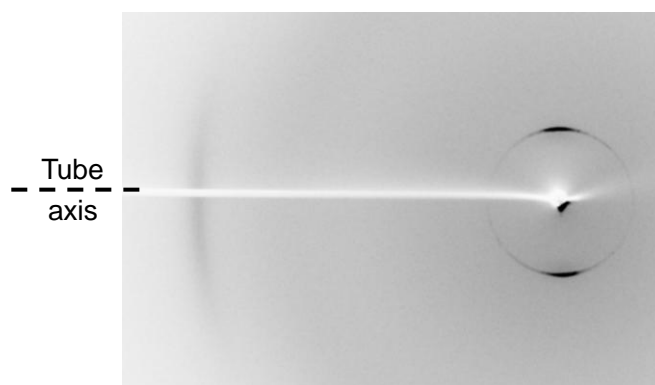


Figure 6.22. SAXS pattern of **D1**/TNF complex filled in a 50 micron ID capillary.

Silane-modified AAO templates

POM observation showed that, like in pure **D1**, the columns of **D1**/TNF complex also take planar alignment on the HTS modified surface (Fig.6.23). Here we filled the complex in the HTS treated AAO templates since it would be interesting to see the configuration of the rigid columns in the cylindrical confinement where planar anchoring on the curved surface is favored. For pure **D1**, we found that the columns prefer to bend following the curved

wall even in 20 nm pores. For the doped columns, on the other hand, the increased rigidity may shift the balance between the bend energy of the columns and the distortion energy of the hexagonal lattice and thus lead to a changed configuration.

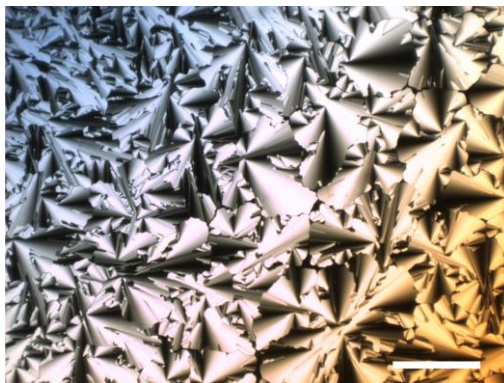


Figure 6.23. POM image of **D1/TNF** sandwiched between surface modified glass slides. The film was cooled from iso to R.T at 0.5 °C/min. The bar represents 200 micron.

The SAXS pattern of HAT6/TNF filled in a silane-modified 20 nm template recorded at $\alpha=75^\circ$ is shown in Fig.6.24a. The (100) spots on the equator and the (001) reflections on the meridian are characteristic of an axial orientation of the columnar phase. This again proves our suggestion that under planar anchoring condition, the orientation of the columns is determined by the competition of the bend deformation energy of the columns in concentric circular configuration and the distortion energy of the 2-d lattice in axial configuration. For the modified 60 nm template sample, similar diffraction pattern was obtained (Fig.6.24b) except that four weak off-equator (010) peaks can be seen.

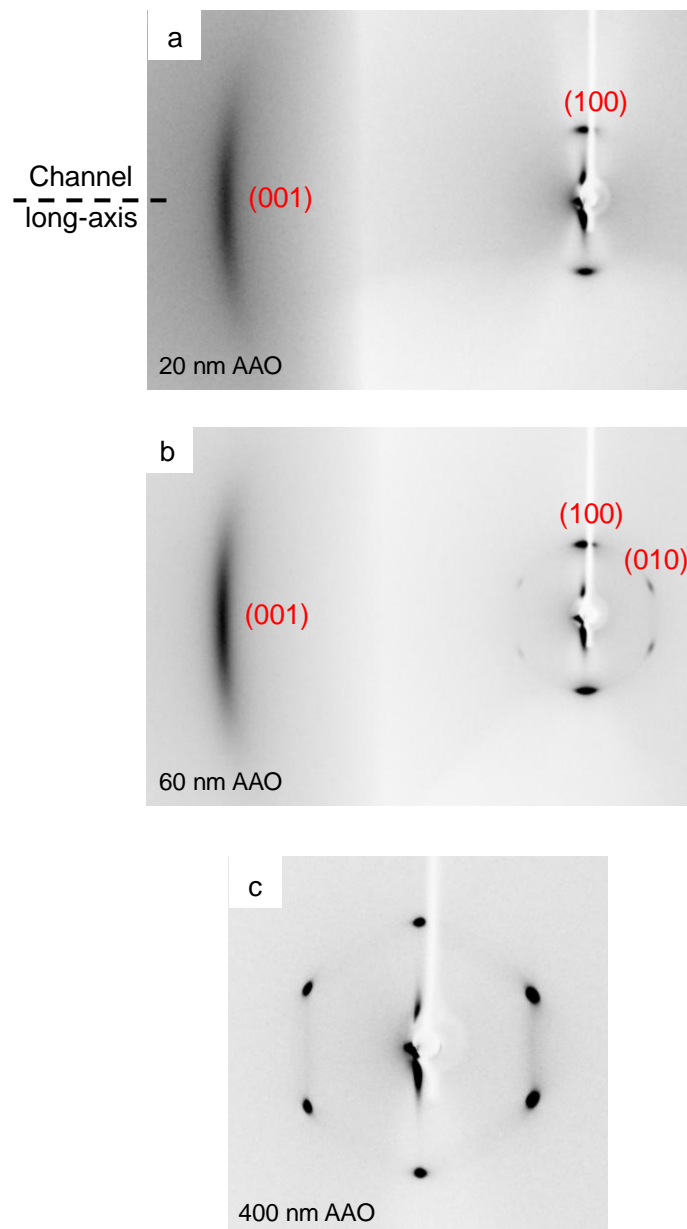


Figure 6.24. SAXS patterns of HAT6/TNF in silane-modified AAO templates: a) 20 nm at $\alpha=75^\circ$; b) 60 nm at $\alpha=80^\circ$. Note the asymmetry of the (001) reflection is due to the curvature of the Ewald sphere.

Interestingly, the diffraction pattern of the doped columns in the modified 400 nm template turns out to be hexagon at $\alpha=75^\circ$ with the (10) plane parallel to the channel axis (Fig.6.24c), which is similar to the diffraction pattern of pure **D1** in modified 400 nm template. It indicates that the orientation of the columns has inverted to circular concentric. It implies that at this pore size, the distortion energy of the hexagonal lattice again overcomes the bend energy of the columns, although they both decrease as the pore diameter increases.

Summary

Compounds	D1				D1/TNF			
	Untreated		HTS treated		Untreated		HTS treated	
Confinement	Config	(100) _{pl} / Cyl _{ax}	Config	(100) _{pl} / Cyl _{ax}	Config	(100) _{pl} / Cyl _{ax}	Config	(100) _{pl} / Cyl _{ax}
20 nm AAO	P	random	CC?		Axial		Axial	
60 nm AAO	P		CC?		P?		Axial	
200 nm AAO	P	⊥						
400 nm AAO	P	⊥	⊥		ER/ mixed domain		CC	
3.4 μ cap	P	⊥						
50 μ cap	P	tilted	tilted		Axial			
100 μ cap	ER							

Table 6.2 Summary of the configuration and the hexagonal lattice orientation of **D1** and **D1/TNF** complex in untreated / HTS treated cylindrical cavities. Abbreviations: (100)_{pl}=(100) plane; Cyl_{ax}=cylinder axis; Cap=capillary; Config=configuration; P=polar; CC=concentric circular; ER=escaped radial.

6.4 Helicene

Helicene is the prototypical helical compound with highly conjugated aromatic structure that possess a twist due to the physical overlap of the benzene rings. Our group has studied the supermolecular structure of a helicene (**D3**) in its columnar liquid crystalline phase by means of X-ray diffraction^[103]. It was found that this compound forms hexagonal columnar phase in which the internal structure of the columns are 13_2 hollow helices comprised of six-molecule repeat units, as shown in Fig.6.25(a-c). Fig.6.25(d-e) show the stacking of the racemate helical columns.

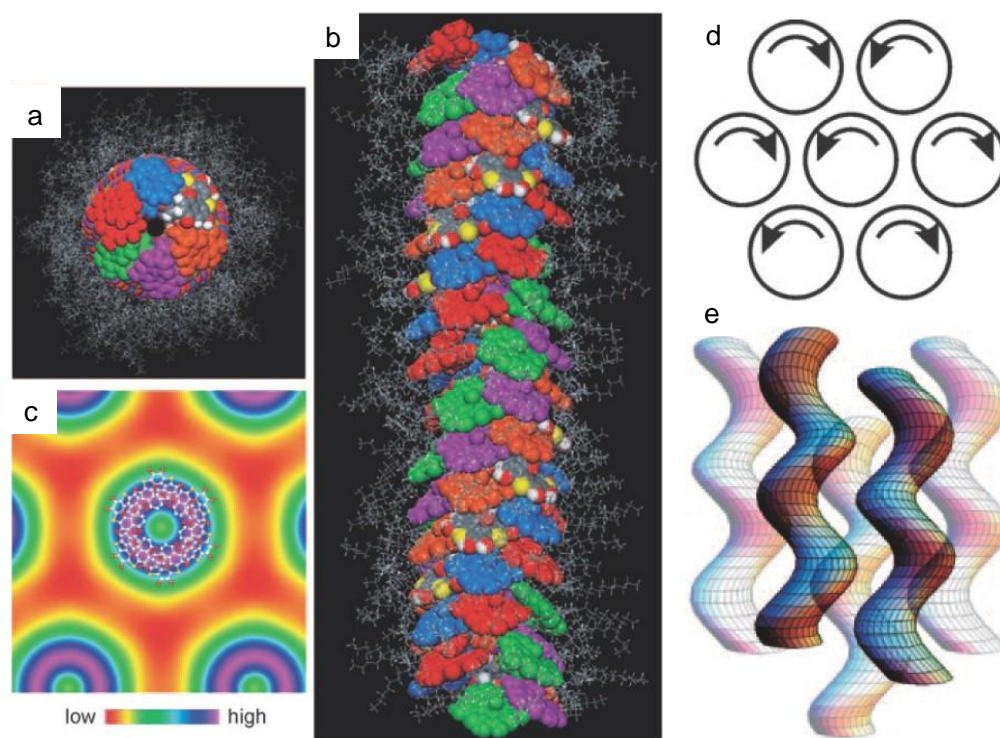


Figure 6.25. Molecular organization in the 13_2 helical column of **D3**. a) Views along column axis, b) side view. The aromatic cores and the alkyl tails are shown with space-filling and stick models, respectively. c) An asymmetric unit, without hydrogen atoms, is superimposed on the electron density map, illustrating the origin of the high-electron-density ring (purple). d, e) Stacking of racemate helical columns, with enantiomers segregated in separate right and left helical columns. In the top view d) arrows show the sense of the helix. In e) the darker helices are in the front row, the pale helices are behind.

Due to this helical structure, large rigidity of the columns could be expected. The orientation of the Col_{hex} phase of a racemic helicene **D3** in the 60 nm template was investigated by SAXS. As shown in Fig.6.26, intensity maxima appear only on the equator even at large α angle, which indicates that the columns are axially oriented in the nanochannel.

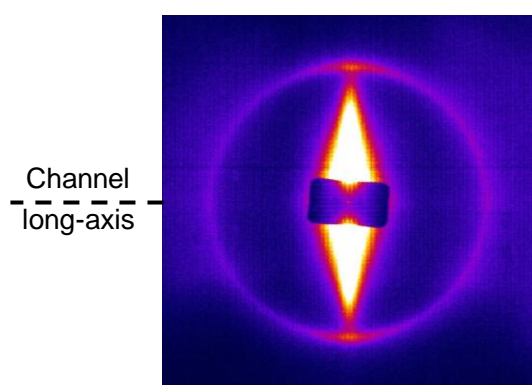


Figure 6.26 SAXS pattern of **D3** in the 60 nm AAO template. $\alpha=65^\circ$.

6.5 Conclusions

In this chapter we studied the configuration of several CDLCs in cylindrical cavities by X-ray diffraction. On the polar surface, the anchoring manner of all the discotic compounds studied was found to be homeotropic. The influence of three factors on the configuration of the discotic columns was investigated: the size of the cylinder, the polarity of the wall surface and the rigidity of the columns.

To evaluate the effect of pore size, we infiltrated CDLCs in AAO templates with nanometer, and glass capillaries with micrometer pore diameter. The configuration of a triphenylene derivative **D1** was determined to be mainly polar in cavities with diameters from 20 nm to 50 microns. In addition, it was found that in 60 nm diameter pores the hexagonal lattice is oriented with its (100) plane parallel to the channel axis, while in 200 and 400 nm diameter pores and above, the (100) plane becomes perpendicular to the channel axis. When the diameter increased to 100 micron, an escaped radial configuration was observed which has never been reported for the columnar discotic LCs.

By coating the solid substrate with HTS monolayer, we successfully switched the anchoring mode of the triphenylene derivative from homeotropic to planar. In silane-modified AAO templates, the columns of **D1** are oriented perpendicular to the channel, with the (10) plane of the hexagonal lattice parallel to the channel axis. In the 50 micron ID round capillary we observed a tilted orientation of the discotic columns with respect to the axis of the cylinder.

To investigate the effect of the rigidity of the discotic columns on their orientation inside the cylinder, we mixed **D1** with TNF, a dopant that was suggested to increase the rigidity of the columns. Under homeotropic anchoring condition, similar orientation of the columns was observed as that of the pure compound when the complex was filled in the 60 and 200

nm AAO templates, respectively. However, in 20 and 400 nm pores most of the columns are axially oriented. We suspect that in the 400 nm pores the columns of the complex form an escaped radial configuration. A plausible reason is that the dopant increased the interaction between columns and thus increased the splay deformation energy, which forced the columns to escape to the third dimension close the center of the cylinder. Under planar-anchoring condition, as achieved by modifying the cavity wall with silane, the orientation of the discotic columns “inverted” with respect to the homeotropic anchoring condition. That is, in the 20 and 60 nm AAO templates the columns are parallel to the channel axes, while in the 400 nm template the configuration is circular concentric. It indicates that in the small cavities the bend deformation energy exceeds the distortion energy of the hexagonal network. Axial orientation was also observed for a helical discotic columnar phase which has rigid columns.

CHAPTER 7 Mesoporous Nanofibers from Dual Structure-Directing Agents in AAO Template

7.1 Introduction

Mesoporous silica nanofibers (MSNF) are important mesostructured materials and have been widely investigated due to their potential applications. The synthesis of MSNF within the regular, larger channels of anodic aluminum oxide (AAO) templates provides a dual templating approach that opens a gateway to diverse mesoporous structures: if the MSNFs remain within the AAO membrane and the nanopores are aligned along the nanochannels of the membrane, inorganic membranes with pore diameters in the region between 3 and 10 nm are produced; if the alumina membrane material is dissolved, mesoporous silica nanofibers with diameters similar to that of the nanochannels of the alumina membranes can be obtained. Generally, MSNFs in AAO have been synthesized by sol-gel method. Lee and coauthors^[104] reported a novel method developed to fabricate MSNF in AAO templates using vapor phase synthesis (VPS). Several cationic surfactants were used as structure-directing agents. By TEM observation, they found that the alignment of the mesostructure changes from parallel-axial to helical when the length of the alkyl chain in the surfactant is decreased. Later they used dual structure-directing agents to produce the MSNF in the pores of AAO^[105]. In this chapter we present a combined SAXS and transmission electron microscope (TEM) study on the morphology of MSNFs produced with dual structure-directing agents using the VPS method in the pores of AAO membranes.

7.2 MSNF samples

Mesoporous silica nanofibers fabricated by using the VPS method via dual structure-directing agents in the channels of 200 nm AAO (purchased from Whatman) were kindly provided by the group of Prof. J. Jang of Seoul National University. Two surfactants used as structure-directing agents were: pluronic F127 (PEO₁₀₀PPO₆₅PEO₁₀₀) as the nonionic surfactant and different n-alkyltrimethylammonium bromides were used as cationic co-surfactants (Fig.7.1). The molar ratio between F127 and the cationic co-surfactant is 1:24. Samples prepared by different surfactant combinations are summarized in Tab.7.1.

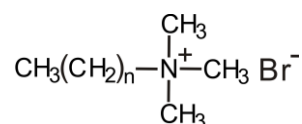


Figure 7.1 General molecular formula of the cationic surfactants.

Samples	Cationic surfactants	n	H.T (°C)
E1	DecylTAB	9	70
E2	DTAB	11	70
E3	TTAB	13	70
E4	CTAB	15	50
E5	CTAB	15	100

Table 7.1 Cosurfactants of compound **En**. H.T=hydrolyzation temperature. DecylTAB: decyltrimethyl-ammonium bromide; DTAB: dodecyltrimethyl-ammonium bromide; TTAB: tetradecyltrimethyl-ammonium bromide; CTAB: cetyltrimethylammonium bromide.

The synthetic procedure is depicted in Fig.7.2^[105]. The AAO membranes were first immersed in the surfactant solution which was composed of F127 (4 g), ethanol (2.3 g), hydrochloric acid (0.3 g), water (17.37 g) and 7.5×10^{-3} mol of cationic surfactant. Since the nanopores penetrate the membrane, the solution automatically infiltrates the membranes.

After the AAO membranes were removed from the surfactant solution they were placed in a closed vessel. 0.1g tetraethyl orthosiloxane was introduced into the vessel and vapor-phase hydrolysis was performed for 3h.

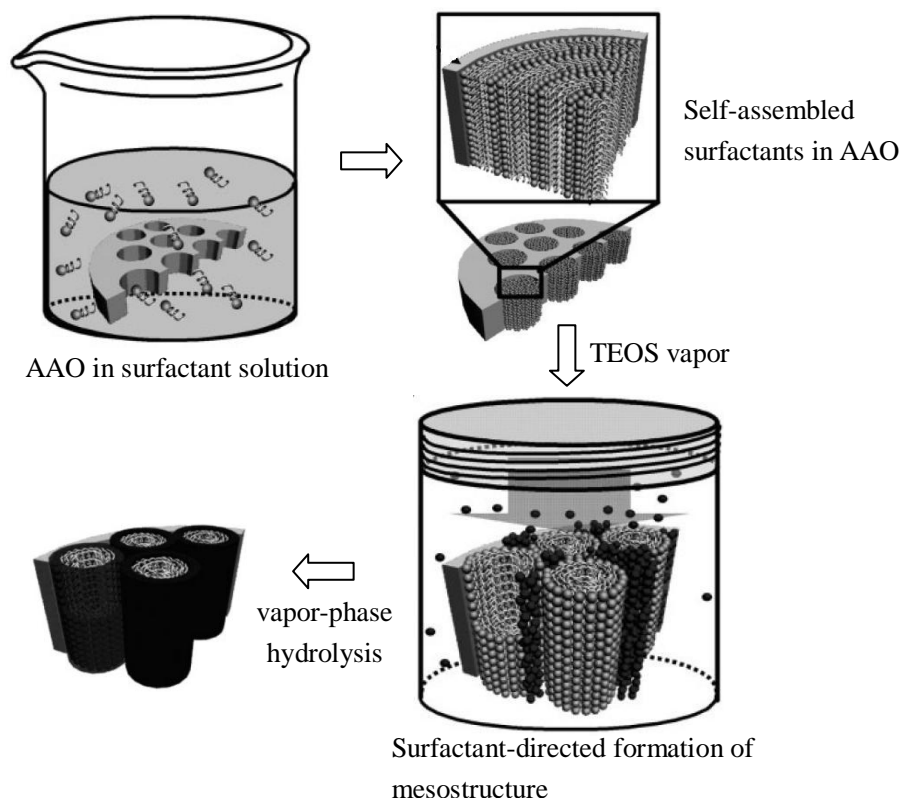


Figure 7.2 Schematic diagram of synthetic procedure for the preparation of mesoporous silica nanofiber using vapor-deposition hydrolysis. From ref [104].

7.3 Results and discussions

In this section the mesostructure of the silica nanofibers are investigated by SAXS and TEM. For SAXS experiments, the template membranes were examined as received with the MSNF inside the nanochannels. The same experiment layout was used as described in the previous chapters. For TEM observations, the AAO template was removed by dissolving in hydrochloric aqueous solution at 50 °C. An excess amount of distilled water was added for dilution. The MSNFs were precipitated and the upper solution was removed. This process was repeated to remove the AlCl_3 . The solution was then dried and MSNFs

were obtained as powder. Calcination was performed at 450 °C to remove any residual surfactant and any possible volatile compounds. The silica nanofibers were then floated in distilled water and transferred onto the copper grid.

E1

The MSNF of **E1** was fabricated using F127/ DecylTAB. The vapor-phase hydrolysis was performed at 70 °C for 3 hours. The diffraction pattern of **E1** in the AAO membrane recorded at $\Phi = 85^\circ$ is shown in Fig.7.3. The hexagonal pattern indicates that the silica nanopores are hexagonally ordered, with the (10) plane parallel to the inner wall surface and the nanopores are perpendicular to the long-axis of the AAO channels. The lattice parameter was calculated as $a_{\text{hex}}=3.64\text{nm}$.

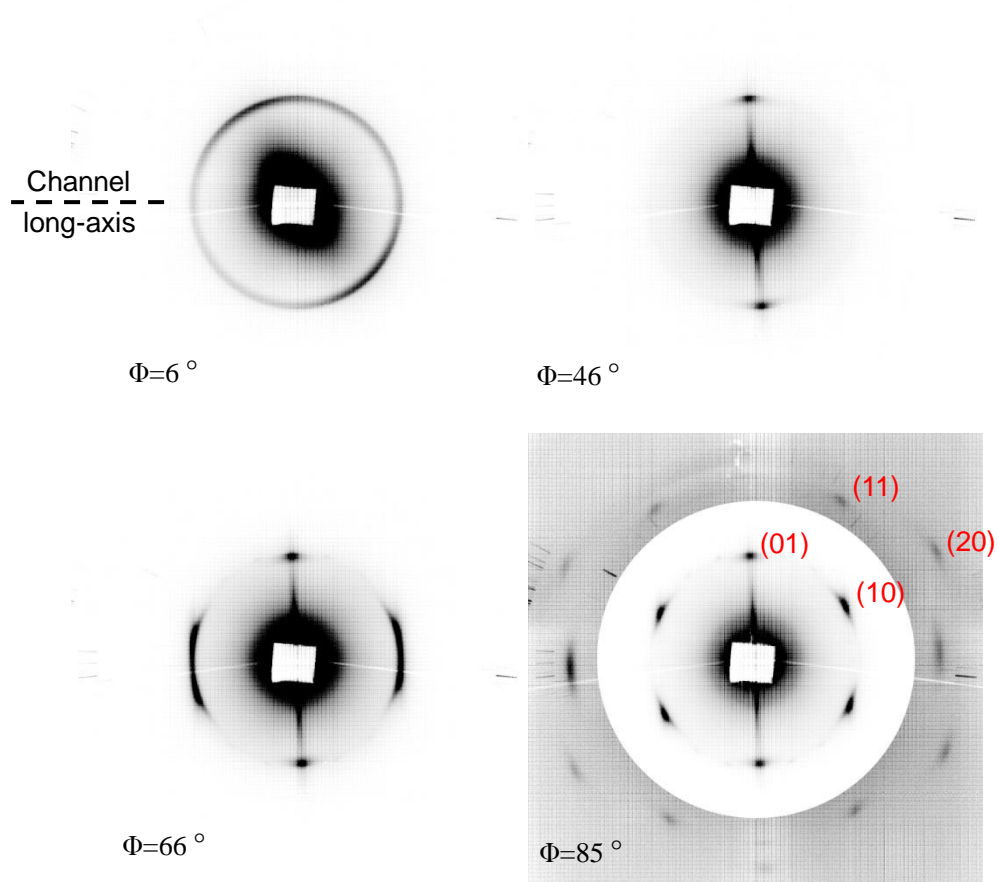


Figure 7.3. SAXS of **E1** recorded at different Φ angles.

E2

The second mesostructure studied was formed by using F127/ DTAB, with the alkyl chain of the cationic surfactant increased from decyl to dodecyl. Fig.7.4 shows the combined diffraction pattern of **E2** recorded at $\Phi=80^\circ$. This image is created by overlapping three images with different levels together in order to show the high order weak reflections. The reflections in the centre can be determined to be p6mm on the basis of the hexagonal symmetry and the 1: $\sqrt{3}$: 2...etc ratio of reciprocal spacings. The parameter of the hexagonal lattice was calculated as $a_{\text{hex}}=14.7\text{nm}$. Thus the increase of the length of the alkyl chain in the cationic surfactant significantly changed the size of the mesoporous structure.

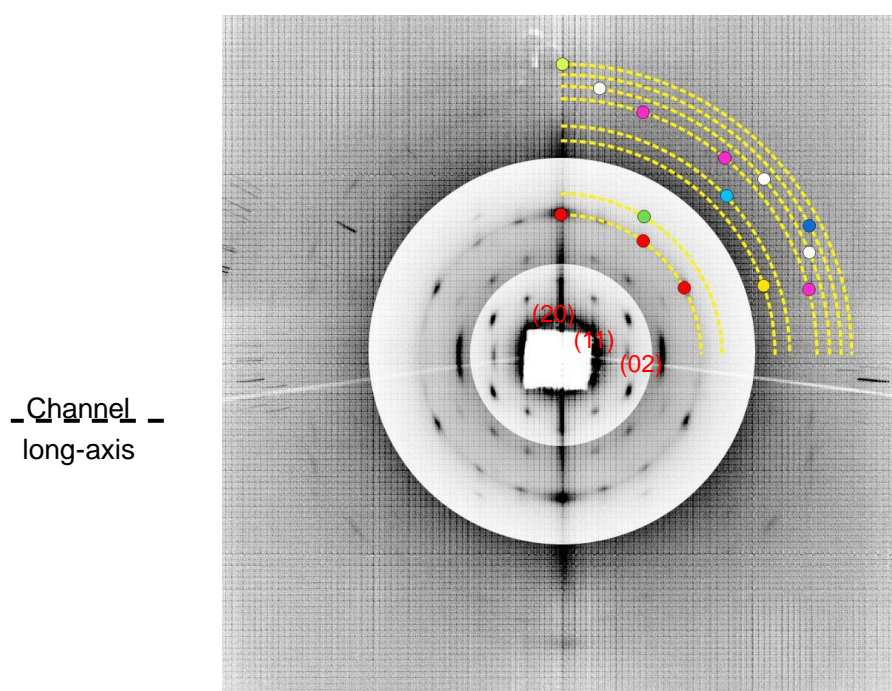


Figure 7.4 SAXS patterns of **E2** recorded at $\Phi=80^\circ$. The centre part belongs to a hexagonal lattice, while the reflections indicated by the colored spots belong to the Cub/Ia3d phase.

A close look at Fig.7.4 reveals that the reflections on the outer circles, as indicated by the yellow dashed lines, belong to another phase. The relative spacing of these reflections are measured as $\sqrt{6}$, $\sqrt{8}$, $\sqrt{14}$, $\sqrt{16}$, $\sqrt{20}$, $\sqrt{22}$, $\sqrt{24}$ and $\sqrt{26}$. Thus they can be assigned

as the {211}, {220}, {321}, {400}, {420}, {332}, {422}, {431} reflection groups of a Ia3d cubic phase. $d_{(211)}$ is calculated as 3.4nm and $a=8.4\text{nm}$.

(hkl)	d_{obs} -spacing (nm)	d_{cal} -spacing (nm)
(211)	3.41	3.41
(220)	2.97	2.95
(321)	2.24	2.23
(400)	2.10	2.09
(420)	1.87	1.87
(332)	1.78	1.78
(422)	1.70	1.71
(431)	1.66	1.64

Table 7.2 Experimental and calculated d-spacings of the color-marked reflections in Fig.7.4.

Based on the central part of the SAXS patterns recorded every one degree of Φ from 0° to 90° , the 3-d diffraction pattern of the Col_{hex} phase was constructed, as shown in Fig.7.3. This map is consistent with the hexagonal 2-d reciprocal net being rotationally averaged around the axis of the nanochannel. It indicates that the hexagonally arranged silica columns are perpendicular to the long axis of the AAO channels.

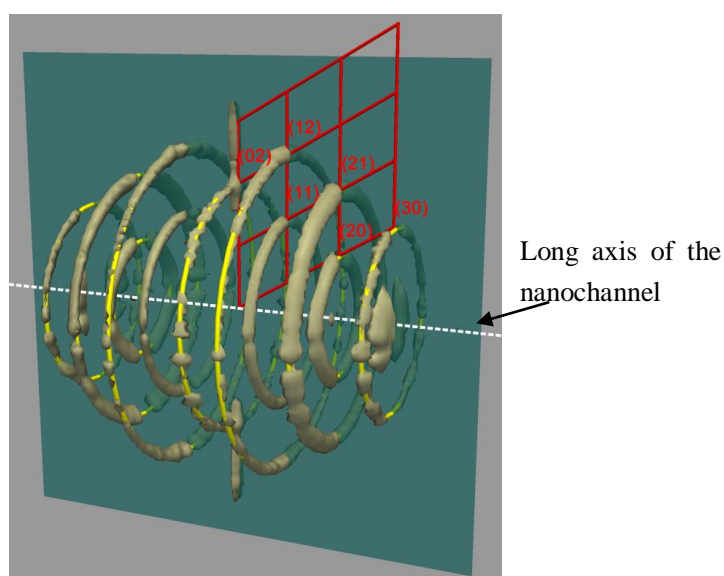


Figure 7.5 Reconstructed reciprocal space of **E2**. The dashed white line indicates the orientation of the nanopores in the AAO. The yellow lines are guides to the eyes.

Fig.7.6 shows the side view of single silica nanofiber, in which highly ordered hexagonal porous structure can be seen. These pores can be clearly seen through in the body of the fiber, which indicates the silica pores go straight through the fiber in the direction perpendicular to the fiber axis. In this situation, because most of the pore entrances are on the wall of nanofiber, foreign material enters the mesopores readily. Therefore, this structure could provide several benefits in the field of catalysts and storage.

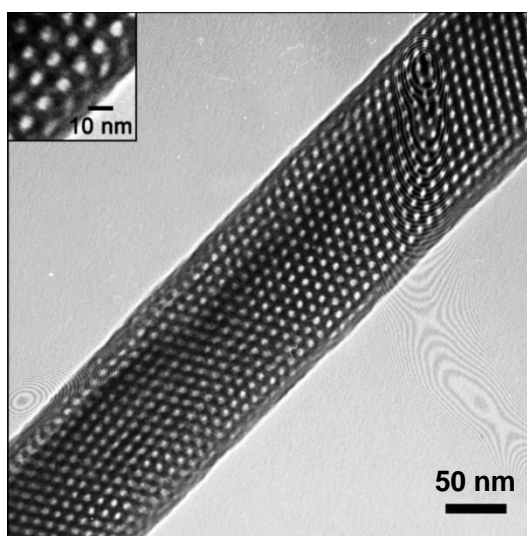


Figure 7.6 TEM image of **E2** showing the side view of one nanofiber obtained after removing the AAO membrane.

E3

When the ionic surfactant chain length is increased to tetradecyl by using TTAB, the mesophase obtained showed different orientation, as detected by SAXS. Fig.7.7a shows the diffraction pattern of sample **E3** recorded at $\Phi=70^\circ$. The ratio between the spacing of the first and second reflection peaks is $1:\sqrt{3}$, while the second and third reflections have a ratio of 1:2. We suspect it is a mixture of hexagonal and lamella phases. The parameters of the hexagonal and lamella structures were calculated as 7.3 and 3.5 nm from the diffraction pattern, respectively. It can be seen that the diffraction spots are concentrated on the equator, which indicates that the nanopores are oriented parallel to the channel axis. Fig.7.7b shows the TEM image of one extracted fiber, in which nanopores parallel to the

fiber can be seen. It further confirms the axial configuration of the nanopores. In this configuration, the filled AAO membrane may exhibit selective transport of molecules depending on their molecular size and thus has potential applications in molecular separation. However no lamella structure was observed during the TEM observation. Thus they were probably formed on the wall surface of the AAO membrane and were removed when the membrane was dissolved.

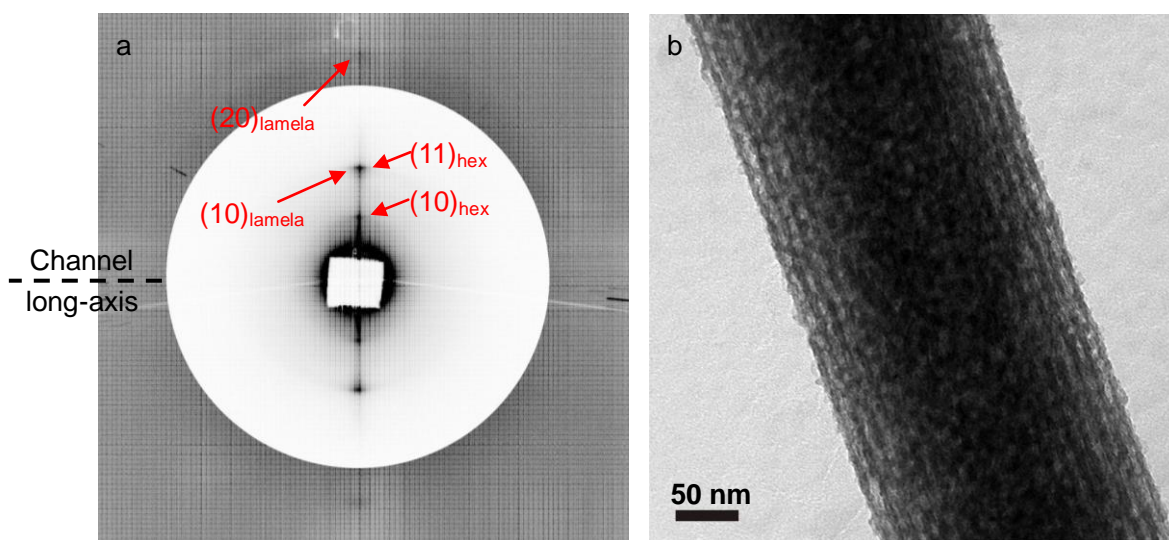


Figure 7.7 (a) SAXS pattern of **E3** in AAO recorded at $\Phi=70^\circ$; (b) TEM image of **E3** showing axially oriented silica nanopores.

E4

Fig.7.8a shows the diffraction pattern of sample **E4** fabricated using F127/CTAB surfactants in the AAO template, hydrolyzed at 50 °C. The hexagonal pattern reveals that the silica forms highly ordered hexagonal mesoporous structure, with the columns of the nanopores perpendicular to the channel axis and (10) plane parallel to the channel axis, as similar to that observed for **E2**. The parameter of the hexagonal lattice was calculated as 14.7 nm. Fig.7.8b shows the TEM image of the side view of one of the silica fiber, in which the hexagonally arranged pores can be seen through. Thus it can be concluded that the columns of the nanopores go straight through the fiber in the direction perpendicular to its long-axis.

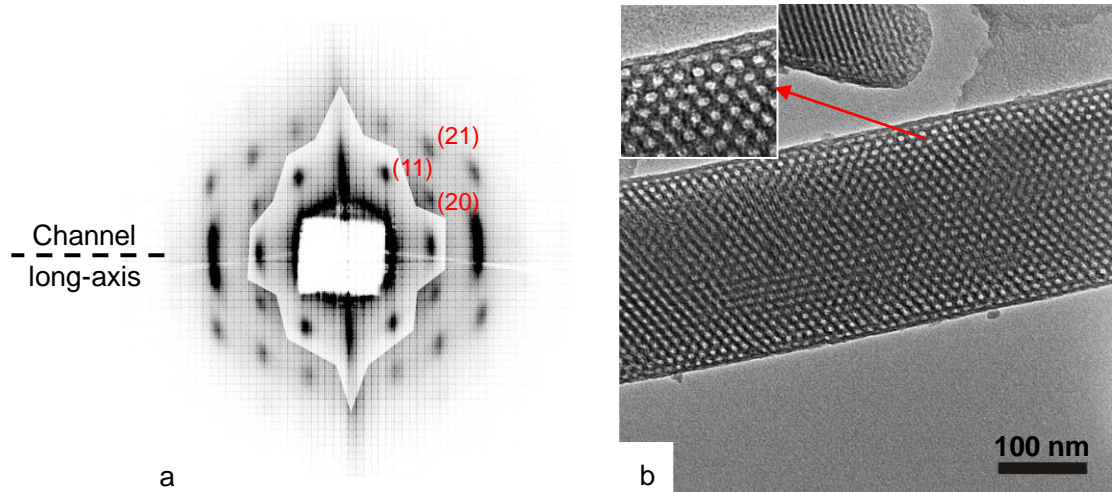


Figure 7.8 (a) SAXS pattern of **E4** in AAO recorded at $\Phi=85^\circ$; (b) TEM image showing one nano fiber of **E4**.

E5

Sample **E5** was also prepared using F127/CTAB surfactants, except that the hydrolysis was performed at 100 °C. With this sample, hexagonal diffraction pattern was obtained, as shown in Fig.7.9. The parameter of the hexagonal lattice was also calculated as 14.7 nm. However there are extra reflections on the equator, which can be indexed as (10) and (20) of a lamella phase. The distance between the layers was calculated as 3.5nm, which is the same as that obtained in sample **E3**. Thus it is possible that similar lamella structures were formed on the wall surface.

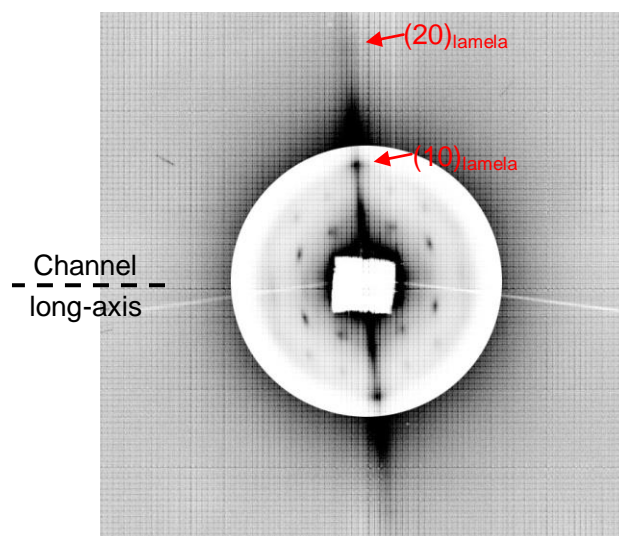


Figure 7.9. SAXS pattern of **E5** recorded at $\Phi=80^\circ$. The AAO membrane was slightly tilted away from the vertical direction during exposure.

7.4 Conclusion

In summary, the mesostructure of MSNFs template by dual surfactants in AAO membrane were characterized by SAXS and TEM observations. It was found that the introduction of cationic surfactant with different length of alkyl chains can affect both the size and configuration of the hexagonally ordered nanopores inside the MSNFs. With different cationic surfactant, the resulted nanopores can be controlled to be either perpendicular or parallel to the fiber axis. These structural features have potential applications in the field of catalysts, storage and molecular separation.

Summary

The initial goal of this research is to investigate the configuration of novel LC phases in cylindrical confinement. Those LC phases include the honeycomb phase and channeled-layer phase formed by polyphilic side-branched compounds (T-shaped molecules), as well as the columnar phase of discotic LCs. Due to the sensitivity to the electron-beam damage these materials cannot be characterized by traditional TEM. In this study we demonstrate a non-destructive method for resolving confined soft matters by combining X-ray scattering and AFM observation. In addition it was aimed to get insight into the mechanism that governs the configuration of the complex LC phases. This chapter will summarize the key findings and suggest perspectives for future work based on the results achieved.

Honeycomb phases

The configuration of honeycomb phases in cylindrical cavities was found to be strongly dependent on the anchoring manner. Thus the planarly and homeotropically anchored honeycomb phases were investigated separately in chapter 3 and 4.

The planar-anchored columns were determined to be concentric circular arranged, and two disclination lines close to the centre were directly observed by AFM for compound **A1** in 400 nm pores. The circular concentric configuration was found to be preserved in cavities up to 100 micron in diameter for compound **A3**. Surprisingly, no axial orientation has been observed for all the planar-anchored samples, which is suggested to be resulted from the high energy cost of the distortion of the 2-d lattice. Besides the 2-d lattice shows preferred orientations with respect to the wall surface in which the polygons are least deformed after being cut by the LC/solid interface.

For the homeotropic-anchored hexagonal honeycomb phase, bipolar configuration in which the columns grow straight cross the cylinders were determined in cavities up to 14 micron. While in 50 and 100 micron capillaries the columns were observed to be parallel to the cylinder and escaped radial configuration was suggested. Interestingly, the orientation

of the hexagonal lattice changes as the pore diameter is increased from 400 nm to 14 micron. It was suggested that in the small pores the orientation is determined by how the hexagonal lattice tile the curved surface, while in the large tube it is determined by the direction of the transverse edge dislocation line.

Channeled-layer hexagonal phases

For compound **C1** the 3d phase is suppressed in the 60 nm pores, instead the compound forms smectic phase. When the pore size was increased to 400 nm, it formed axially oriented ChL_{hex} phase. This is because in the ChL phase the aromatic cores are parallel to the columns and largely increase their rigidity; while the hexagonal lattice of the polar columns is flexible and the distortion energy is low compared with that of the honeycomb phase.

For compound **C2** the formation and configuration of the phases are temperature dependent. During slow cooling the compound mainly forms concentric circular conFigured smectic phase in the 400 nm pores. However the curvature can no longer support the circular concentric smectic phase when the cylinder increased to 2.5 micron due to the increased splay energy and instead axially oriented ChL_{hex} phase forms. While under fast cooling the ChL_{hex} phase orients with the columns perpendicular to channel axis both in the submicron and micrometer cylinders. It indicates that the concentric circular smectic phase is thermodynamically more stable but the growth of the ChL_{hex} phase is kinetically favored.

Columnar discotic liquid crystal phase

The configuration of the homeotropic-anchored discotic columns of a triphenylene derivative **D1** was determined to be mainly polar in cavities with diameters from 20 nm to 50 microns. When the diameter increased to 100 micron, an escaped radial configuration was observed. However no axial orientation was observed for pure **D1** under homeotropic anchoring condition, which conflicts the only published experimental work on confined discotics described in detail. Similar to sample **B1** in chapter 4, the orientation of the hexagonal lattice changes as the pore diameter is increased from 60 nm to 200 nm. The

same mechanism can be applied to explain this change. When doped with an electron acceptor, the columns become more rigid and axial orientation was observed in the 20 nm AAO template. For the doped sample, the escaped radial configuration was observed in the 400 nm pores.

Surface modification was performed to change the surface anchoring of the discotic columns from homeotropic into planar. Under this anchoring condition, the columns of pure **D1** are suggested to be circular concentric arranged, with the (10) plane of the hexagonal lattice parallel to the channel axis. Unlike the homeotropically anchored columns, this orientation of the hexagonal lattice didn't change as the pore diameter was increased from 60 nm to 400 nm. In the 50 micron round capillary a tilted orientation of the discotic columns with respect to the axis of the cylinder was observed.

For the doped system, on the other hand, the orientation of the discotic columns "inverted" with respect to the homeotropic anchoring condition. That is, in the 20 and 60 nm AAO templates the columns are parallel to the channel axes, while in the 400 nm template the configuration is circular concentric. It indicates that in the small cavities the bend deformation energy exceeds the distortion energy of the hexagonal network.

Axial orientation was also observed for a helical discotic columnar phase which has rigid columns.

Mesoporous Nanofibers fabricated via dual structure-directing agents in AAO templates

The mesostructure of MSNFs template by dual surfactants in AAO membrane were characterized by SAXS and TEM observations. It was found that the introduction of cationic surfactant with different length of alkyl chains can affect both the size and configuration of the hexagonally ordered nanopores inside the MSNFs. With different cationic surfactant, the resulted nanopores can be controlled to be either perpendicular or parallel to the fiber axis.

Future work

In this work we observed experimentally different arrangements of novel LC phases confined in cylindrical cavities. Those configurations of LC phases were discussed in terms of the surface anchoring condition, the size of the confined geometry, the deformation energy of the 2-d lattice and the rigidity of the columns.

However, there is still much experimental work needed in the future:

1. The morphologies of the LCs in pores smaller than 400 nm have not been observed directly. This is due to the roughness of the AAO membrane that hinders high resolution AFM imaging. Future work would involve the use of torsional mode AFM and sharp probes.
2. Although we successfully observed the disclination defect in the centre of the circular concentric configured LC columns, we have not yet observed the transverse edge dislocation that was suggested in the polar configuration.
3. It would be interesting to study the hexagonal honeycomb phase confined in cylinders with triangular or hexagonal shaped cross-section, or the square honeycomb phase in square shaped cylinders. In these cases the distortion of the 2-d lattice in the axial orientation could be minimized and thus the columns could be expected to align parallel to the channel.
4. For the capillary sample, there is a big gap between the confinement size between several micron tubes on the one hand and 100 micron tubes on the other. Capillaries with intermediate diameters need to be fabricated. Micro-beam X-ray diffraction could be a better technique for studying the capillary samples.

In addition, more quantitative calculation of the energy of different configurations could be interesting from the basic scientific point of view. Computer simulation and finite element analysis could be developed and used to predict the configuration of those complex LC phases in confined geometry.

From the point of view of applications, the axially oriented discotic columns doped with electron acceptor could be extracted and used as 1-d organic nano conductor. Also with the discotics in this configuration, the filled AAO membrane could be used to fabricate organic photovoltaic devices.

Further, the idea of confinement could be inverted. That is, instead of confining the organic compounds in inorganic materials, these LC phases could be used to confine the inorganic nano materials such as metal nanoparticles and carbon nano tubes. The defects in nematic and smectic LCs have already been successfully used to fabricate confined nanowires and photonic crystals of nanoparticles. Considering our samples, for example, the gold nanoparticles might be introduced within the central defect lines of the honeycomb columns in circular concentric configuration. For the homeotropically anchored honeycomb columns mixed with carbon nano-tubes, if well-dispersed, the carbon nano-tubes may find their way to align parallel to the LC columns in order to avoid breaking the 2-d lattice and thus achieve homeotropic orientation on a flat surface.

References

- [1]. G. Crawford, S. Zumer (Editors), *Liquid Crystals in Complex Geometries*, Taylor and Francis, London, **1996**.
- [2]. J. W. Doane, A. Golemme, J. L. West, *MOL CRYST LIQ CRYST.*, **1988**, 165, 511.
- [3]. S.Chandraskhar, *Liquid Crystals Second edition*, Cambridge University press, UK, **1992**.
- [4].G. Friedel, Ann, *Physique.*, **1922**, 18, 273.
- [5]. S. Chandrasekhar, B.K. Sasashiva, A. K. Suresh, *Pramana.*, **1977**, 9, 471.
- [6]. R.J. Bushby, O. R. Lozman, *Current Opinion in Colloid & Interface Science.*, **2002**, 7, 343.
- [7]. N.Boden, R. C. Borner, R. J. Bushby, et al., *Liquid Crystals*, **2006**, 33, 1443.
- [8]. F. Wurthner, *Chemical Communications*, **2004**, 14, 1564.
- [9].P. Weber, D. Guillon, A. Skoulios, *Liquid Crystals*, **1991**, 9, 369.
- [10]. P. Herwig, C. W. Kayser, K. Mullen, et al., *Advanced Materials*, **1996**, 8, 510.
- [11]. J. Barbera, O. A. Rakitin, M. B. Ros, T. Torroba, *Angew. Chem., Int. Ed.* **1998**, 37, 296.
- [12]. D. Caprion, L. Bellier-Castella, J. P. Ryckaert, *Phys. Rev. E: Stat., Nonlinear, Soft Matter Phys.*, **2003**, 67, 041703/1.
- [13]. N. Zharnikova, N. Usol'tseva, E. Kudrik, M. Thelakkat, *J. Mater. Chem.*, **2009**, 19, 316.
- [14]. C.Tschierske, *J. Mater. Chem.*, **1998**, 8, 1485.
- [15]. S. Kumar, *Liq. Cryst.*, **2004**, 31, 1037.
- [16]. S. Kumar, *Chem. Soc. Rev.*, **2006**, 35, 83.
- [17]. O. V. Kruglova, *Discotic Liquid Crystals: From Dynamics to Conductivity*, IOS Press, Amsterdam, **2007**.
- [18]. D. Adam, P. Schuhmacher, J. Simmerer etc., *Nature.*, **1994**, 371, 141.
- [19]. A. M. van de Craats, J.M. Warman, et al., *Adv. Mater.*, **1999**, 11,1469.
- [20]. N. Boden, R. J. Bushby, J. Clements, *J. Phys. Chem*, **1993**, 98, 5920.
- [21]. N. Boden, R. J. Bushby, J. Clements, B. Movaghar, *Physical Review B*, **1995**, 52, 13274.
- [22]. R. Freudenmann, B. Behnisch and M. Hanack, *J. Mater.Chem.*, **2001**, 11, 1618.
- [23]. W. Pisula, A. Menon, M. Stepputat, I. Lieberwirth, A. Kolbe, A. Tracz, H. Siringhaus, T. Pakula and K. Mullen, *Adv. Mater.*, **2005**, 17, 684.

- [24]. L. Schmidt-Mende, A. Fechtenkötter, K. Müllen, E. Moons, R. H. Friend and J. D. MacKenzie, *Science.*, **2001**, 293, 1119.
- [25]. S. Sergeev, W. Pisula and Y. H. Geerts, *Chem. Soc. Rev.*, **2007**, 36, 1902.
- [26]. C. Tschierske, *J. Mater. Chem.*, **2001**, 11, 2647.
- [27]. M. Kolbel, T. Beyersdorff, X. H. Cheng, C. Tschierske, J. Kain and S. Diele, *J. AM. Chem. Soc.*, **2001**, 123, 6809.
- [28]. X. H. Cheng, M. Prehm, M. K. Das, J. Kain, U. Baumeister, S. Diele, D. Leine, A. Blume, C. Tschierske, *J. Am. Chem. Soc.*, **2003**, 125, 10977.
- [29]. F. Hildebrandt et al, *Advanced materials.*, **1997**, 9, 564.
- [30]. B. Chen, U Baumeister, G. Pelzl, M. K. Das, X. B. Zeng, G. Ungar, C. Tschierske, *J. Am. Chem. Soc.*, **2005**, 127, 16578.
- [31]. S. Singh, *Liquid Crystal: fundamentals*, World Scientific, Singapore, **2002**.
- [32]. Y. Bouligand, *J. de Physique.*, **1980**, 41, 1297.
- [33]. M. Kleman and P. Oswald, *J. de Physique.*, **1982**, 43, 655.
- [34]. F. C. Frank, *Disc. Faraday Soc.*, **1958**, 25, 19.
- [35]. O. Lehmann, *Flüssige Kristalle.*, **1904**.
- [36]. E. Dzyaloshinskii, *Sov. Phys.*, **1970**, 31, 773.
- [37]. P. E. Cladis and M. Kleman, *J. Phys. (Paris).*, **1972**, 33, 591.
- [38]. R.B. Meyer, *Philos. Mag.* **1973**, 27, 405.
- [39]. C. E. Williams, P. Pieranski, and P. E. Cladis, *Phys. Rev. Lett.*, **1972**, 29, 90.
- [40]. P. G. de Gennes, *The Physics of Liquid Crystals* (Clarendon, Oxford, 1974).
- [41]. D. W. Allender, G. P. Crawford, and J. W. Doane, *Phys. Rev. Lett.*, **1991**, 67, 1442.
- [42]. G. P. Crawford, D. W. Allender, and J. W. Doane, *Phys. Rev. A.*, **1991**, 44, 2570.
- [43]. G. P. Crawford, M. Vilfan, and J. W. Doane, *Phys. Rev. A.*, **1991**, 43, 835.
- [44]. G. P. Crawford, D. W. Allender, and J. W. Doane, *Phys. Rev. A.*, **1992**, 45, 8693.
- [45]. R. J. Ondris-Crawford, G. P. Crawford, S. Zumer, and J. W. Doane, *Phys. Rev Lett.*, **1993**, 70, 194.
- [46]. R. J. Ondris-Crawford, M. Ambrozic, J. W. Doane, S. Zumer, *Physical Review E.*, **1994**, 50, 4773.
- [47]. S. Kralj, S. Žumer, *Phys. Rev. E.*, **1996**, 54, 1610.

- [48]. G. P. Crawford, L. M. Steele, R. J. Ondris-Crawford, G. S. Iannacchione, C. J. Yeager, J. W. Doane, D. Finotello, *J. Chem. Phys.*, **1992**, 96, 7788.
- [49]. G. P. Crawford, R. Stannarius, J. W. Doane, *Phys. Rev. A.*, **1992**, 44, 2558; G. P. Crawford, R. J. Ondris-Crawford, J. W. Doane, S. Zumer, *Phys. Rev. E.*, **1996**, 53, 3647.
- [50]. T. Jin, B. Zalar, A. Lebar, M. Vilfan, S. Zumer, and D. Finotello, *Eur. Phys. J. E.*, **2005**, 16, 159.
- [51]. R. Hurt, G. Krammer, G. Crawford. etc., *Chem. Mater.*, **2002**, 14, 4558.
- [52]. M. Steinhart, S. Zimmermann, P. Goring. etc., *Nano Letters*, **2005**, 5, 429.
- [53]. C. Stillings, E. Martin, M. Steinhart. etc., *Mol. Cryst. Liq. Cryst.*, **2008**, 495, 285.
- [54]. C. Stillings, M. Steinhart, E. Martin, etc., *Eur. Phys. J.*, **2009**, E28., 305.
- [55]. D. Caprion, *Eur. Phys. J.*, **2009**, E28, 305.
- [56]. D. Routkevitch et al, *Phys. Chem.*, **1996** 100, 14037.
- [57]. R. J. Tonucci, B. L. Justus, A. J. Campillo, and C. E. Ford, *Science.*, **1992**, 258, 783.
- [58]. T. W. Whitney, et al, *Science.*, **1993**, 261, 1316.
- [59]. H. Masuda, K. J. Fukuda, *Science*, 1995, 268, 5216.
- [60]. J. P. O'Sullivan, G. C. Wood, *Proc. R. Soc. London, Ser. A.*, **1970**, 317, 511.
- [61]. V. P. Parkhutik, V. I. Shershulsky, *J. Phys. D: Appl. Phys.*, **1992**, 25, 1258.
- [62]. J. Siejka, C. Ortega, *J. Electrochem. Soc.*, **1977**, 124, 883.
- [63]. O. Jessensky, F. Muller, U. Gosele, *Appl. Phys. Lett.*, **1998**, 72, 1173.
- [64]. K. S. W. Sing, D. H. Everett, R. H. W. Haul, L. Moscou, R. A. Pierotti, J. Rouquerol, T. Siemieniowska, *Pure. Appl. Chem.*, **1985**, 57, 603.
- [65]. C. T. Kresge, M. E. Leonowicz, W. J. Roth, J. C. Vartuli, J. S. Beck, *Nature.*, **1992**, 359, 710.
- [66]. a) M. G. Kanatzidis, *Adv. Mater.*, **2007**, 19, 1165; b) J. Jang, J. Bae, *Chem. Commun.*, **2005**, 1200; c) E. Kockrick, P. Krawiec, W. Schnelle, D. Geiger, F. M. Schappacher, R. Pottgen, S. Kaskel, *Adv. Mater.*, **2007**, 19, 3021; d) C. Liang, Z. Li, S. Dai, *Angew. Chem.*, **2008**, 120, 3754; *Angew. Chem. Int. Ed.*, **2008**, 47, 3696; e) M. Vallet-Reg, F. Balas, D. Arcos, *Angew. Chem.*, **2007**, 119, 7692; *Angew. Chem. Int. Ed.*, **2007**, 46, 7548; *Angew. Chem.*, **2007**, 119, 7692.
- [67]. H. Yang, A. Kuperman, N. Coombs, S. Mamiche-Afara, G. A. Ozin, *Nature.*, **1996**, 379, 703.
- [68]. Z. Yang, Z. Niu, X. Cao, Z. Yang, Y. Lu, Z. Hu, *Angew. Chem. Int. Ed. Engl.*, **2003**, 42, 4201.
- [69]. A. Yamaguchi, F. Uejo, T. Yoda, T. Uchida, Y. Tanamura, T. Yamashita, N. Teramae, *Nat. Mater.*,

2004, 3, 337.

- [70]. Q. Lu, F. Gao, S. Kmarmeni, T. E. Mallouk, *J. Am. Chem. Soc.*, **2004**, 126, 8650.
- [71]. K. Maeda, K. Ichinose, T. Yamazaki, T. Suzuki, *Micropor Mesopor Mat.*, **2008**, 112, 603.
- [72]. Y. Wu, G. Cheng, K. Katsov, S. W. Sides, J. Wang, J. Tang, G. H. Fredrickson, M. Moskovits, G. D. Stucky, *Nature Mater.*, **2004**, 3, 816.
- [73]. D. Wang, R. Kou, Z. Yang, J. He, Z. Yang, Y. Lu, *Chem. Commun.*, **2005**, 166.
- [74]. B. Platschek, N. Petkov, T. Bein, *Angew. Chem. Int. Ed. Engl.*, **2006**, 45, 1134.
- [75]. H. Masuda, K. Yada, A. Osaka, *Jpn. J. Appl. Phys., Part 2*, **1998**, 37, L1340.
- [76]. H. Masuda, K. Fukuda, *Science*, **1995**, 268, 1446.
- [77]. O. Jessensky, F. Muller, U. Gosele, *Appl. Phys. Lett*, **1998**, 72, 1173.
- [78]. Y. M. Sun, M. Steinhart, etc., *Rapid Commun.* **2005**, 26, 369.
- [79]. D. K. Aswal, S. Lenfant, D. Guerin, J. V. Yakhmi, D. Vuillaume. *Anal Chim Acta.*, **2006**, 568, 84.
- [80]. C. Hammond, *The Basics of Crystallography and Diffraction, 3rd Edition*, Oxford University Press, UK, **2009**.
- [81]. T. A. Ezquerra, *Applications of Synchrotron Light to Scattering and Diffraction in Materials and life Sciences*, Springer, Berlin Heidelberg, **2009**.
- [82]. B. He, *Two-Dimensional X-ray Diffraction*, John Wiley&Sons, Inc, New Jersey, **2009**.
- [83]. U. Pietsch, V. Holy, T. Baumbach, *High-resolution X-ray Scattering from Thin Films to Lateral Nanostructures*, Springer, New York, **2004**.
- [84]. G. Ungar, F. Liu, X. B. Zeng, B. Glettner, M. Prehm, R. Kieffer, C. Tschierske, *J. Phys., Conf. Series.*, **2010**, 247, 012032.
- [85]. P. Eaton, P. West, *Atomic Force Microscopy*, Oxford University press, UK, **2010**.
- [86]. W. R. Bowen, N. Hilal, *Atomic Force Microscopy in Process Engineering*, Elsevier Ltd, UK, **2009**.
- [87]. B. Chen, X. B. Zeng, U. Baumeister, G. Ungar, C. Tschierske, *Science*, **2005**, 307, 96.
- [88]. Masuda, H.; Yada, K.; Osaka, A. *Jpn. J. Appl. Phys.* 1998, 37, L1340 – L1342.
- [89]. Choi, J.; Luo, Y.; Wehrspohn, R. B.; Hillebrand, R.; Schilling, J.; Gosele, U. *J. Appl. Phys.* 2003, 94, 4757 – 4762.
- [90]. C. Hammond, *The Basics of Crystallography and Diffraction*, Oxford University Press, uk, **2009**.
- [91]. W. Irvine, V. Vitelli, P. Chaikin, *Nature*, **2010**, 468, 947.
- [92]. B. Chen, X. B. Zeng etc., *Angew. Chem.*, **2004**, 43, 4621.

-
- [93]. K. Kawata, *Chem. Rec.*, **2002**, 2, 59.
- [94]. S.Chandrasekhar, G.S.Ranganath, *Rep. Prog. Phys.* **1990**, 53, 57.
- [95]. E. Fontes, P. A. Heiney, W. H. De Jeu, *Phys. Rev. Lett.*, **1988**, 61, 1202.
- [96]. Van der Craats, A. M. Warman, etc., *Adv. Mater.*, **1996**, 8, 823; Van der Craats, A. M. de Haas, etc., *Synth. Met.*, **1997**, 86, 2125.
- [97]. E. Grelet, H. Bock, *Europhys. Lett.*, **2006**, 73, 712.
- [98]. S. Sergeev, J. Levin, J. Y. Balandier, E. Pouzet, Y. H. Geerts, *Mendeleev Communications*, **2009**, 19, 185.
- [99]. K. Praefcke, J. D. Holbrey, *Journal of inclusion phenomena and molecular recognition in chemistry*, **1996**, 24, 19.
- [100]. O. Kruglova, E. Mendes, etc., *ChemPhysChem*, **2007**, 8, 1338.
- [101]. P. E. Cladis and M. Kleman, *J.Phys.(Paris)*., **1972**, 33, 591.
- [102]. R.B. Meyer, *Philos. Mag.* **1973**, 27, 405.
- [103]. M. A. Shcherbina, X. B. Zeng. etc., *Angewandte*, **2009**, 48, 7837.
- [104]. K. J. Lee, S. H. Min, J. Jang, *Small.*, **2008**, 4, 1945.
- [105]. K. J. Lee, S. H. Min, J. Jang, *Chem. Eur. J.*, **2009**, 15, 2491.

Appendix

A.1 Construction of the 3-d diffraction pattern

Each spot (x,z) on the diffraction image corresponds to a point (q_x, q_y, q_z) in the reciprocal space. If we take the x' and z' axes in the q -space to be parallel to the x and z axes of the diffraction image respectively and y' axis at the direction of the incident beam, it can be worked out that:

$$q_x' = \frac{2\pi x}{\lambda \sqrt{S_d^2 + x^2 + z^2}}$$

$$q_y' = \frac{2\pi}{\lambda} \left(\frac{S_d}{\sqrt{S_d^2 + x^2 + z^2}} - 1 \right)$$

$$q_z' = \frac{2\pi}{\lambda} \frac{z}{\sqrt{S_d^2 + x^2 + z^2}}$$

Here S_d is the sample to detector distance, and λ the x-ray wavelength. As the template is rotated by Φ , the axis of the reciprocal space is rotated by Φ as well. Here the x and z axes are parallel to the template, while the y axis is perpendicular to it, and we have:

$$q_x = q_x' \cos\Phi + q_y' \sin\Phi$$

$$q_y = q_y' \cos\Phi - q_x' \sin\Phi$$

$$q_z = q_z'$$

From the above equations each spot on the diffraction images can be mapped into the reciprocal space.

To construct the 3-d diffraction pattern, a cubic volume in the reciprocal space $(-Q < q_x, q_y, q_z < Q)$ is divided into typically $100 \times 100 \times 100$ boxes. For each sample, every point of all diffraction images is then mapped to one of these boxes, and an averaged intensity value is taken for all the points fall into each particular box. The 3-d diffraction pattern is then examined in ParaView (Copyright Kitware, Inc.) using iso-intensity surfaces.

A.2 Calculation of the correlation length

The correlation length L is calculated according to the Scherrer equation

$$L = \frac{K\lambda}{\beta \cos\theta}$$

where K is the Scherrer constant that depends on the shape of the crystalline, λ is the wavelength of the X-ray beam, β is the half width at half maximum (in the unit of angle), and θ is the Bragg angle of the peak. Here we use $K=1$.

$$L = \frac{2d \sin\theta}{\beta \cos\theta} = \frac{2\pi \sin\theta}{q\beta \cos\theta}$$

Where d is the d spacing of the lattice and q is the dimension of the reciprocal lattice director (q value). Under the experimental geometry of GISAXS, $\sin\theta=1$ and $\cos\theta=1$, thus the Scherrer equation can be changed to:

$$L = \frac{2\pi\theta}{q\beta} = \frac{2\pi}{\Delta q}$$

where Δq (\AA^{-1}) is the full width at the half height of the peaks fitted to a Gaussian profile by Peaksolve. In order to correct for instrumental broadening the profile of the primary synchrotron beam in the focal, i.e. detector plane was determined. We used two different standards with highly ordered structure, one crystalline (n-alkane $C_{40}H_{82}$, 99% pure, Sigma-Aldrich), and a liquid crystal amphiphile, ALSC-15, both having been slowly cooled from the melt and annealed. Both compounds gave a series of reflection orders, and the peak widths of these reflections were extrapolated to $q = 0$ to correct for the effect of lattice strain in the reference samples.

A.2.1 Determination of direct beam width

$C_{40}H_{82}$, orthorhombic phase:

First peak: $q = 0.119 \text{ \AA}^{-1}$ ($d_{(002)} = 52.8 \text{ \AA}$), $\Delta q_s = 0.004483 \text{ \AA}^{-1}$

Second peak: $q = 0.238 \text{ \AA}^{-1}$ ($d_{(004)} = 26.4 \text{ \AA}$), $\Delta q_s = 0.005996 \text{ \AA}^{-1}$

Third peak: $q = 0.357 \text{ \AA}^{-1}$ ($d_{(006)} = 17.6 \text{ \AA}$), $\Delta q_s = 0.007632 \text{ \AA}^{-1}$

Extrapolation gives $\Delta q_s = 0.002888 \text{ \AA}^{-1}$ at $q = 0$.

ALSC-15, 170C, rectangular columnar $p2gg$ phase:

First peak: $q = 0.130 \text{ \AA}^{-1}$ ($d = 48.3 \text{ \AA}$), $\Delta q_s = 0.004937 \text{ \AA}^{-1}$

Second peak: $q = 0.178 \text{ \AA}^{-1}$ ($d = 35.3 \text{ \AA}$), $\Delta q_s = 0.005579 \text{ \AA}^{-1}$

Third peak: $q = 0.190 \text{ \AA}^{-1}$ ($d = 33.1 \text{ \AA}$), $\Delta q_s = 0.006227 \text{ \AA}^{-1}$

Forth peak: $q = 0.202 \text{ \AA}^{-1}$ ($d = 31.2 \text{ \AA}$), $\Delta q_s = 0.005882 \text{ \AA}^{-1}$

Fifth peak: $q = 0.210 \text{ \AA}^{-1}$ ($d = 30.0 \text{ \AA}$), $\Delta q_s = 0.005974 \text{ \AA}^{-1}$

Extrapolation gives $\Delta q_s = 0.003166 \text{ \AA}^{-1}$ at $q = 0$.

The average of the two extrapolated values above gives an estimation of the peak width of the direct beam Δq_s as 0.003 \AA^{-1} .

A.2.2 Determination of intrinsic line widths and coherence length

The instrumental peak width was subtracted from the Gaussian fitted to the experimental peak, taking advantage of the property that the sum of the widths of two Gaussian functions is equal to the width of their convolution. Thus the coherence length can be calculated as:

$$L = \frac{2\pi}{\Delta q - \Delta q_s}$$

For the 400 nm AAO sample filled with **B1**, the calculation was based on the diffraction pattern at $\Phi = 70^\circ$ (Fig.A.1a). (01) peak (equator): $q=0.19714 \text{ \AA}^{-1}$, $\Delta q=0.00741062 \text{ \AA}^{-1}$, $d_{(01)}=31.9 \text{ \AA}$; $L_{(01)}=1648 \text{ \AA}$; (10) peak: $\Delta q=0.00676992 \text{ \AA}^{-1}$, $L_{(10)}=3959 \text{ \AA}$

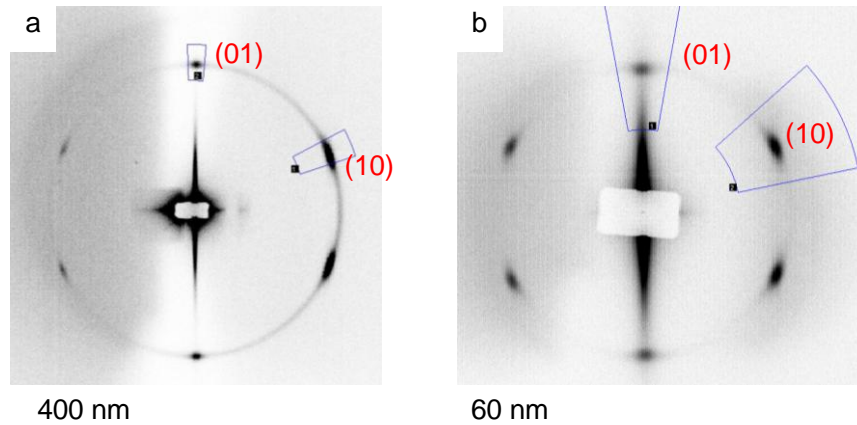


Figure A. 1. a) Scans on the SAXS pattern of 400 nm template filled with **B1** at $\Phi = 70^\circ$; b) scans for the 60 nm sample.

For the 60 nm AAO sample filled with **B1**, the scans were performed on the SAXS pattern at $\Phi = 81.5^\circ$ (Fig.A.1b). (01) peak: $q = 0.195 \text{ \AA}^{-1}$, $d_{(01)} = 32.2 \text{ \AA}$, $\Delta q = 0.018715 \text{ \AA}^{-1}$, $L_{(01)} = 393 \text{ \AA}$. (10) peak: $q = 0.201 \text{ \AA}^{-1}$, $d_{(10)} = 31.3 \text{ \AA}$, $\Delta q = 0.011009 \text{ \AA}^{-1}$, $L_{(10)} = 785 \text{ \AA}$.